MONITORING CELL INFILTRATION INTO THE MYOCARDIAL INFARCTION SITE USING MICROMETER-SIZED IRON OXIDE PARTICLES-ENHANCED MAGNETIC RESONANCE IMAGING

A Dissertation
Presented to
The Academic Faculty

By

Yidong Yang

In Partial Fulfillment
Of the Requirements for the Degree
Doctor of Philosophy in Medical Physics

Georgia Institute of Technology

August 2010

MONITORING CELL INFILTRATION INTO THE MYOCARDIAL INFARCTION SITE USING MICROMETER-SIZED IRON OXIDE PARTICLES-ENHANCED MAGNETIC RESONANCE IMAGING

Approved by:

Dr. Tom C.-C. Hu, Coadvisor
Department of Radiology
Medical College of Georgia

Dr. Sang Hyun Cho, Coadvisor
School of Mechanical Engineering
Georgia Institute of Technology

Dr. Chris C.-K. Wang
School of Mechanical Engineering
Georgia Institute of Technology

Dr. John N. Oshinski
Department of Biomedical Engineering
Georgia Institute of Technology

Dr. Nathan E. Yanasak
Department of Radiology
Medical College of Georgia

Dr. Autumn Schumacher
School of Nursing
Medical College of Georgia

Date Approved: June 21, 2010

ACKNOWLEDGEMENTS

I would like to express my deepest appreciation to my research advisor, Dr. Tom C.-C. Hu, for his supervision and guidance throughout my graduate study. He is not only a great advisor, but also a wonderful friend, who always provides me constructive advice about science and life. Without his guidance and persistent help, this dissertation would not have been possible.

I would like to record my gratitude to my coadvisor, Dr. Sang Hyun Cho and my committee members, Dr. Chris C.-K. Wang, Dr. John N. Oshinski, Dr. Nathan E.Yanasak and Dr. Autumn Schumacher, for serving on my PhD committee and for their valuable comments. They provided helpful suggestions and indispensable support for my career development.

I would like to thank my colleagues, Dr. Jimei Liu and Yuhui Yang. They contributed to this research with their hard work and excellent skills on mice surgery. I would also like to thank my classmate and colleague, Dr. Benjamin Waghorn. It is a pleasure to work with them in the Small Animal Imaging Lab at the Medical College of Georgia.

I acknowledge the International Society for Magnetic Resonance in Medicine (ISMRM) for permission to include Chapter 2, which was originally published in Magnetic Resonance in Medicine. Financial support was partially provided by the American Health Assistance Foundation (National Heart Foundation).

Special thanks go to my parents and my brother. It is their support that encourages me to pursue, persist, and accomplish my doctoral study. Finally, I thank everybody who helped make the successful realization of this dissertation.

TABLE OF CONTENTS

LIST OF TABLES

LIST OF FIGURES

GLOSSARY

ACE-I	Angiotensin-converting-enzyme inhibitor
ANOVA	Analysis of variance
CACS	Coronary artery calcification score
CIM	Complete isolation media
CNR	Contrast-to-noise ratio
CT	Computed tomography
CTA	Computed tomography angiography
CV	Coefficient of variance
CVD	Cardiovascular disease
ECG	Electrocardiogram
EPC	Endothelial progenitor cells
ESC	Embroic stem cells
FA	Flip angle
FDA	Food and drug agent
FDG	^{18}Fluorodeoxyglucose
FOV	Field of view
Gd-DTPA	Gadolinium diethylenetriaminepentaacetic acid
GEFC	Gradient echo sequence with flow compensation
GFP	Green fluorescent protein
LVEDV	Left ventricular end-diastolic volume
LVEF	Left ventricular ejection fraction
LVESV	Left ventricular endo-systolic volume
MI	Myocardial infarction
MION	Monocrystalline iron oxide nanoparticles
MNC	Mononuclear cells
MPIO	Micrometer-sized iron oxide particles
MR	Magnetic resonance
MRI	Magnetic resonance imaging

MRS	Magnetic resonance spectroscopy
MSC	Mesenchymal stem cells
NA	Not applicable
nSI	Normalized signal intensity
PFA	Paraformaldehyde
PBS	Phosphate-buffered saline
PET	Positron emission tomography
RES	Reticuloendothelial system
RF	Radio frequency
ROA	Rate of attenuation
ROI	Region of interest
SD	Standard deviation
SEM	Standard error of mean
SPECT	Single photon emission computed tomography
SPIO	Superparamagnetic iron oxide particles
SSPIO	Standard superparamagnetic iron oxide particles
SV	Stroke volume
TE	Echo time
TR	Repetition time
USPIO	Ultra-small superparamagnetic iron oxide particles

SUMMARY

The cell infiltration into the myocardial infarction (MI) site was studied using magnetic resonance imaging (MRI) with micrometer-sized iron oxide particles (MPIO) as cell labeling probes. MI is a leading cause of global death and disability. However, the roles of inflammatory cells and stem cells during the post-MI remodeling and repair processes are yet to be discovered. This study was to develop noninvasive MRI techniques to monitor and quantify the cellular infiltration into the MI site. MPIO can produce pronounced signal attenuation at regions of interest in MRI. Therefore, cells labeled with these particles can be detected after they are activated and home to the MI site. In the first project, MPIO of various doses were injected into the mouse blood stream 7 days before the MI surgery. Serial MRI was performed at various time points post-MI to monitor the inflammatory cell infiltration into the MI site. Significant signal attenuation caused by labeled cells, in particular macrophages, was observed at the MI site. The study suggests an optimal imaging window should be from 7 to 14 days post-MI, during which the MR signal was inversely proportional to the MPIO dose. The study also suggests an optimal MPIO dose should be between 9.1 and 14.5 μg Fe/g body weight. In the second project, mesenchymal stem cells labeled with MPIO were transplanted into the mouse bone marrow 14 days before the MI surgery. Serial MRI was performed at various time points post-MI to monitor the labeled cells, which mobilized from the bone marrow and homed to the MI site. All the MRI findings were further confirmed by histology. In addition to revealing the characteristics of cell infiltration during MI, this study also provides noninvasive MRI techniques to monitor and potentially quantify labeled cells at the pathological site. The technique can also be used to investigate the function of cells engaged in MI and to test the effect on cell infiltration caused by any treatment strategies.

CHAPTER 1
BACKGROUND

1.1 CARDIOVASCULAR DISEASE

Cardiovascular disease (CVD) is one of the leading causes of death and disability worldwide. CVD accounts for about 16.7 million deaths, which is 29.2% of all deaths in the world according to the World Health Organization[1]. CVD represents a major economic burden on healthcare systems in developed countries[2]. As the number of obese people and aging population increase, the cost associated with CVD is likely to grow. It is reported that CVD accounted for 34.2% (829,072) of all deaths in the United States in 2006 and the cost of CVD was estimated to be $475.3 billion[3]. Of all types of CVD, coronary heart disease accounted for more than 50%. Figure 1.1 illustrates the percentage breakdown of deaths due to CVD in the United States in 2006.

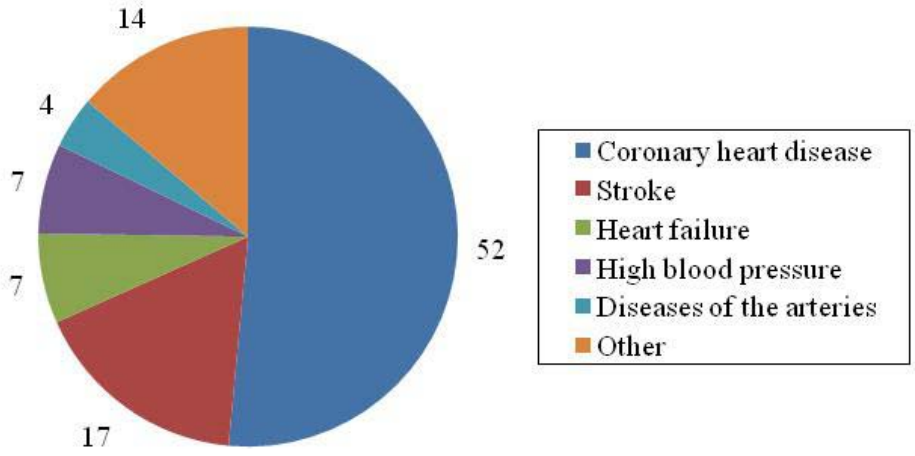

Figure 1.1 Percentage breakdown of deaths due to CVD in the United States in 2006. Source: National Center for Health Statistics (NCHS). Numbers are rounded. Adapted from Lloyd-Jones et al[3].

Medical imaging plays important roles in the diagnosis and treatment of CVD. Many established imaging protocols have been applied to the routine clinical procedures. For instance, nuclear medicine imaging methods have become one of the standard clinical procedures to assess cardiac function. Positron emission tomography (PET) and single photon emission computed tomography (SPECT) are widely used in nuclear medicine to detect coronary artery diseases following the injection of radiopharmaceuticals such as ^{99m}Tc-Sestamibi and ^{18}fluorodeoxyglucose (FDG). Unlike those imaging modalities utilizing radiation, magnetic resonance imaging (MRI) precludes the risk to patients caused by any radiation exposure. Since MRI is able to achieve a better soft tissue contrast, anatomical changes caused by cardiac disease can thus be detected even without any administration of contrast media. For example, serial cardiac images (also referred as cine cardiac MRI) can be acquired at various times during the cardiac cycle to measure the cardiac output and ejection fraction, and consequently to evaluate cardiac function. Abnormalities in the ventricular wall motion and thickness can also be detected. Cardiac MRI becomes even more powerful with contrast agent enhancement. Using gadolinium-enhanced MRI to detect alteration of myocardial perfusion and myocardial viability caused by coronary artery diseases has already been established as a standard clinical procedure[4-7]. With the development of novel imaging sequences and parallel imaging techniques, MRI can achieve its tremendous potentials in the prognosis of cardiac coronary diseases. More information regarding different imaging modalities and contrast agents will be introduced in the following sections.

1.2 MYOCARDIAL INFARCTION

Myocardial infarction (MI), also known as a heart attack, is a process of cell death caused by the shortage or interruption of blood supply to the affected myocardium. The causes can be either partial or complete occlusion of one or more coronary arteries. It is widely recognized that to a large extent occlusion of a coronary artery is caused by a thrombosis[8]. The thrombosis induced by rupture of a coronary atherosclerotic plaque can block the blood flow and thus stop the oxygen supply to the affected cardiac area.

Following rupture of an atherosclerotic plaque, coagulating factors such as platelets and red blood cells aggregate in the site and form a fibrin-containing clot. If no collateral blood vessel develops following the obstruction, the shortage of blood flow to the affected myocardium causes cell death, either necrosis, apoptosis, or both. Cellular changes occur within 20 minutes after coronary artery occlusion, including phosphocreatine and creatine depletion, intracellular edema, and myocyte distortion[9]. Within the first hour of blood interruption, mitochondria swelling and nuclear chromatin margination are observed. Neutrophils infiltration and digestion process start within 6 hours after occlusion. These cells release phosphorylase, endopeptidase and oxidative enzymes after they reach the infarction site. By 24 hours after occlusion, the myocyte nucleus disappears and myofibrils are stretched due to ventricular contraction. A few days after occlusion, macrophages migrate to the infarction site and remove the debris. Granulation tissue can be observed at 10 days after occlusion. Collagenization and neovascularization processes continue and last for several weeks.

As previously stated, the term myocardial infarction reflects cell death of cardiac myocytes caused by ischemia. Possible ischemic symptoms include various combinations of chest, upper extremity, jaw, or epigastric discomfort with exertion or at rest[10]. The discomfort associated with acute MI usually lasts at least 20 min. MI may be detected only by ECG, biomarker elevations, or cardiac imaging, with atypical symptoms or even without symptoms. By size, MI can be classified as microscopic (focal necrosis), small (<10% of the left ventricular myocardium), moderate (10-30% of the left ventricular myocardium), and large (>30% of the left ventricular myocardium)[10]. From onset of a MI until a scar formation, MI can be temporally breakdown into four stages: evolving (<6 hr), acute (6 hr–7 days), healing (7–28 days), and healed (29 days and beyond)[10]. Evolving infarction is referred to as the stage between onset of a MI and the initiation of myocyte cell death. Around 6 hours after onset, polymorphonuclear leukocytes start to infiltrate into the MI site. The presence of these cells characterizes the stage of acute MI. Healing infarction is characterized by the absence of polymorphonuclear leukocytes, and the infiltration of mononuclear cells (MNCs) and fibroblasts. The appearance of scar tissue marks a healed infarction.

Most clinical infarctions involve the left ventricle, and the right ventricular infarction is less common. MI can result in the damage of myocardial tissue, abnormality of ventricular wall motion and finally the decline of cardiac function. Due to the loss of myocardium, the ventricular wall at the infarction site can become as thin as a paper. The left ventricular ejection fraction (LVEF) can be undermined so severely that the blood supply cannot meet the demand, finally leading to heart failure and death. In patients with heart failure, serial measurements of LVEF provide important prognostic information[11].

Other important assessments include left ventricular volume, wall thickness and valve function.

Many cell types involve in the post-MI myocardial remodeling and repair processes. Inflammatory cells such as monocytes/macrophages home to the infarction site and remove the necrotic tissue debris during the healing stage (7–18 days). Stem cells such as messenchymal stem cells migrate to the injured site and try to repair the damaged myocardium. Stem cells are critical for potential myocardial tissue regeneration and currently are highlighted research subjects in cardiac cell therapy.

1.2.1 Inflammatory Response in MI

Inflammation plays a vital role in the process of post-infarction myocardial remodeling. Inflammatory reaction is a prerequisite for post-infarction healing and scar formation. Reperfusion of the infarcted myocardium is accompanied by substantial enhancement of inflammatory response. However, augmented inflammatory response can result in deleterious ventricular remodeling, ultimately leading to heart failure.

Myocardial cell death caused by interruption of blood supply results in the breakdown of cellular components and membrane structures. These membrane fragments can trigger complement cascade and initiate the complement-mediated inflammatory response[12,13]. Myocardial cell death is also associated with an upregulation of reactive oxygen species, which are molecules with unpaired electrons. These reactive oxygen species exert direct hazard to myocardial cells. Complement activation, reactive oxygen species, and their mutual interaction may be involved in triggering inflammatory cascades through the induction of cytokines[14-16]. The resident mast cell degranulation

following myocardial infarction results in rapid release of tumor necrosis factor-alpha (TNF-α), which serves as a trigger of cytokine cascade and mononuclear cell infiltration[17,18].

The cell-mediated inflammatory process begins with recruitment and infiltration of neutrophils, which may be capable of amplifying cell recruitment through release of oxidants and proteases[19,20]. Following initiation of inflammatory response, neutrophils migrate to the affected myocardium and rapidly change their shape as well as deformability, which is induced by chemotactic factors. The changes in shape and deformability, and interactions with endothelial cells via adhesion molecules (e.g., selectins and integrins) result in the adherence of neutrophils to the endothelium as well as the transendothelial migration into the extravascular inflamed tissue. Following ligand-specific adhesion to myocardial cells, neutrophils can release toxic products such as proteolytic enzymes and reactive oxygen species, which can directly injure the surrounding cardiac myocytes[21,22].

Following the phase of neutrophil infiltration is mononuclear cell infiltration. Monocytes differentiate into macrophages after they are recruited into the infarcted myocardium. Although it warrants further investigation to elucidate the exact roles of the macrophages in the post-MI healing process, the fact that the beneficial effects of reperfusion accompanied by enhanced monocyte infiltration suggests that macrophages may promote the effective myocardial repair[23,24]. Macrophages and mast cells may be capable of supporting fibrosis and neovacularization by secreting cytokines and growth factors[25,26,27], however, a clear definition of their roles requires further investigations. Lymphocytes also infiltrate into the ischemic and reperfused myocardium, mediating the

healing process by modulating mononuclear cell phenotypes[28]. Recruitment and infiltration of mast cells, monocytes/macrophages, and lymphocytes form a unique environment rich in inflammatory cells, which play indispensible roles in debris clearance, fibrosis, neovascularization and extracellular matrix remodeling. In addition to being a major component of regulating scar formation, fibroblasts also support neovascularization, which can bring oxygen and nutrients to the healing myocardium[29-32].

The inflammatory response is the key in the post-MI remodeling and repair process, and thus is determinant for the patient outcome[33]. Augment of pro-inflammatory cytokine cascades can result in the deterioration of left ventricular function. Therefore, modulation of the pro-inflammatory cytokine cascades can potentially reverse the downfall of left ventricular function[34]. This type of approaches are usually called anti-inflammatory strategies, which have been used in the treatment of MI[35-37]. For instance, angiotensin-converting-enzyme inhibitors (ACE-Is) have demonstrated efficacy in preventing deterioration of left ventricular function, partially due to their anti-inflammatory effects on reducing the expression of pro-inflammatory cytokines[38,39]. Statin (or HMG CoA reductase inhibitors) is another class of anti-inflammatory drugs used to ameliorate post-MI cardiac function[40,41]. However, it is still open to debate whether or not it is the anti-inflammatory mechanism that causes cardiac function improvement and how the mechanism works[34,42]. Apparently, a better understanding of molecular interactions and inflammatory mechanisms involved in the MI is needed in order to develop effective and specific therapeutic strategies that can minimize inflammatory injury and maximize myocardial repair.

1.2.2 Roles of Monocytes/Macrophages in MI

After MI, occlusion of a coronary artery jeopardizes the affected myocardium and induces myocardial cell death due to diminished or obstructed blood oxygen supply. The cell necrosis triggers the inflammatory process through release of cytokines and chemokines. During the inflammatory process, circulating monocytes respond to the chemotactic signals, migrate into the infarction site and differentiate into macrophages. The macrophages play many pivotal roles during the myocardial remodeling. At the infarction site, for example, the macrophages clear necrotic myocytes and apoptotic neutrophils; they also secrete cytokines, chemokines and growth factors which contribute to inflammation cascade and regulate multiple healing events such as scar formation and angiogenesis[27]. The inflammatory response is essential for post-MI ventricular remodeling and the roles of macrophages are of fundamental importance in this process. The primary functions of macrophages are listed in Table 1.1.

Table 1.1 Primary functions of macrophages

Function	Role post-MI
Phagocytosis	Remove necrotic myocytes and apoptotic neutrophils
Chemotaxis	Recruit additional macrophages to injury site to amplify response
Secretion	Regulate scar formation by secreting growth factors, angiogenic factors, and matrix metalloproteinases
Angiogenesis	Restore blood flow

Adapted from Lambert et al[27].

1.2.3 Roles of Stem Cells in MI

Apart from macrophages, stem cells may also play fairly important roles in the post-MI repair mechanism[43]. In the adult heart, cardiac myocytes enter into a post-mitotic state and lose the capability of proliferation and differentiation. In the condition of MI, cardiomyocytes would enlarge to compensate for the declined cardiac function rather than proliferate to repair the damaged tissue. An estimated 10-40% of MI patients are likely to develop heart failure, since the scar tissue healing over the necrosed myocardium contains mononuclear and fibroblast cells, but rare contractile or pacemaker myocytes[10,44]. The lack of cardiomyocyte progenitors limits the capability of the heart to regenerate itself.

Current therapeutic approaches are constrained by the fact that an adult heart has a limited capacity of regeneration, and thus concentrated at slowing disease progression instead of repairing the damaged tissue and restoring cardiac function. The goal of finding a once-and-for-all solution for MI motivates scientists and cardiologists to investigate alternative therapeutic strategies. As a promising alternative, stem cell therapy has recently been widely explored, attempting to regenerate myocardial tissue at the MI site and impede heart failure development. The exact roles of stem cells in the myocardial repair and remodeling processes are not well understood and clinical studies have produced mixed results[45,46]. However, *in vitro* cell culture and animal experiments have yielded exciting results after stem cells were transplanted into the infarcted heart. Whereas there is a wide debate about whether stem cells can engraft to and couple with the myocardium and improve cardiac function, clearly more efforts are warranted before those promising aspects of preclinical results can be translated to the bedside.

Many cell types such as embryonic stem cells (ESC)[47], human ESC-derived cardiomyocytes[48], skeletal myocytes[49], and bone marrow-derived stem cells[50,51] have been transplanted into the infarcted myocardium in both animal and human models to determine their beneficial effects. However, complications have occurred when embedding these cells into the myocardium. For example, ESC may cause an adverse immunological response and/or teratoma formation[52]; successful differentiation of human ESC-derived cardiomyocytes involves a highly complex process not easily performed[53]; and engrafted skeletal myocytes may fail to functionally integrate with the host tissue[54]. Mesenchymal stem cells (MSC) may be a better therapeutic option since they exhibit a multi-lineage plasticity, a reduced immune response, and are easy to harvest[55,56]. Previous research by Quevedo et al[57] showed that MSC were capable of restoring cardiac function via trilineage differentiating capacity. Table 1.2 summarizes many potential cell types as well as their respective advantages and disadvantages for MI cell therapy. Table 1.3 summarizes some recent clinical trials using bone marrow-derived cell transplantation for treating acute MI. The outcomes were mixed and the exact roles that stem cells play in post-MI remodeling are yet to be discovered.

How stem cells or progenitor cells mediate the post-MI repair process and consequently improve cardiac function is still unknown. While some types of stem cells may have potential of regenerating the myocardium, they may also contribute to myocardial repair via neovascularization[58,59] and modulation of inflammatory response[60,61]. Ciulla et al demonstrated that bone marrow MNCs selectively homed to the injured myocardium and contributed to the vessel formation[58]. Kawamoto et al showed that intramyocardial transplantation of autologous endothelial progenitor cells

significantly enhanced neovascularization in the myocardial ischemia[59]. Ciulla et al investigated the effects of bone marrow MNC therapy on pro-inflammatory cytokines and on left ventricle remodeling, and compared these effects over a standard ACE-I therapy in a rat model of myocardial injury. They found that both bone marrow MNCs and ACE-I reduced the expression of pro-inflammatory cytokines and contributed to the prevention of left ventricular function deterioration[61].

Table 1.2 Advantages and disadvantages of potential cell types for MI cell therapy

Cell types	Advantages	Disadvantages
Fetal/neonatal cardiomyocytes	• Establish E-M coupling • High proliferative capacity • Genetic engineering	• Ethical/moral issues • Donor availability • Poor long-term survivability • Immune rejection • Sensitive to ischemic injury
Embryonic stem cells	• Pluripotent • Establish E-M coupling • Genetic engineering	• Ethical/moral issues • Difficult scalability • Allogenic immune rejection • Deficient characterization
Skeletal myoblasts	• Ease of isolation and culture scalability • Autologous source • Ischemia resistance • Genetic engineering	• Inability to establish E-M coupling • Potential arrhythmias • Uncontrolled proliferation
Endothelial progenitor cells	• Ease of isolation and culture scalability • Autologous source • Genetic engineering	• Insufficient characterization
Bone marrow derived mesenchymal stem cells	• Multipotent • Ease of culture and isolation • Autologous source • Genetic engineering	• Difficult scalability • Deficient characterization
Smooth muscle cells	• Ease of isolation and culture scalability • Secrete angiogenic factor • Autologous source	• Inability to establish E-M coupling • Potential arrhythmias

Note: E-M coupling: electro-mechanical coupling. This table is adapted from Dib et al[62].

Table 1.3 Randomized clinical trials using bone marrow-derived cell transplantation for acute MI treatment

Study	Cell type	Time after MI (days)	Significant improvement	No change
Strauer[63]	MNC	5–9	Regional wall motion, infarct size, perfusion	LVEF, LVEDV
Assmus[64]	EPC/ MNC	5 ± 2	Regional wall motion, LVEF, infarct size	LVEDV
Wollert[65]	MNC	6 ± 1	Regional wall motion, LVEF, infarct size	LVEDV, infarct size
Chen[66]	MSC	18	Regional wall motion, LVEF, LVEDV	NA
Bartunek[67]	CD133+	11.6 ± 1.4	Regional wall motion, LVEF, infarct size	NA
Janssens[68]	MNC	1	Regional wall motion, infarct size	LVEF, LVEDV
Lunde[69]	MNC	4–6	NA	LVEF, infarct size
Schächinger[70]	MNC	3–6	LVEF, long-term clinical outcome	LVEDV

Note: LVEDV: left ventricular end-diastolic volume; EPC: endothelial progenitor cells; NA: not applicable. Adapted from Charwat et al[43].

1.3 CARDIAC IMAGING MODALITIES

Previously, electrocardiogram (ECG) and coronary catheterization (also called coronary angiography) have been the primary methodologies for the diagnosis and prognosis of cardiovascular disease. However, the limited sensitivity of ECG, and the poor regional resolution and invasive nature of coronary catheterization necessitate the development of additional imaging techniques that can simultaneously provide complementary information on heart anatomy, cardiac function, and myocardial perfusion and viability. Echocardiography is able to provide more anatomic information which can reflect changes in cardiac tissue structure as well as wall motion. Furthermore, SPECT and PET have been established as functional imaging tools well suited for diagnosis of cardiovascular diseases. Nuclear cardiac stress testing has become a routine clinical procedure to detect coronary artery diseases and to prevent further morbidity or mortality. Since the 1970s, dramatic advances have occurred in imaging technology, such as in design of radiation detectors and superconductive magnets, driving the tremendous evolution in computed tomography (CT) and MRI technology. At present, CT and MRI are being used increasingly for routine diagnosis and prognosis. Along with PET, SPECT and echocardiography, CT and MRI have become the major imaging methodologies for cardiovascular diagnosis.

1.3.1 Echocardiography

Echocardiography has made a significant contribution to the evolution of cardiac imaging as a noninvasive, convenient and inexpensive imaging methodology. Echocardiography is a simple, widely accessible technique for evaluation of ventricular function and initiation of either further detailed diagnosis or proper therapeutic strategies.

The advantages of echocardiography lie in its high temporal resolution, simplicity and bedside portability.

Echocardiography is widely used in the measurement of ventricular blood flow velocities, and cardiac tissue velocities and stains. In this manner, echocardiography has been used in the diagnosis of left ventricular dissynchrony[71], characterization of the myocardial scar tissue[72], evaluation of hypertrophic cardiomyopathy[73], and assessment of valve dysfunction[74]. However, applications of echocardiography in cardiac imaging are limited by its inherent shortcomings: poor image quality, lack of detailed anatomic information and consequently difficulty in interpretation. While some new techniques in echocardiography including contrast enhancement and three-dimensional echocardiography are now under development and have potential in supporting its position in cardiac imaging[75], many of its roles are now filled by other imaging modalities such as PET, CT and MRI.

1.3.2 CT

The enormous advancement in CT technology has tremendously enhanced both temporal and spatial resolution of modern CT systems. CT systems have evolved rapidly from single-slice to multi-slice imaging (64-slice systems are now available in routine diagnosis), allowing acquisition of a three-dimensional data set in a few seconds. In addition, improved spatial resolution renders much better visualization and more accurate quantitative analysis. The increased temporal resolution enables the gantry to finish one rotation in tenths of a second, significantly reducing the artifact caused by the motion of the heart. On the other hand, the increased spatial resolution allows reconstruction of a

voxel as small as 0.5x0.5x0.5 mm^3, which is feasible to visualize and diagnose the coronary arteries.

Recently, CT has been used to define the cardiac anatomy[76], evaluate cardiac function[77,78] and image the great vessels as well as coronary arteries[79,80]. Since CT imaging is based on the detection of transmitted x-ray through the human body, the best contrast is achieved between soft tissue and targets of interest with a relatively high atomic number. In this manner, CT is a superb modality for differentiation of coronary calcification[81,82]. Similarly, CT angiography can provide well defined images of blood-containing structures including atria, ventricles and blood vessels, following injection of the iodinated contrast media.

However, the principle of utilizing radiation to reconstruct the images unavoidably creates a potential hazard to patients. Recently, the relatively high dose in CT imaging has drawn intensive concern. For instance, coronary CT angiography engages continuous radiation exposure and thus can lead to a considerably high dose[83]. Table 1.4 presents some common CT procedures and their corresponding patient dose. Furthermore, CT does not have soft tissue contrast as good as that obtained from MRI. A relatively large radiation dose is required in order to achieve sufficient soft tissue contrast, which could result in significant radiation exposure to the patient. CT also faces challenges when it is used to evaluate cardiac function and quantify heart parameters. The large dose caused by the continuous radiation exposure during cardiac loops greatly restricts the application of functional CT to patients. Neither is CT a good option of performing repeatable longitudinal diagnosis, which otherwise would result in a considerable radiation dose to patients.

Table 1.4 Effective dose and background equivalent years for diagnostic coronary angiograms and selected CT examinations.

CT procedures	Effective dose (mSv)	Background equivalent years
Coronary angiogram	3-25	1-7
Coronary CTA	7-13	2-4
Prospective CACS	1.5-3.6	0.4-1
Chest CT	5-7	1.4-4
Abdomen/pelvis CT	8-11	2-3
Average US annual background	3.6	1

Note: the average annual background includes medical exposure. CTA: CT angiography; CACS: coronary artery calcification score. Adapted from Westerman[83].

1.3.3 PET and SPECT

Nuclear medicine has been well established as a routine methodology for diagnosis and prognosis of coronary artery diseases. The biochemical environment of cardiac tissue changes when the heart undergoes a pathological condition, which results in a discontinuous distribution of radiopharmaceuticals in the myocardium. Nuclear medicine techniques are sensitive to detect the reduced concentration of radiopharmaceuticals caused by decreased myocardial perfusion/metabolism and consequently to identify the regions undergoing coronary artery diseases. The prognosis of ischemic cardiac diseases is based on the extent of myocardial ischemia and the degree of ventricular remodeling. SPECT and PET can provide information on myocardial metabolism, perfusion and cardiac function simultaneously, and thus are well suited for studying cardiac ischemic diseases[84].

The advent of numerous radiopharmaceuticals has contributed significantly to the extensive use of PET and SPECT in cardiology and the maturation of nuclear medicine methodology. The first radiotracer applied in nuclear medicine is ^{131}Cs, dating back to

1964[85]. At the present time, three ^{99m}Tc-labeled tracers have been approved by the United States Food and Drug Administration (FDA): Sestamibi, Teboroxime and Tetrofosmin[86]. ^{99m}Tc has advantages compared with its predecessor ^{201}Tl, which has a low energy spectrum and long physical half life. Two positron emitters, ^{13}N and ^{82}Rb, are commonly used in PET imaging. The characteristics of common radiopharmaceutical are presented in Table 1.5. Following injection of radiopharmaceuticals, PET and SPECT are used in the diagnosis and prognosis of cardiovascular diseases to assess cardiac parameters such as ejection fraction and wall motion[87], examine myocardial viability and perfusion[88], and estimate the extent of ischemia[89]. However, the diagnosis efficacy of nuclear medicine techniques is limited by their low spatial resolution, which is especially true for SPECT due to the poor correction of photon attenuation and scattering. In addition, each nuclear medicine procedure requires an administration of radiopharmaceuticals which accumulate not only in the heart but also in other healthy organs such as brain and bladder and thus inevitably expose the patient to radiation risk.

Table 1.5 Characteristics of SPECT and PET radiopharmaceuticals

Modality	Tracer	Dose (MBq)	Energy (KeV)	Physical half-life	Time to imaging from injection
SPECT	^{201}Tl	111-166.5	80	1-15 min	73 hrs
	^{99m}Tc-Sestamibi ^{99m}Tc-Tetrofosmin	296-1480	140	15-45 min	6 hrs
PET	^{82}Rb	1110-2220	511	80 sec	75 sec
	^{13}N-Ammonia	370-740	511	6 min	10 min

Adapted from Vesely et al[86].

1.3.4 MRI

In the past decades, tremendous advances in the field of nuclear magnetic resonance have taken place. In hardware, a superconductive magnet that can provide as high as seven Tesla is common now for the purpose of translational studies. Three-Tesla MRI systems are now commonly used in routine clinical diagnosis. Including design of more efficient radio frequency (RF) and gradient coils as well as development of more specific contrast agents, all these innovations have dramatically improved the quality of MRI images. Furthermore, the development of parallel imaging and design of new imaging sequences allow cardiac image acquisition to occur within just a couple of heart beats, which dramatically improves the temporal resolution. In addition, the intensive research efforts and promising outcomes in cardiac magnetic resonance spectroscopy (MRS) can potentially translate this quantitative imaging method from benchside to bedside, leading to more accurate diagnosis and prognosis in the future.

MRI can provide cardiac images with high quality and reproducibility, which makes it a standard reference in the display of cardiac anatomy and measurement of ventricular function. Cardiac MRI has been accepted as a competitive or even superb methodology in the detection of myocardium viability and diagnosis of coronary artery diseases compared with echocardiography and nuclear medicine[90-92]. Gadolinium-enhanced MRI has been widely used in the diagnosis of myocardial infarction. Hypoperfused myocardium in coronary artery disease can be visualized by using first-pass gadolinium-enhanced MRI[93]. Bertschinger et al[94] demonstrated that first-pass gadolinium-enhanced MRI can not only delineate the perfusion defect due to coronary artery stenosis, but also the transmural distribution of the perfusion abnormality.

Myocardium viability can be detected and assessed with late gadolinium-enhanced MRI. The high image quality and sufficient contrast by gadolinium enhancement enable cardiac MRI to provide an accurate estimation of the location, extent and detailed distribution of the viable myocardium[95,96].

MRI has improved spatial resolution compared with other modalities. The high resolution allows cardiac MRI not only to differentiate the perfusion-defective myocardium from normal myocardium, and distinguish viable from nonviable myocardium, but to disclose the transmural extent of the MI. As mentioned earlier, the poor image quality of echocardiography results in 15% of echocardiographic images being suboptimal or nondiagnostic[92]. Nuclear medicine modalities are limited either by the lack of photon attenuation correction in SPECT, or by high cost for PET diagnosis. In addition, both PET and SPECT involve radiation exposure to patients. Another advantage of MRI is its flexibility in localization of an imaging plane in two-dimensional imaging. In MRI an image plane can be set in an arbitrary direction because choosing an imaging plane is achieved solely by changing the magnetic field gradient. This is important in cardiac MRI because the human heart is in an oblique direction, and transverse imaging slices are commonly interpreted. These factors make MRI a superior cardiac imaging modality for repeated imaging in diagnosis, prognosis and monitoring effects of therapeutic interventions. However, it is worth noting that the outcome of contrast-enhanced cardiac MRI is strongly dependent on the parameters of sequences applied. In addition, it is occasionally necessary to make correction for the signal attenuation resulted from increased distance to the RF coil. Another potential drawback of MRI is the potential hazard due to deposition of the RF energy in the patient's body.

1.3.5 Hybrid Systems

Each modality has its own advantages and disadvantages and therefore plays a unique role in the diagnosis and prognosis of cardiovascular diseases. Table 1.6 presents a summary of common applications of the four imaging modalities described above. Patients usually go through multiple rather than a single imaging modality, which provides complementary information and improves the efficacy and accuracy of diagnosis. Recently, hybrid systems physically integrating two imaging modalities have been developed and applied, allowing acquisition of spatially registered images simultaneously. At present, PET/CT and SPECT/CT are very common in the diagnosis of cardiovascular disease. CT provides high resolution images of coronary anatomy, and at the same time, PET or SPECT identifies the physiological consequences of abnormalities in specific coronary arteries. On the other hand, the anatomic information acquired from CT can be used to compute the attenuation map for PET/SPECT. Now hybrid systems integrating PET and MRI are also available in the market. In addition to its independent imaging capabilities, MRI also fills the role of providing anatomy for PET in PET/MRI as CT does in PET/CT.

Table 1.6 Capacities of various imaging modalities in cardiac imaging

Modality	Cardiac anatomy	Coronary artery structure	Ventricular function	Invasive	Radiation
Catheterization	Yes	Yes	No	Yes	Yes
Echocardiography	Yes	No	Yes	No	No
PET, SPECT	Yes	No	Yes	No	Yes
CT	Yes	Yes	Yes	No	Yes
MRI	Yes	Yes	Yes	No	No

1.4 MOLECULAR MRI AND CONTRAST AGENTS

Molecular imaging uses noninvasive, repeatable imaging methods to monitor the *in vivo* biological processes under normal or pathological conditions. The imaging modalities usually include optical imaging, nuclear medicine and MRI. Molecular imaging has been advanced by the advent of target-specific imaging probes. For example, fluorescent and bioluminescent proteins have been widely used in optical imaging as reporter genes to target interested cell lines, and FDG in PET to target the enzyme metabolism. Recently, the potential of MRI for molecular imaging has been extensively explored, with a large number of imaging probes designed, tested and applied. These magnetic resonance (MR) contrast agents are able to increase (positive contrast agents) or decrease (negative contrast agents) signal intensity by altering tissue relaxation times T_1 and/or T_2. Hence, an improved image contrast between targeted tissue and background can be achieved.

As a non-radiation imaging approach, MRI is a powerful tool for imaging morphological and functional changes due to its high spatial and temporal resolution. In molecular imaging, the sensitivity of MRI can be further increased by using contrast agents that can recognize and adhere to specific targets. The MR contrast agents are usually separated into two categories: paramagnetic contrast agents and superparamagnetic contrast agents. Whereas paramagnetic contrast agents primarily shorten T_1 and thus result in a brighter signal in the target, superparamagnetic contrast agents primarily shorten T_2 and thus lead to signal attenuation in the target. Table 1.7 presents the differences between these two types of contrast agents.

Table 1.7 Properties of MR contrast agents

Comparison	Paramagnetic	Superparamagnetic
T_1 Effect	Strong	Weak
T_2 Effect	Weak	Strong
Signal intensity	Increase	Decrease
MR Sequence	T_1-weighted	T_2-weighted
Example	Gadolinium chelates	Iron oxide particles

Paramagnetic contrast agents are based on metal ions such as gadolinium (Gd^{3+}), manganese (Mn^{2+}) or europium (Eu^{3+}), that have a relatively large number of unpaired electrons. The unpaired electrons have a permanent magnetic moment. In aqueous solution, the electronic magnetic moment interacts with the magnetic moment of the nearby protons in water molecules. Random fluctuations of these dipolar interactions resulted from molecular motions reduce both the T_1 and T_2 relaxation times of the water protons[97]. The primary effect of paramagnetic contrast agents is to reduce T_1, and thus paramagnetic contrast agents are also called T_1 contrast agents. Paramagnetic metals are used in the form of chelates, which are complexes binding metal irons to ligands. The most commonly used clinical paramagnetic contrast agent is gadolinium chelates such as gadolinium diethylenetriaminepentaacetic acid (Gd-DTPA). Using chelates instead of free metal irons can reduce the toxicity of free irons and enhance the selective targeting to the tissue of interest.

Superparamagnetic contrast agents are small magnetic particles containing iron, and are also referred to as superparamagnetic iron oxide particles (SPIO). The atomic structures of commonly used metal ions for MR contrast agents are shown in Table 1.8.

SPIO consist of iron oxide crystals coated with polymeric matrix such as dextrin and polymer. SPIO primarily reduce T_2 relaxation time and thus are also called T_2 contrast agents. The widespread use of SPIO is partially due to their T_2^* effect. The T_2^* effect includes not only the decay of the transverse magnetic moment due to spin-spin interactions (T_2 relaxation), but the dephase caused by the inhomogeneity of the local magnetic field. The active components producing T_2 or T_2^* shortening effect in SPIO are iron oxide crystals. Each crystal contains multiple magnetic domains composed of either Fe_2O_3 or Fe_3O_4. The interactions of unpaired electrons in ferric and/or ferrous ion produce a magnetic moment for each magnetic domain. In the absence of a magnetic field, the magnetic moment of each magnetic domain is randomly distributed, leading to a net magnetic moment of zero. When an external magnetic field is applied, all the magnetic moments are forced to reorient and line up with the magnetic field, producing a magnetic field which is stronger than the simple algebraic summation of overall magnetic moments. This magnetic susceptibility is strong enough to disturb the local magnetic field during signal acquisition and cause inhomogeneity in the local magnetic field, shortening T_2 and T_2^* values and leading to signal attenuation in T_2 or T_2^* weighted MRI. Figure 1.2 illustrates the SPIO structure and reorientation of magnetic moments when an external magnetic field is applied.

Table 1.8 Electron configurations of metal ions used for contrast agents

Metal ion	Electron configuration	Unpaired electrons
Gd^{3+}	[Xe] $6s^0 4f^7 5d^0$	7
Mn^{2+}	[Ar] $4s^0 3d^5$	4
Fe^{2+}	[Ar] $4s^0 3d^6$	5
Fe^{3+}	[Ar] $4s^0 3d^5$	7

SPIO have a better biocompatibility compared to paramagnetic contrast agents. Gadolinium or manganese chelates distribute through the intravascular and extracellular space following their intravenous administration. A typical dose of 0.1–0.3 mmol/kg body weight is usually injected into patients in order to achieve a sufficient image contrast. This dose can lead to a relatively high concentration of gadolinium in the normal tissue. The requirement of relatively high concentration can also result in an osmolarity higher than that of the normal blood, which is particularly true for the ionic chelates[97]. The high osmolarity can create potential adverse effects for patients. In contrast, iron is a composition of the human body with abundance much higher than gadolinium or manganese. Iron exists in the human body in the form of haemosiderin, ferritin and transferrin. Normal liver contains approximately 0.2 mg Fe/gram and total iron store in the human body is as large as 3500 mg. The total amount of iron oxide for diagnostic MRI is about 50–100 mg, which is small compared to the normal iron store in the human body[98]. Chronic iron toxicity develops only after the iron concentration in the liver exceeds 4 mg Fe/gram[99]. Due to the strong superparamagnetic property of iron, usually a small iron dose is needed to achieve a sufficient image contrast, compared to gadolinium agents[100]. Therefore, SPIO agents are better suited for repeated measurements and serial MRI than paramagnetic agents are[101].

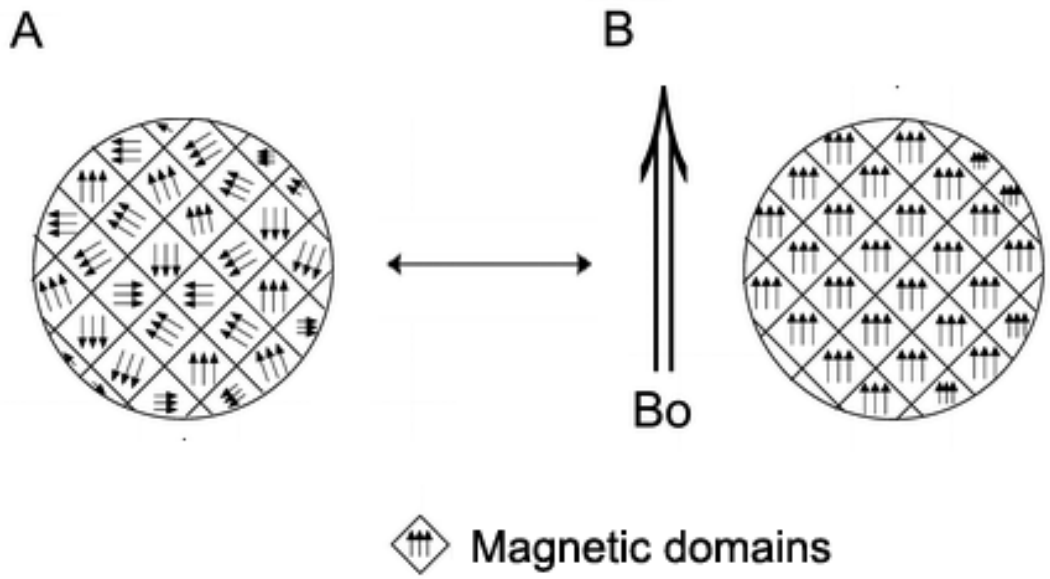

Figure 1.2 Structure of a single crystal of superparamagnetic iron oxide particles. A. Magnetic moments of individual domains are randomly oriented in the absence of an external field. B. Magnetic moments are reoriented and aligned with the magnetic field when an external magnetic field is applied. Adapted from Wang et al[101].

1.5 SPIO-ENHANCED MRI

According to the literature[101,102], iron oxide particles can be sized into four categories: micrometer-sized iron oxide particles (MPIO) have a diameter on the order of μm; standard SPIO (SSPIO) have a diameter of sub-micrometer but greater than 60 nm; ultrasmall SPIO (USPIO) of ~10-40 nm; and monocrystalline iron oxide nanoparticles (MION) of ~10-30 nm. Some literatures classify particles larger than 300 nm as oral SPIO due to their clinical applications in imaging the gastrointestinal system, during which particles are orally administered. The applications of MPIO as cell labeling probes are now being widely explored[103,104]. The preparation parameters such as size, coating and receptor or antibody conjugation, if any, determine the specialized applications of SPIO.

Generally, SPIO can work either as blood pool agents or as cellular and molecular agents. The low toxicity is an advantage of SPIO as a blood pool agent over other contrast media. The long circulating time in blood makes USPIO an effective blood pool agent. On one hand, USPIO have been widely applied in MR angiography for delineation of ventricular blood[105] and enhancement of blood vessels[106,107]. On the other hand, USPIO also act as a suitable candidate for perfusion imaging and have been applied in the brain[108], heart[109] and kidney[110] to differentiate the region with normal perfusion from those with abnormal perfusion. USPIO can also be used to characterize the abnormal vascularity in tumor angiogenesis[111].

Another burgeoning field is the application of SPIO as cell labeling probes in cellular and molecular imaging. SPIO labeling can be further divided into passive

targeting and active targeting. SPIO passive targeting is based on the fact that SPIO can be phagocytized by those cell types in the reticuloendothelial system (RES), such as macrophages and lymphocytes. In this manner, SPIO can be used to differentiate the pathological tissue containing an altered quantity of RES cells from the normal tissue in the liver[112], spleen[113], bone marrow[114] and lymph nodes[115], particularly for tumor diagnosis. Furthermore, SPIO have been widely used in inflammation imaging to detect inflammatory activities in the brain[116] and heart[117]. Passive targeting can also be used to label stem cells through the incubation of cells with SPIO. The labeled cells can be monitored after they are transplanted into the imaging subject[118,119]. Active targeting refers to cell labeling methods via the conjugation of SPIO with gene reporters or antibodies. By combining SPIO with gene markers that closely relate to a specific disease, the biologically engineered probes can specifically target a disease. Many cellular and molecular markers have been explored and tested in combination with SPIO, such as for imaging myocardial infarction[120] and angiogenesis[121], and to diagnose tumors[122].

1.6 REFERENCES

1. World Health Organization. Cardiovascular disease: Prevention and control. Global strategy on diet, physical activity and health. 2007.

2. Tarride JE, Lim M, DesMeules M, et al. A review of the cost of cardiovascular disease. Can J Cardiol 2009;25(6):e195-202.

3. Lloyd-Jones D, Adams R, Carnethon M, et al. Heart disease and stroke statistics--2009 update: a report from the American Heart Association Statistics Committee and Stroke Statistics Subcommittee. Circulation 2009;119(3):480-486.

4. Kitagawa K, Sakuma H, Nagata M, et al. Diagnostic accuracy of stress myocardial perfusion MRI and late gadolinium-enhanced MRI for detecting flow-limiting coronary artery disease: a multicenter study. Eur Radiol 2008;18(12):2808-2816.

5. Kachenoura N, Redheuil A, Herment A, et al. Robust assessment of the transmural extent of myocardial infarction in late gadolinium-enhanced MRI studies using appropriate angular and circumferential subdivision of the myocardium. Eur Radiol 2008;18(10):2140-2147.

6. Kurita T, Onishi K, Motoyasu M, et al. Two cases of dilated cardiomyopathy with right ventricular wall degeneration demonstrated by late gadolinium enhanced MRI. Int J Cardiol 2008;129(1):e21-23.

7. Kitagawa K, Ichikawa Y, Hirano T, et al. Diagnostic value of late gadolinium-enhanced MRI and first-pass dynamic MRI for predicting functional recovery in patients after acute myocardial infarction. Radiat Med 2007;25(6):263-271.

8. Libby P. Current concepts of the pathogenesis of the acute coronary syndromes. Circulation 2001;104(3):365-372.

9. Runge MS, Patterson C. Principles of molecular cardiology. Totowa, N.J.: Humana Press; 2005. xiii, 617 p219-221.

10. Thygesen K, Alpert JS, White HD. Universal definition of myocardial infarction. J Am Coll Cardiol 2007;50(22):2173-2195.

11. Cintron G, Johnson G, Francis G, et al. Prognostic significance of serial changes in left ventricular ejection fraction in patients with congestive heart failure. The V-HeFT VA Cooperative Studies Group. Circulation 1993;87(6 Suppl):VI17-23.

12. Pinckard RN, Olson MS, Giclas PC, et al. Consumption of classical complement components by heart subcellular membranes in vitro and in patients after acute myocardial infarction. J Clin Invest 1975;56(3):740-750.

13. Rossen RD, Michael LH, Hawkins HK, et al. Cardiolipin-protein complexes and initiation of complement activation after coronary artery occlusion. Circ Res 1994;75(3):546-555.

14. Birdsall HH, Green DM, Trial J, et al. Complement C5a, TGF-beta 1, and MCP-1, in sequence, induce migration of monocytes into ischemic canine myocardium within the first one to five hours after reperfusion. Circulation 1997;95(3):684-692.

15. Lefer DJ, Granger DN. Oxidative stress and cardiac disease. Am J Med 2000;109(4):315-323.

16. Frangogiannis NG, Smith CW, Entman ML. The inflammatory response in myocardial infarction. Cardiovasc Res 2002;53(1):31-47.

17. Gordon JR, Galli SJ. Mast cells as a source of both preformed and immunologically inducible TNF-alpha/cachectin. Nature 1990;346(6281):274-276.

18. Frangogiannis NG, Lindsey ML, Michael LH, et al. Resident cardiac mast cells degranulate and release preformed TNF-alpha, initiating the cytokine cascade in experimental canine myocardial ischemia/reperfusion. Circulation 1998;98(7):699-710.

19. Jordan JE, Zhao ZQ, Vinten-Johansen J. The role of neutrophils in myocardial ischemia-reperfusion injury. Cardiovasc Res 1999;43(4):860-878.

20. Frangogiannis NG, Youker KA, Entman ML. The role of the neutrophil in myocardial ischemia and reperfusion. EXS 1996;76:263-284.

21. Jaeschke H, Smith CW. Mechanisms of neutrophil-induced parenchymal cell injury. J Leukoc Biol 1997;61(6):647-653.

22. Entman ML, Youker K, Shoji T, et al. Neutrophil induced oxidative injury of cardiac myocytes. A compartmented system requiring CD11b/CD18-ICAM-1 adherence. J Clin Invest 1992;90(4):1335-1345.

23. Jugdutt BI. Effect of reperfusion on ventricular mass, topography, and function during healing of anterior infarction. Am J Physiol 1997;272(3 Pt 2):H1205-1211.

24. Weihrauch D, Arras M, Zimmermann R, et al. Importance of monocytes/macrophages and fibroblasts for healing of micronecroses in porcine myocardium. Mol Cell Biochem 1995;147(1-2):13-19.

25. Ruoss SJ, Hartmann T, Caughey GH. Mast cell tryptase is a mitogen for cultured fibroblasts. J Clin Invest 1991;88(2):493-499.

26. Metcalfe DD, Baram D, Mekori YA. Mast cells. Physiol Rev 1997;77(4):1033-1079.

27. Lambert JM, Lopez EF, Lindsey ML. Macrophage roles following myocardial infarction. Int J Cardiol 2008;130(2):147-158.

28. Frangogiannis NG, Mendoza LH, Lindsey ML, et al. IL-10 is induced in the reperfused myocardium and may modulate the reaction to injury. J Immunol 2000;165(5):2798-2808.

29. Gabbiani G. Evolution and clinical implications of the myofibroblast concept. Cardiovasc Res 1998;38(3):545-548.

30. Sun Y, Weber KT. Infarct scar: a dynamic tissue. Cardiovasc Res 2000;46(2):250-256.

31. Thai HM, Juneman E, Lancaster J, et al. Implantation of a three-dimensional fibroblast matrix improves left ventricular function and blood flow after acute myocardial infarction. Cell Transplant 2009;18(3):283-295.

32. Hasegawa T, Kimura A, Miyataka M, et al. Basic fibroblast growth factor increases regional myocardial blood flow and salvages myocardium in the infarct border zone in a rabbit model of acute myocardial infarction. Angiology 1999;50(6):487-495.

33. Nian M, Lee P, Khaper N, et al. Inflammatory cytokines and postmyocardial infarction remodeling. Circ Res 2004;94(12):1543-1553.

34. Tousoulis D, Antoniades C, Koumallos N, et al. Pro-inflammatory cytokines in acute coronary syndromes: from bench to bedside. Cytokine Growth Factor Rev 2006;17(4):225-233.

35. Kennedy TP, Vinten-Johansen J. A review of the clinical use of anti-inflammatory therapies for reperfusion injury in myocardial infarction and stroke: where do we go from here? Curr Opin Investig Drugs 2006;7(3):229-242.

36. Solomon DH, Glynn RJ, Levin R, et al. Nonsteroidal anti-inflammatory drug use and acute myocardial infarction. Arch Intern Med 2002;162(10):1099-1104.

37. Iabluchanskii NI, Vlasenko MA, Kopitsa NI, et al. The use of anti-inflammatory agents and stimulators of reparative processes in myocardial infarction. Vrach Delo 1989(5):22-25.

38. Schindler R, Dinarello CA, Koch KM. Angiotensin-converting-enzyme inhibitors suppress synthesis of tumour necrosis factor and interleukin 1 by human peripheral blood mononuclear cells. Cytokine 1995;7(6):526-533.

39. Wei GC, Sirois MG, Qu R, et al. Subacute and chronic effects of quinapril on cardiac cytokine expression, remodeling, and function after myocardial infarction in the rat. J Cardiovasc Pharmacol 2002;39(6):842-850.

40. Spencer FA, Allegrone J, Goldberg RJ, et al. Association of statin therapy with outcomes of acute coronary syndromes: the GRACE study. Ann Intern Med 2004;140(11):857-866.

41. Sposito AC, Carvalho LS, Cintra RM, et al. Rebound inflammatory response during the acute phase of myocardial infarction after simvastatin withdrawal. Atherosclerosis 2009;207(1):191-194.

42. Dzau VJ, Bernstein K, Celermajer D, et al. Pathophysiologic and therapeutic importance of tissue ACE: a consensus report. Cardiovasc Drugs Ther 2002;16(2):149-160.

43. Charwat S, Gyongyosi M, Lang I, et al. Role of adult bone marrow stem cells in the repair of ischemic myocardium: current state of the art. Exp Hematol 2008;36(6):672-680.

44. Weir RA, McMurray JJ, Velazquez EJ. Epidemiology of heart failure and left ventricular systolic dysfunction after acute myocardial infarction: prevalence, clinical characteristics, and prognostic importance. Am J Cardiol 2006;97(10A):13F-25F.

45. Murry CE, Field LJ, Menasche P. Cell-based cardiac repair: reflections at the 10-year point. Circulation 2005;112(20):3174-3183.

46. Menasche P. Cell-based therapy for heart disease: a clinically oriented perspective. Mol Ther 2009;17(5):758-766.

47. Yang L, Soonpaa MH, Adler ED, et al. Human cardiovascular progenitor cells develop from a KDR+ embryonic-stem-cell-derived population. Nature 2008;453(7194):524-528.

48. Kehat I, Khimovich L, Caspi O, et al. Electromechanical integration of cardiomyocytes derived from human embryonic stem cells. Nat Biotechnol 2004;22(10):1282-1289.

49. Menasche P. Skeletal myoblasts for cardiac repair: Act II? J Am Coll Cardiol 2008;52(23):1881-1883.

50. Carr CA, Stuckey DJ, Tatton L, et al. Bone marrow-derived stromal cells home to and remain in the infarcted rat heart but fail to improve function: an in vivo cine-MRI study. Am J Physiol Heart Circ Physiol 2008;295(2):H533-542.

51. Shyu KG, Wang BW, Hung HF, et al. Mesenchymal stem cells are superior to angiogenic growth factor genes for improving myocardial performance in the mouse model of acute myocardial infarction. J Biomed Sci 2006;13(1):47-58.

52. Nussbaum J, Minami E, Laflamme MA, et al. Transplantation of undifferentiated murine embryonic stem cells in the heart: teratoma formation and immune response. FASEB J 2007;21(7):1345-1357.

53. Laflamme MA, Chen KY, Naumova AV, et al. Cardiomyocytes derived from human embryonic stem cells in pro-survival factors enhance function of infarcted rat hearts. Nat Biotechnol 2007;25(9):1015-1024.

54. Leobon B, Garcin I, Menasche P, et al. Myoblasts transplanted into rat infarcted myocardium are functionally isolated from their host. Proc Natl Acad Sci U S A 2003;100(13):7808-7811.

55. Pittenger MF, Mackay AM, Beck SC, et al. Multilineage potential of adult human mesenchymal stem cells. Science 1999;284(5411):143-147.

56. Kawada H, Fujita J, Kinjo K, et al. Nonhematopoietic mesenchymal stem cells can be mobilized and differentiate into cardiomyocytes after myocardial infarction. Blood 2004;104(12):3581-3587.

57. Quevedo HC, Hatzistergos KE, Oskouei BN, et al. Allogeneic mesenchymal stem cells restore cardiac function in chronic ischemic cardiomyopathy via trilineage differentiating capacity. Proc Natl Acad Sci U S A 2009;106(33):14022-14027.

58. Ciulla MM, Ferrero S, Montelatici E, et al. Assessment of selective homing and contribution to vessel formation of cryopreserved peripherally injected bone marrow mononuclear cells following experimental myocardial damage. Cardiovasc Hematol Disord Drug Targets 2006;6(3):141-149.

59. Kawamoto A, Tkebuchava T, Yamaguchi J, et al. Intramyocardial transplantation of autologous endothelial progenitor cells for therapeutic neovascularization of myocardial ischemia. Circulation 2003;107(3):461-468.

60. Boyle AJ, Schuster M, Witkowski P, et al. Additive effects of endothelial progenitor cells combined with ACE inhibition and beta-blockade on left ventricular function following acute myocardial infarction. J Renin Angiotensin Aldosterone Syst 2005;6(1):33-37.

61. Ciulla MM, Montelatici E, Ferrero S, et al. Potential advantages of cell administration on the inflammatory response compared to standard ACE inhibitor treatment in experimental myocardial infarction. J Transl Med 2008;6:30-37.

62. Dib N, Taylor DA, Diethrich EB. Stem cell therapy and tissue engineering for cardiovascular repair : from basic research to clinical applications. New York, NY: Springer; 2006. xix, 335 p25-35.

63. Strauer BE, Brehm M, Zeus T, et al. Repair of infarcted myocardium by autologous intracoronary mononuclear bone marrow cell transplantation in humans. Circulation 2002;106(15):1913-1918.

64. Schachinger V, Assmus B, Britten MB, et al. Transplantation of progenitor cells and regeneration enhancement in acute myocardial infarction: final one-year results of the TOPCARE-AMI Trial. J Am Coll Cardiol 2004;44(8):1690-1699.

65. Wollert KC, Meyer GP, Lotz J, et al. Intracoronary autologous bone-marrow cell transfer after myocardial infarction: the BOOST randomised controlled clinical trial. Lancet 2004;364(9429):141-148.

66. Chen SL, Fang WW, Ye F, et al. Effect on left ventricular function of intracoronary transplantation of autologous bone marrow mesenchymal stem cell in patients with acute myocardial infarction. Am J Cardiol 2004;94(1):92-95.

67. Bartunek J, Croissant JD, Wijns W, et al. Pretreatment of adult bone marrow mesenchymal stem cells with cardiomyogenic growth factors and repair of the chronically infarcted myocardium. Am J Physiol Heart Circ Physiol 2007;292(2):H1095-1104.

68. Janssens S, Theunissen K, Boogaerts M, et al. Bone marrow cell transfer in acute myocardial infarction. Nat Clin Pract Cardiovasc Med 2006;3 Suppl 1:S69-72.

69. Lunde K, Solheim S, Aakhus S, et al. Intracoronary injection of mononuclear bone marrow cells in acute myocardial infarction. N Engl J Med 2006;355(12):1199-1209.

70. Schachinger V, Erbs S, Elsasser A, et al. Intracoronary bone marrow-derived progenitor cells in acute myocardial infarction. N Engl J Med 2006;355(12):1210-1221.

71. Yu CM, Bax JJ, Gorcsan J, 3rd. Critical appraisal of methods to assess mechanical dyssynchrony. Curr Opin Cardiol 2009;24(1):18-28.

72. Picano E, Pelosi G, Marzilli M, et al. In vivo quantitative ultrasonic evaluation of myocardial fibrosis in humans. Circulation 1990;81(1):58-64.

73. Maron BJ, Maron MS, Wigle ED, et al. The 50-year history, controversy, and clinical implications of left ventricular outflow tract obstruction in hypertrophic cardiomyopathy from idiopathic hypertrophic subaortic stenosis to hypertrophic cardiomyopathy: from idiopathic hypertrophic subaortic stenosis to hypertrophic cardiomyopathy. J Am Coll Cardiol 2009;54(3):191-200.

74. Baumgartner H, Hung J, Bermejo J, et al. Echocardiographic assessment of valve stenosis: EAE/ASE recommendations for clinical practice. Eur J Echocardiogr 2009;10(1):1-25.

75. Marwick TH. Echocardiography in the era of multimodality imaging. Heart Lung Circ;19(3):175-184.

76. Pietras RJ, Wolfkiel CJ, Veselik K, et al. Validation of ultrafast computed tomographic left ventricular volume measurement. Invest Radiol 1991;26(1):28-34.

77. Feiring AJ, Rumberger JA, Reiter SJ, et al. Sectional and segmental variability of left ventricular function: experimental and clinical studies using ultrafast computed tomography. J Am Coll Cardiol 1988;12(2):415-425.

78. Mochizuki T, Murase K, Higashino H, et al. Two- and three-dimensional CT ventriculography: a new application of helical CT. AJR Am J Roentgenol 2000;174(1):203-208.

79. Cleverley JR, Barrie JR, Raymond GS, et al. Direct findings of aortic injury on contrast-enhanced CT in surgically proven traumatic aortic injury: a multi-centre review. Clin Radiol 2002;57(4):281-286.

80. Mosely DS, Knight DA, Kacprowicz R, et al. Computed tomography scan versus ventilation-perfusion lung scan in the detection of pulmonary embolism. J Emerg Med 2002;23(2):205-206; author reply 206.

81. Becker CR, Jakobs TF, Aydemir S, et al. Helical and single-slice conventional CT versus electron beam CT for the quantification of coronary artery calcification. AJR Am J Roentgenol 2000;174(2):543-547.

82. Carr JJ, Crouse JR, 3rd, Goff DC, Jr., et al. Evaluation of subsecond gated helical CT for quantification of coronary artery calcium and comparison with electron beam CT. AJR Am J Roentgenol 2000;174(4):915-921.

83. Westerman BR. Advances in cardiovascular CT imaging: CT technology. Int J Cardiovasc Imaging 2005;21(1):5-11.

84. Candell-Riera J, Romero-Farina G, Aguade-Bruix S, et al. Ischemic cardiomyopathy: a clinical nuclear cardiology perspective. Rev Esp Cardiol 2009;62(8):903-917.

85. Carrea JR, Gleason G, Shaw J, et al. The Direct Diagnosis of Myocardial Infarction by Photoscanning after Administration of Cesium-131. Am Heart J 1964;68:627-636.

86. Vesely MR, Dilsizian V. Nuclear cardiac stress testing in the era of molecular medicine. J Nucl Med 2008;49(3):399-413.

87. Petretta M, Cuocolo A, Nicolai E, et al. Combined assessment of left ventricular function and rest-redistribution regional myocardial thallium-201 activity for

prognostic evaluation of patients with chronic coronary artery disease and left ventricular dysfunction. J Nucl Cardiol 1998;5(4):378-386.

88. Berman DS, Kiat H, Van Train KF, et al. Comparison of SPECT using technetium-99m agents and thallium-201 and PET for the assessment of myocardial perfusion and viability. Am J Cardiol 1990;66(13):72E-79E.

89. Eisenberg JD, Sobel BE, Geltman EM. Differentiation of ischemic from nonischemic cardiomyopathy with positron emission tomography. Am J Cardiol 1987;59(15):1410-1414.

90. Baer FM, Voth E, LaRosee K, et al. Comparison of dobutamine transesophageal echocardiography and dobutamine magnetic resonance imaging for detection of residual myocardial viability. Am J Cardiol 1996;78(4):415-419.

91. Baer FM, Theissen P, Schneider CA, et al. Dobutamine magnetic resonance imaging predicts contractile recovery of chronically dysfunctional myocardium after successful revascularization. J Am Coll Cardiol 1998;31(5):1040-1048.

92. Nagel E, Lehmkuhl HB, Bocksch W, et al. Noninvasive diagnosis of ischemia-induced wall motion abnormalities with the use of high-dose dobutamine stress MRI: comparison with dobutamine stress echocardiography. Circulation 1999;99(6):763-770.

93. Walsh EG, Doyle M, Lawson MA, et al. Multislice first-pass myocardial perfusion imaging on a conventional clinical scanner. Magn Reson Med 1995;34(1):39-47.

94. Bertschinger KM, Nanz D, Buechi M, et al. Magnetic resonance myocardial first-pass perfusion imaging: parameter optimization for signal response and cardiac coverage. J Magn Reson Imaging 2001;14(5):556-562.

95. Kim RJ, Fieno DS, Parrish TB, et al. Relationship of MRI delayed contrast enhancement to irreversible injury, infarct age, and contractile function. Circulation 1999;100(19):1992-2002.

96. Klein C, Nekolla SG, Bengel FM, et al. Assessment of myocardial viability with contrast-enhanced magnetic resonance imaging: comparison with positron emission tomography. Circulation 2002;105(2):162-167.

97. Merbach AE, Tóth É. The chemistry of contrast agents in medical magnetic resonance imaging. Chichester ; New York: Wiley; 2001. xii, 471 p243-279.

98. Corot C, Robert P, Idée JM, et al. Recent advances in iron oxide nanocrystal technology for medical imaging. Adv Drug Deliv Rev 2006;58(14):1471-1504.

99. Bonnemain B. Superparamagnetic agents in magnetic resonance imaging: physicochemical characteristics and clinical applications. A review. J Drug Target 1998;6(3):167-174.

100. Simonsen CZ, Ostergaard L, Vestergaard-Poulsen P, et al. CBF and CBV measurements by USPIO bolus tracking: reproducibility and comparison with Gd-based values. J Magn Reson Imaging 1999;9(2):342-347.

101. Wang YX, Hussain SM, Krestin GP. Superparamagnetic iron oxide contrast agents: physicochemical characteristics and applications in MR imaging. Eur Radiol 2001;11(11):2319-2331.

102. Thorek DL, Chen AK, Czupryna J, et al. Superparamagnetic iron oxide nanoparticle probes for molecular imaging. Ann Biomed Eng 2006;34(1):23-38.

103. Shapiro EM, Skrtic S, Koretsky AP. Sizing it up: cellular MRI using micron-sized iron oxide particles. Magn Reson Med 2005;53(2):329-338.

104. Williams JB, Ye Q, Hitchens TK, et al. MRI detection of macrophages labeled using micrometer-sized iron oxide particles. J Magn Reson Imaging 2007;25(6):1120-1128.

105. Stillman AE, Wilke N, Jerosch-Herold M. Use of an intravascular T1 contrast agent to improve MR cine myocardial-blood pool definition in man. J Magn Reson Imaging 1997;7(4):765-767.

106. Stillman AE, Wilke N, Li D, et al. Ultrasmall superparamagnetic iron oxide to enhance MRA of the renal and coronary arteries: studies in human patients. J Comput Assist Tomogr 1996;20(1):51-55.

107. Rohl L, Ostergaard L, Simonsen CZ, et al. NC100150-enhanced 3D-SPGR MR angiography of the common carotid artery in a pig vascular stenosis model. Quantification of stenosis and dose optimization. Acta Radiol 1999;40(3):282-290.

108. Forsting M, Reith W, Dorfler A, et al. MRI in acute cerebral ischaemia: perfusion imaging with superparamagnetic iron oxide in a rat model. Neuroradiology 1994;36(1):23-26.

109. Rozenman Y, Zou XM, Kantor HL. Magnetic resonance imaging with superparamagnetic iron oxide particles for the detection of myocardial reperfusion. Magn Reson Imaging 1991;9(6):933-939.

110. Trillaud H, Degreze P, Combe C, et al. USPIO-enhanced MR imaging of glycerol-induced acute renal failure in the rabbit. Magn Reson Imaging 1995;13(2):233-240.

111. Dennie J, Mandeville JB, Boxerman JL, et al. NMR imaging of changes in vascular morphology due to tumor angiogenesis. Magn Reson Med 1998;40(6):793-799.

112. Ros PR, Freeny PC, Harms SE, et al. Hepatic MR imaging with ferumoxides: a multicenter clinical trial of the safety and efficacy in the detection of focal hepatic lesions. Radiology 1995;196(2):481-488.

113. Bremer C, Allkemper T, Baermig J, et al. RES-specific imaging of the liver and spleen with iron oxide particles designed for blood pool MR-angiography. J Magn Reson Imaging 1999;10(3):461-467.

114. Seneterre E, Weissleder R, Jaramillo D, et al. Bone marrow: ultrasmall superparamagnetic iron oxide for MR imaging. Radiology 1991;179(2):529-533.

115. Anzai Y, Brunberg JA, Lufkin RB. Imaging of nodal metastases in the head and neck. J Magn Reson Imaging 1997;7(5):774-783.

116. Henning EC, Ruetzler CA, Gaudinski MR, et al. Feridex preloading permits tracking of CNS-resident macrophages after transient middle cerebral artery occlusion. J Cereb Blood Flow Metab 2009;29(7):1229-1239.

117. Sosnovik DE, Nahrendorf M, Deliolanis N, et al. Fluorescence tomography and magnetic resonance imaging of myocardial macrophage infiltration in infarcted myocardium in vivo. Circulation 2007;115(11):1384-1391.

118. Arbab AS, Janic B, Knight RA, et al. Detection of migration of locally implanted AC133+ stem cells by cellular magnetic resonance imaging with histological findings. FASEB J 2008;22(9):3234-3246.

119. Kraitchman DL, Bulte JW. Imaging of stem cells using MRI. Basic Res Cardiol 2008;103(2):105-113.

120. Weissleder R, Lee AS, Fischman AJ, et al. Polyclonal human immunoglobulin G labeled with polymeric iron oxide: antibody MR imaging. Radiology 1991;181(1):245-249.

121. Zhang C, Jugold M, Woenne EC, et al. Specific targeting of tumor angiogenesis by RGD-conjugated ultrasmall superparamagnetic iron oxide particles using a clinical 1.5-T magnetic resonance scanner. Cancer Res 2007;67(4):1555-1562.

122. Suzuki M, Honda H, Kobayashi T, et al. Development of a target-directed magnetic resonance contrast agent using monoclonal antibody-conjugated magnetic particles. Noshuyo Byori 1996;13(2):127-132.

CHAPTER 2
MONITORING INFLAMMATORY CELL INFILTRATION — A PRELIMINARY STUDY

2.1 INTRODUCTION

The potential of MRI as a noninvasive tool to detect contrast agent-labeled cells has been investigated recently, with the advent of novel contrast agents and cell labeling techniques[1,2]. As a negative enhancement contrast agent, iron oxide particles cause signal attenuation in T_2- and T_2^*-weighted images which makes them useful in a variety of animal models for cellular imaging[3]. Sized from large to small, SPIO are categorized as MPIO, SSPIO, USPIO and MION, respectively[4]. The majority of iron oxide particles accumulate in the liver, spleen, bone marrow and lymphatic node tissue after injection[3,5,6]. The physicochemical characteristics of iron oxide particles determine their MRI efficacy, blood pool kinetics, biodistribution, and metabolism within the imaged subjects[7,8]. Iron oxide contrast has been used to detect hepatic tumors[9,10] and lymph node metastases[11,12], and also for tracking stem cells[13] and monitoring various diseases associated with high macrophage activity[14,15]. Recently, MPIO were shown to significantly improve cellular imaging when single cells loaded with single MPIO were detected via MRI[16]. In contrast, accumulation of a considerable number of USPIO in one cell was required to achieve sufficient image contrast. Furthermore, the dilution effect caused by cell division more readily leads to loss of cell tracking in USPIO cell labeling than in MPIO cell labeling.

Inflammatory cells, in particular macrophages, are capable of taking up iron oxide particles[17]. Consequently, the labeled inflammatory cells can be detected using T_2^*-

weighted MRI during the inflammation process. In this manner, the iron oxide particles have been used to detect ischemia-associated inflammation[18,19], macrophage-rich atherosclerosis[20,21], and acute cardiac graft rejection[22]. Several pathways have been proposed for transporting iron oxide particles to macrophages[3]. For example, iron oxide particles could be endocytosed by activated blood monocytes migrating into affected tissue or they could be transcytosed across the endothelium via progressive endocytosis by *in situ* macrophages. Both mechanisms may take place simultaneously when iron oxide particles are transported into the affected tissue via the inflammatory neovasculature.

Recently, iron oxide particles have been used to label inflammatory cells engaged in MI-induced cardiac tissue inflammation. Furthermore, Sosnovik and colleagues[23] demonstrated that inflammatory cells could be labeled by intravenous injection of iron oxide particles *after* the MI. In this manner, both circulating and resident inflammatory cells will engulf iron oxide particles and contribute to the signal attenuation around the MI site. Although inflammatory cells such as macrophages could also be labeled *in vitro* and then transplanted into the infarcted heart[24], the transplantation delivery is usually limited by a low engraftment. Therefore, this study demonstrates a new cell labeling method for studying the inflammation process during cardiac remodeling in which the inflammatory cells are pre-labeled *prior to* the MI via intravenous injection of iron oxide particles.

One purpose of this study is to investigate the temporal relationship between inflammatory cell infiltration and cardiac performance during MI-induced cardiac remodeling using MPIO-enhanced MRI. Following a MI, effective cardiac tissue repair

occurs when monocyte-derived macrophages and mast cells produce cytokines and growth factors necessary for fibroblast proliferation and neovascularization[25]. However, when augmented macrophage homing and cytokine production cause adverse left ventricular remodeling, the deterioration of cardiac function typically leads to heart failure[26]. Therefore, an advanced MRI cell tracking technique demonstrating a prospective for studying the *in vivo* behavior of inflammatory cells would help to better understand MI-induced inflammation.

2.2 METHODS

2.2.1 Animal Preparation

Adult male C57Bl/6 mice (n=27; 23.8±1.4 g; 6–11 weeks old) were used in compliance with the Institutional Animal Care and Use Committee at the Medical College of Georgia, Augusta, GA, USA. The animals were anesthetized with a mixture of medical air, oxygen (1:1), and 2.0% isoflurane (Abbott Laboratories, Abbott Park, IL, USA), then put in a prone position on the animal cradle. The isoflurane was maintained at 1.8±0.2% throughout all MRI sessions. This protocol maintained a constant respiration rate of 63±6 breaths per minute and heart rate of 437±58 beats per minute during each MRI session.

The animals were divided into three experimental groups: 1) myocardial infarction group with MPIO injection (MI+MPIO, n=7); 2) myocardial infarction group without MPIO injection (MI-MPIO, n=6); and 3) sham-operated group with MPIO injection (Sham+MPIO, n=7). For the MI+MPIO and Sham+MPIO groups, the animals received intravenous administration of MPIO for pre-labeling inflammatory cells. At 7

days post-MPIO injection, the MI+MPIO group underwent a thoracotomy (open-chest) surgical procedure followed by permanent ligation of the left anterior descending coronary artery, which induced a MI. The Sham+MPIO group underwent only the thoracotomy surgery, which did not cause any type of myocardial injury. This study investigated MPIO-labeled inflammatory cells migrating to the MI site. Therefore, none of the surgeries were performed until the free MPIO were cleared from the blood pool for both MPIO injection groups. The 7-day interval between the MPIO injection and surgical procedure allowed the particles to be cleared from the blood pool under the detectable level, which minimized potential signal attenuation contributed by circulating particles otherwise remaining in the blood pool. This protocol also reduced the possibility of activated resident inflammatory cells endocytosing the MPIO directly from the blood pool following the MI.

2.2.2 Contrast Agent

The iron oxide contrast agent used in this study was Bangs particles (a type of MPIO, Catalog code: ME03F; Bangs Laboratories, Inc., Fishers, IN, USA). The Bangs particles have a mean diameter of 1.63 μm, with a magnetite core (42.5% weight) coated with a polymer (P(S/V-COOH)Mag/Encapsulated). These particles are also tagged with a fluorescent dye (Suncoast Yellow fluorescence, excitation:emission = 540:600 nm). The undiluted MPIO solution (original concentration of 2.793×10^9 particles per ml) was injected via tail vein at a dose of 14.5 μg Fe/g body weight (i.e., 1.31×10^7 particles/g body weight).

2.2.3 Blood Sample Measurement

MPIO blood kinetics in the murine model was examined to determine the proper timing for surgically inducing an experimental MI without residual effects of the negative MRI enhancement from the circulating iron particles. The kinetics study was performed on 7 non-injured animals (25.3±3.4 g; 6-12 weeks old). Blood samples were obtained at various times up to 8 minutes post-MPIO injection with MPIO fluorescence intensity measured on a 2-D IVIS 100 Imaging System (Caliper Life Sciences, Hopkinton, MA, USA). One or two blood samples were taken from each mouse anesthetized with 1.0% isoflurane. Briefly, a 27-gauge needle, 1-ml syringe and 0.5-ml tube were used and moistened with heparin. Then approximately 100 µl of blood was removed by puncturing the needle into the left ventricle of the heart. A 50-µl blood sample was then placed into the 96-well plate for fluorescence imaging.

2.2.4 MI

Animals were anesthetized with an intraperitoneal injection of ketamine/xylazine and placed in a supine position. A midline cervical incision was made for tracheal intubation. The intubated mice were then connected to a rodent ventilator (CWE Inc., Ardmore, PA, USA) and ventilated at a respiratory rate of 90 breaths per minute. A mid-line thoracotomy was done to open the chest at the upper sternum between the fourth and fifth ribs. A MI was produced by permanently ligating the left anterior descending coronary artery at a position approximately 1 mm below the left auricle with an 8-0 polypropylene monofilament suture. This coronary artery ligation caused a visual area of infarction in the left ventricle, seen as the tissue turning a pale color below the ligation site. The sham group underwent only the thoracotomy to open the chest; ligation of the

left anterior descending artery was not performed on these animals. After surgery, the mice were allowed to recover in a recovery chamber at 38 ºC under careful supervision, then returned to their cages to rest until time for each imaging session.

2.2.5 MRI

MRI was performed one day before surgery as a baseline, and then repeated at 3, 7 and 14 days after surgery. Images were acquired on a horizontal 7.0-T, 21-cm MRI spectrometer (Bruker Instruments, Billerica, MA, USA) equipped with a micro-imaging gradient insert (950 mT/m). A 35mm inner diameter volume coil was used to transmit and receive at ^{1}H frequency (300 MHz). The ECG and respiratory signals were monitored and used for gating by a physiological monitoring system (SA Instruments, INC., Stony Brook, NY). Short-axis images were acquired through the left ventricle and perpendicular to the long axis of the heart using two pulse sequences: (1) a Gradient Echo sequence with Flow Compensation (GEFC) to acquire the T_2^*-weighted images on which signal intensity and contrast-to-noise ratio (CNR) were calculated; and (2) a GEFC cine sequence to acquire the movie of cardiac movement, on which cardiac function was evaluated. The parameters for the GEFC were: echo time/repetition time (TE/TR) = 4/120 ms; flip angle (FA) = 30^{o}; field of view (FOV) = 30 x 30 mm; slice thickness = 1 mm; matrix = 256 x 256 and 8 averages. The parameters for GEFC cine sequence were: TE/TR = 4/16 ms; FA = 25^{o}; FOV = 30 x 30 mm; slice thickness = 1 mm; matrix size = 128 x 128; 8 frames in one cardiac cycle and 8 averages. Both pulse sequences were gated using the R-wave of the ECG signal.

To evaluate the cardiac performance, the left ventricular ejection fraction (LVEF) was calculated using left ventricular end-diastolic volume (LVEDV) and left ventricular

end-systolic volume (LVESV) [LVEF (%) = (LVEDV-LVESV)/LVEDV]. The LVEDV and LVESV were determined from the endocardial contours at the end-diastole and end-systole phase, respectively. The regions of interest (ROI) for calculation were drawn on the continuous short-axis MRI slices from the apex to the base covering the entire heart.

CNR at the MI site was calculated on GEFC images [$CNR = (SI_{MI} - SI_{norm})/SI_{bkg}$]. SI_{MI} represents the signal intensity at the MI region which was determined as the area with wall thinning and further confirmed by the akinetic contractility in the cine images, SI_{norm} represents the signal intensity at the normal myocardium, and SI_{bkg} represents the background noise.

2.2.6 Fluorescent Imaging and Histology

After the MRI session, the heart was removed from the animal and immediately fluorescently imaged on the same two-dimensional IVIS 100 Imaging System used for the blood sample measurements (n = 4 for MI+MPIO, n = 3 for Sham+MPIO, and n = 2 for MI-MPIO). Briefly, the heart was put on the stage inside the imaging chamber with the infarction site facing up. The parameters used to obtain the primary image were: excitation:emission = 500-550:575-650 nm; exposure time = 1 sec; binning = 2; f/stop = 2; FOV = 5 cm and subject height = 1.5 cm. The parameters for background image were: excitation:emission = 460-490:575-650nm; exposure time = 1 sec; binning = 2; f/stop = 2; FOV = 5 cm and subject height = 1.5 cm. The corrected image was obtained by subtracting the background image from the primary image. One mouse from each group was sacrificed for histology after the MRI session at 7 and 14 days post-surgery, respectively. Briefly, the animals were perfused first with saline and then with 4% paraformaldehyde. The heart was excised, fixed in paraformaldehyde, and then cut into

7-μm-thick sections. F4/80 staining was performed to stain macrophages and Prussian blue staining to confirm the MPIO existence.

2.2.7 Statistical Analysis

All data was presented as mean ± standard error of mean (SEM). A two-way repeated-measures analysis of variance (ANOVA) was used to compare the difference in CNR and LVEF among the three experimental groups. Bonferroni post-hoc test was used to compare any two assigned groups. A linear regression was used to determine if a correlation existed between the CNR and LVEF for MI+MPIO group. The first-order exponential fit was used to estimate the half-life of MPIO washout in the blood pool. The GraphPad Prism 5.01 (GraphPad Software Inc., San Diego, CA, USA) was used for all statistical analyses. Significance was determined at $P < 0.05$.

2.3 RESULTS

2.3.1 MPIO Blood Kinetics

Blood kinetics study (Figure 2.1) showed that the fluorescence intensity of blood samples reached a maximum within 30 seconds post-MPIO injection. The MPIO was quickly washed out from the blood pool with a half-life of less than 1 minute ($T_{1/2} = 0.73$ minute; $r^2 = 0.94$). Therefore, the 7-day interval between MPIO injection and MI was sufficient for particles to be cleared from the blood pool, thus minimizing the signal attenuation caused by the MPIO otherwise remaining in the peripheral blood. In this manner, inflammatory cells mobilizing to the MI site by remote recruitment were distinguished from the resident inflammation-activated immune cells. More information

about MPIO blood kinetics during the myocardial infarction process can be found in Appendix A.

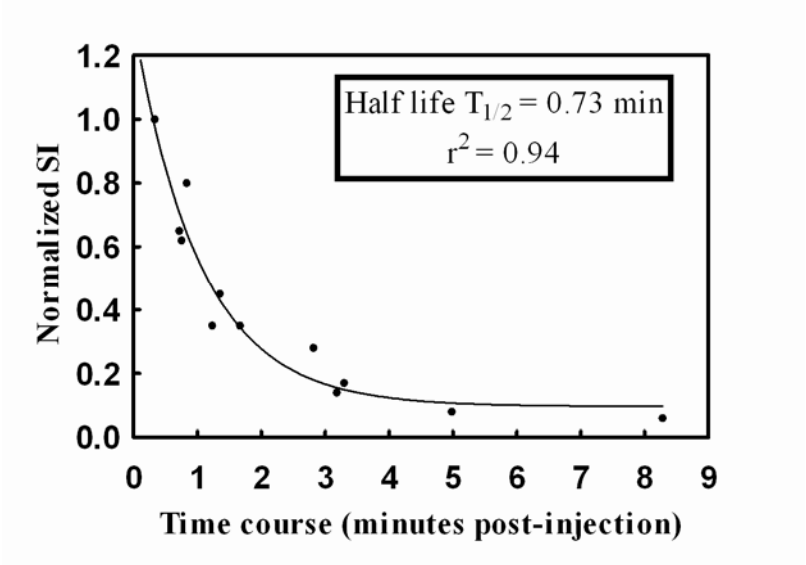

Figure 2.1 MPIO blood kinetics. Each animal (n = 7) had blood removed at various time points up to 8 minutes post-MPIO injection. Fluorescence signal intensity of 50-µl blood was measured and fitted to an exponential curve. SI: signal intensity.

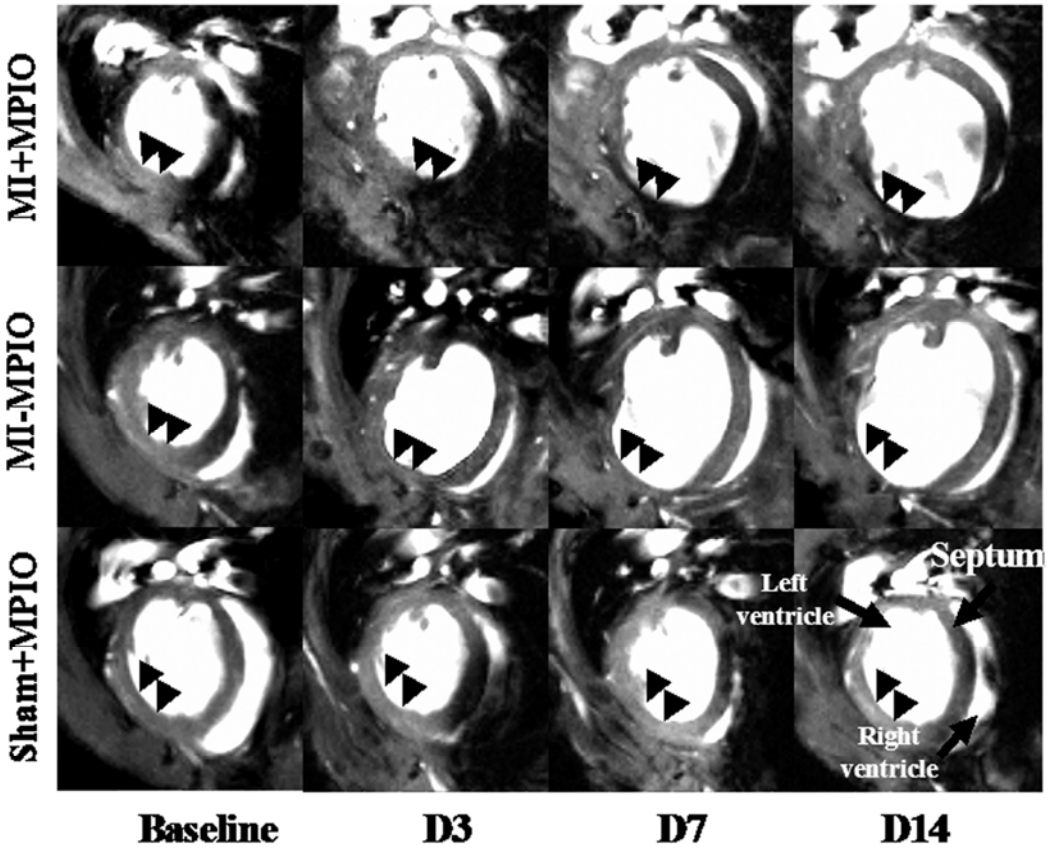

Figure 2.2 Longitudinal MR images. MRIs were performed at baseline, 3 days (D3), 7 days (D7) and 14 days (D14) post-surgery. Temporal signal attenuation was observed at the MI site in MI+MPIO group. The short arrows point to the myocardial infarction or corresponding sites, and the long arrows in the bottom right image show the cardiac geometry.

2.3.2 MPIO-Labeled Inflammatory Cell Infiltration

Pre-labeled inflammatory cell infiltration into the MI site was monitored and examined in T_2^*-weighted MRI. As illustrated in Figure 2.2, gradual signal attenuation at the MI site was observed in the MI+MPIO group. No detectable signal attenuation was observed at the corresponding site in either MI-MPIO or Sham+MPIO group. The MRI findings were correlated with histology and fluorescent imaging. In Figure 2.3, Views A and B are microscopic pictures of transverse heart slices from a representative MI+MPIO heart and Sham+MPIO heart, respectively. Each picture is a montage of approximately thirty 10x-magnified microscopic images. A large number of MPIO-labeled cells were localized around the MI and adjacent area (Figure 2.3A), while no MPIO-labeled cell was observed in the sham heart (Figure 2.3B). Furthermore, the *ex vivo* fluorescent images for the MI+MPIO group showed a strong signal enhancement at the MI site and also the adjacent area, indicative of localized MPIO (Figure 2.3E). The Sham+MPIO heart lacked fluorescence enhancement (Figure 2.3H). The cross-correlation between MRI, histology staining and fluorescent imaging confirmed that the pronounced signal attenuation around the MI site was caused by infiltration of MPIO-labeled cells.

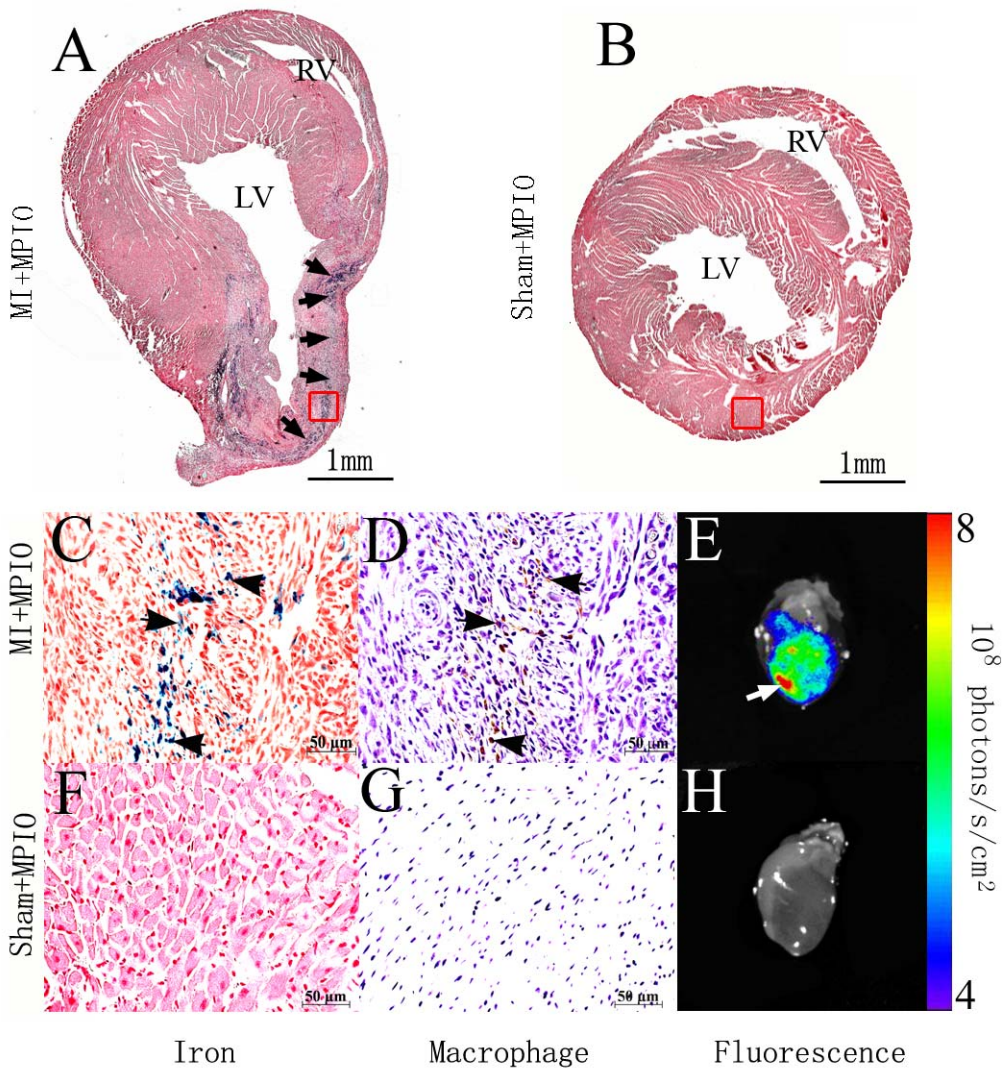

Figure 2.3 Histology. The images show the transverse heart slices from MI+MPIO and Sham+MPIO group, respectively. The MI and sham hearts were excised 7 days post-surgery. A and B: whole heart slices montaged with approximately 30 microscopic images (10x magnification). Arrows in A indicate the iron accumulation in the myocardial infarction site. Also observed are iron clusters in the extended area adjacent to the MI site. LV: left ventricle; RV: right ventricle. C and D: correspond to the enlargement area boxed with red lines in A. Arrows in C point to some iron-laden cells; arrows in D point to the macrophages. F and G: correspond to enlargement area boxed with red lines in B. C and F: Prussian blue staining for iron. D and G: F4/80 staining for macrophages. E and H: fluorescent images of the representative hearts. In panel E, also observed are enhanced signal intensities beyond the MI site, suggesting extended MPIO accumulation. However, some of them might be caused by tissue auto-fluorescence.

The histology for the MI+MPIO group further showed the co-localization of Prussian blue and F4/80 staining, indicating that an appreciable amount of MPIO were incorporated in macrophages (Figures 2.3C and 2.3D). No F4/80 positive or Prussian blue stained cell was observed in the Sham+MPIO heart. These results suggested that a large number of MPIO-labeled macrophages mobilized, infiltrated, and engrafted into the infarcted area of the heart, thereby causing distinguishable signal attenuation in the T_2*-weighted MRI.

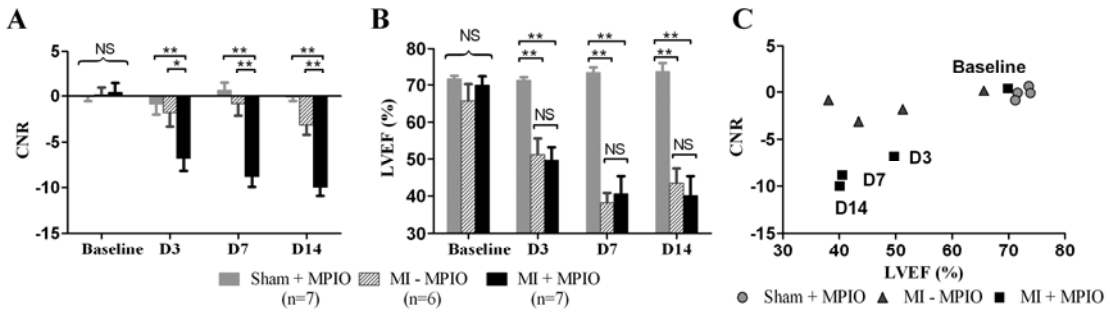

Figure 2.4 CNR and LVEF measurements. A. Temporal signal attenuation at the MI site. B. Temporal changes of LVEF. (*) P < 0.01, (**) P< 0.001, NS: not significant. C. Correlating of CNR and LVEF. Plots for different groups are labeled with different legends. As expected, data points of the sham group form a cluster close to the baseline points, suggesting no attenuation for both CNR and LVEF. Data points of the MI-MPIO group show attenuation in LEVF but only minimally in CNR. For the MI+MPIO group, CNR and LVEF were synchronously attenuated. Further analysis using linear regression shows a positive linear correlation between CNR and LVEF (r^2=0.98). D3, D7 and D14: 3, 7 and 14 days post-MI, respectively.

CNR at the MI site was calculated to quantify the infiltration of MPIO-labeled inflammatory cells into the MI site. The negative CNR values indicated hypointensities around the MI site (Figure 2.4A). The more negative the CNR was, the more attenuated the signal at the MI site relative to the normal myocardium. The continuous CNR attenuation in MI+MPIO group suggested ever-increasing MPIO-labeled inflammatory cell infiltration. The CNR decreased dramatically within one week post-MI and changed only minimally between 7 days and 14 days post-MI. The CNR at the corresponding sites for the two control groups did not show large variation over the experiment course. A two-way repeated-measures ANOVA showed a significant difference in CNR values between the three treatment groups ($P < 0.0001$). Bonferroni post-hoc testing further showed that the CNR in MI+MPIO group was significantly different from the other two groups at all time points after surgery ($P < 0.01$). No significant difference in CNR values at baseline was observed among the three groups. The CNR represents the difference of signal intensity between the MI site and normal myocardium. Therefore, these results suggest that not only a global infiltration of MPIO-labeled cells occurred at the MI site, but also possibly a redistribution of MPIO-labeled cells between the MI site and normal myocardium. The concept of redistribution was excluded, however, because relatively stable signal intensity was observed in the normal myocardium over the course of each experiment. Thus, this CNR data suggests a global MPIO-labeled inflammatory cell migration and infiltration into the MI site.

2.3.3 Temporal Features of Cardiac Performance

Figure 2.3A illustrates the anatomical morphological changes occurring 7 days after the MI. LVEF, a standard clinical measurement, was used to evaluate the resulting alterations in post-MI cardiac performance. Ventricular hypertrophy quickly develops following a MI in the murine model. LVEF in the MI group decreased dramatically within one week post-MI, then somewhat stabilized; the LVEF in the sham group did not alter much over the course of the experiment (Figure 2.4B). A two-way repeated-measures ANOVA showed a significant difference in LVEF between the 3 treatment groups ($P < 0.0001$). As expected, the Bonferroni post-hoc test further showed the LVEF in the sham group was significantly different from that of the other two groups at all time points after surgery ($P < 0.001$). No significant difference between the three treatment groups was observed at baseline.

2.3.4 Correlation of Inflammatory Cell Infiltration and Cardiac Function

A linear regression was used to examine the temporal relationship between MPIO-labeled cell infiltration and cardiac function by testing the extent to which CNR at the MI site was correlated with LVEF. CNR and LVEF demonstrated similar time-dependence characteristics for the MI+MPIO group over the 14-day course; both measures rapidly attenuated within one week post-MI before they eventually stabilized (Figures 4A and 4B). A positive linear correlation ($r^2 = 0.98$, slope = 0.332) was obtained between CNR and LVEF (Figure 2.4C). This finding suggests that the post-MI inflammatory cell infiltration was associated with progression of left ventricular remodeling.

2.4 DISCUSSION

This study investigated the temporal characteristics of MI-induced inflammation by noninvasively monitoring the infiltration of MPIO-labeled inflammatory cells. In contrast to previous studies[23], iron oxide particles were injected *prior* to inducing the MI rather than *afterward*. Using this protocol, the pre-labeled immune cells were distinguishable from the activated resident immune cells since only the pre-labeled cells mobilizing to the MI site were detected. Surgically inducing the MI after the MPIO were cleared from the peripheral blood pool did not allow the local immune cells (activated as part of the initial inflammatory response) to phagocytize the circulating MPIO otherwise remaining in the blood pool. Furthermore, the entire progress of labeled cell mobilization and infiltration could be temporally tracked during the post-MI remodeling process.

The pre-labeling technique described in this study represents a more effective method for studying inflammatory cell behavior compared to injecting *in vitro* labeled-cells directly into the infarcted heart. Similarly, Ye and colleagues[27] recently demonstrated the pre-labeling approach when they tracked recipient macrophages in a rat chronic cardiac allograft rejection model. Recent investigations found that the *in vitro* labeling process may affect the functionality of labeled cells and may also cause cell loss during and/or after cell injection, leading to a low cell engraftment[28]. Furthermore, intra-myocardial injection could further injure the myocardium causing irreversible damage. Pre-labeling may potentially promote a variety of cell types, rather than one specific cell type, to take up the iron oxide particles. Therefore, a limitation of the current study was the unavoidable non-specific cell labeling. T cells, B cells and macrophages are all capable of incorporating MPIO while keeping their migrating and engrafting capabilities.

Nevertheless, the iron oxide-enhanced MRI has been demonstrated as an effective method for macrophage detection, since the highest MPIO incorporation was observed in the culture of macrophages[17].

The half life of iron oxide particles in the blood is dose-dependent and related to a progressive saturation of macrophage uptake by various organs[3]. Hence, the half life of MPIO in the blood pool was first measured in this study at the given dose level (14.5 μg Fe/g body weight) to determine when the circulating MPIO ceased to provide significant contrast enhancement. The short half life (< 1 minute) obtained in this study suggested the 7-day interval between MPIO injection and surgery was sufficient for the MPIO clearance from blood. Iron oxide particles are predominantly cleared by the RES[29] after which they accumulate in macrophage-rich organs such as the liver, spleen, bone marrow and lymph node[6,8]. Due to the saturation of macrophage uptake by such organs, a large amount of iron oxide particles was expected to remain much longer than the blood half-life. The 7-day interval should be long enough to ensure an appreciable liver signal recovery and to prevent temporal MPIO saturation in such organs. An assumption was made that the RES would not readily release MPIO-labeled immune cells until the surgically-induced MI triggered the inflammatory response. Nonetheless, quantifying the MPIO-labeled cells in the blood sample at baseline and various times after the MI would be useful to further consolidate the current findings with those of future studies. Some information about the quantification of MPIO-labeled cells in blood can be found in appendix A.

The MRI results demonstrated dramatic changes in both cardiac performance and inflammatory cell infiltration within one week post-MI. These physiological alterations

suggest that an early intervention, within one week post-MI, may be fundamental to reducing adverse inflammatory responses in the murine model. This study also found that the attenuated signal intensity at the MI site was relatively steady after one week post-MI. This stabilized signal attenuation may indicate that MPIO-labeled inflammatory cells remained in the MI site for an appreciable time period. Thus, future studies should be conducted over a longer time span that would potentially capture MPIO washout in the post-MI remodeling process. A positive correlation was obtained when correlating CNR with LVEF, which implied that the inflammatory cell infiltration was linearly associated with reduced cardiac function. However, this finding also warrants further investigation since the mechanism and role of inflammation during the MI process was beyond the scope of this study.

Novel methods are warranted to more accurately quantify labeled-cell infiltration in MRI, rather than using CNR as the representative index. CNR may exhibit intrinsic variation due to fluctuation of the running MR system. CNR values are calculated via the mean values of signal intensity of selected ROI. This ROI measurement generally represents the mean density of accumulated iron oxide particles rather than detailed distribution of labeled cells. Therefore, T_2-mapping might be a better way to quantify iron oxide-labeled cells. Furthermore, fundamental drawbacks exist for T_2^*-weighted MRI. The hypointensities may be caused by tissue-interface inhomogeneity, hemorrhage and cell necrosis, resulting in misinterpretation of the MRI results. For example, signal attenuation was occasionally observed in the left ventricular posterior wall and interventricular septum. These artifacts could be caused by cardiac motion, tissue-air interference, and/or disturbance by the MPIO deposited in the liver. In addition to

developing better cell quantification methods, the MPIO dose also warrants further optimization. An excessive dose may lead to MPIO saturation around the MI site, while an insufficient dose may result in loss of cell tracking. In this initial study, a relatively high dose was injected to see if the signal attenuation was feasible for tracking post-MI macrophage infiltration. Dose optimization was performed in the subsequent studies.

2.5 CONCLUSIONS

This study demonstrated that inflammatory cell mobilization and cardiac performance could be noninvasively and temporally monitored in the murine MI model using MPIO-enhanced MRI. Continuous signal attenuation around the MI site quantified with CNR suggests ever-increasing MPIO-labeled inflammatory cell infiltration. Also, a positive linear correlation was obtained between MPIO-labeled cell infiltration and left ventricular function during post-MI remodeling. These results support the hypotheses that inflammatory cells pre-labeled with an MPIO contrast agent mobilized, infiltrated and engrafted to the MI site and could be monitored using T_2^*-weighted MRI. This MPIO-enhanced MRI technique has the potential of quantifying cell infiltration and therefore disease progress during pathological processes.

2.6 REFERENCES

1. Modo M, Hoehn M, Bulte JW. Cellular MR imaging. Mol Imaging 2005;4(3):143-164.

2. Liu W, Frank JA. Detection and quantification of magnetically labeled cells by cellular MRI. Eur J Radiol 2009;70(2):258-264.

3. Corot C, Robert P, Idee JM, et al. Recent advances in iron oxide nanocrystal technology for medical imaging. Adv Drug Deliv Rev 2006;58(14):1471-1504.

4. Benderbous S, Corot C, Jacobs P, et al. Superparamagnetic agents: physicochemical characteristics and preclinical imaging evaluation. Acad Radiol 1996;3 Suppl 2:S292-294.

5. Bourrinet P, Bengele HH, Bonnemain B, et al. Preclinical safety and pharmacokinetic profile of ferumoxtran-10, an ultrasmall superparamagnetic iron oxide magnetic resonance contrast agent. Invest Radiol 2006;41(3):313-324.

6. Weissleder R, Stark DD, Engelstad BL, et al. Superparamagnetic iron oxide: pharmacokinetics and toxicity. AJR Am J Roentgenol 1989;152(1):167-173.

7. Bonnemain B. Superparamagnetic agents in magnetic resonance imaging: physicochemical characteristics and clinical applications. A review. J Drug Target 1998;6(3):167-174.

8. Wang YX, Hussain SM, Krestin GP. Superparamagnetic iron oxide contrast agents: physicochemical characteristics and applications in MR imaging. Eur Radiol 2001;11(11):2319-2331.

9. Bellin MF, Zaim S, Auberton E, et al. Liver metastases: safety and efficacy of detection with superparamagnetic iron oxide in MR imaging. Radiology 1994;193(3):657-663.

10. Weishaupt D, Willmann JK, Lutz AM, et al. Resovist for imaging of hepatocellular carcinoma in the cirrhotic liver. Eur Radiol 2004;14 Suppl 1:C5-6.

11. Bellin MF, Beigelman C, Precetti-Morel S. Iron oxide-enhanced MR lymphography: initial experience. Eur J Radiol 2000;34(3):257-264.

12. Russell M, Anzai Y. Ultrasmall superparamagnetic iron oxide enhanced MR imaging for lymph node metastases. Radiography 2007;13((Supplement 1): e73-e84).

13. Bulte JW, Douglas T, Witwer B, et al. Magnetodendrimers allow endosomal magnetic labeling and in vivo tracking of stem cells. Nat Biotechnol 2001;19(12):1141-1147.

14. Kleinschnitz C, Bendszus M, Frank M, et al. In vivo monitoring of macrophage infiltration in experimental ischemic brain lesions by magnetic resonance imaging. J Cereb Blood Flow Metab 2003;23(11):1356-1361.

15. Corot C, Petry KG, Trivedi R, et al. Macrophage imaging in central nervous system and in carotid atherosclerotic plaque using ultrasmall superparamagnetic iron oxide in magnetic resonance imaging. Invest Radiol 2004;39(10):619-625.

16. Shapiro EM, Skrtic S, Sharer K, et al. MRI detection of single particles for cellular imaging. Proc Natl Acad Sci U S A 2004;101(30):10901-10906.

17. Williams JB, Ye Q, Hitchens TK, et al. MRI detection of macrophages labeled using micrometer-sized iron oxide particles. J Magn Reson Imaging 2007;25(6):1120-1128.

18. Rausch M, Sauter A, Fröhlich J, et al. Dynamic patterns of USPIO enhancement can be observed in macrophages after ischemic brain damage. Magn Reson Med 2001;46(5):1018-1022.

19. Dousset V, Delalande C, Ballarino L, et al. In vivo macrophage activity imaging in the central nervous system detected by magnetic resonance. Magn Reson Med 1999;41:329-333.

20. Durand E, Raynaud JS, Bruneval P, et al. Magnetic resonance imaging of ruptured plaques in the rabbit with ultrasmall superparamagnetic particles of iron oxide. J Vasc Res 2007;44(2):119-128.

21. Kooi ME, Cappendijk VC, Cleutjens KB, et al. Accumulation of ultrasmall superparamagnetic particles of iron oxide in human atherosclerotic plaques can be detected by in vivo magnetic resonance imaging. Circulation 2003;107(19):2453-2458.

22. Wu YL, Ye Q, Foley LM, et al. In situ labeling of immune cells with iron oxide particles: an approach to detect organ rejection by cellular MRI. Proc Natl Acad Sci U S A 2006;103(6):1852-1857.

23. Sosnovik DE, Nahrendorf M, Deliolanis N, et al. Fluorescence tomography and magnetic resonance imaging of myocardial macrophage infiltration in infarcted myocardium in vivo. Circulation 2007;115(11):1384-1391.

24. Leor J, Rozen L, Zuloff-Shani A, et al. Ex vivo activated human macrophages improve healing, remodeling, and function of the infarcted heart. Circulation 2006;114(1 Suppl):I94-100.

25. Frangogiannis NG, Smith CW, Entman ML. The inflammatory response in myocardial infarction. Cardiovasc Res 2002;53(1):31-47.

26. Timmers L, Sluijter JP, van Keulen JK, et al. Toll-like receptor 4 mediates maladaptive left ventricular remodeling and impairs cardiac function after myocardial infarction. Circ Res 2008;102(2):257-264.

27. Ye Q, Wu YL, Foley LM, et al. Longitudinal tracking of recipient macrophages in a rat chronic cardiac allograft rejection model with noninvasive magnetic resonance imaging using micrometer-sized paramagnetic iron oxide particles. Circulation 2008;118(2):149-156.

28. Pawelczyk E, Arbab AS, Chaudhry A, et al. In vitro model of bromodeoxyuridine or iron oxide nanoparticle uptake by activated macrophages from labeled stem cells: implications for cellular therapy. Stem Cells 2008;26(5):1366-1375.

29. Bierry G, Jehl F, Boehm N, et al. Macrophage activity in infected areas of an experimental vertebral osteomyelitis model: USPIO-enhanced MR imaging--feasibility study. Radiology 2008;248(1):114-123.

CHAPTER 3
MONITORING INFLAMMATORY CELL INFILTRATION — A DOSE-DEPENDENT STUDY

3.1 INTRODUCTION

Myocardial infarction is a leading cause of global deaths and disabilities. Inflammation plays a key role in the process of post-MI cardiac remodeling, during which inflammatory cells mobilize to the MI site attempting to take away necrotic cells and repair the damaged tissue[1,2]. As superparamagnetic contrast agents, iron oxide particles can reduce relaxation time T_2 and T_2^* and thus produce signal attenuation at the target of interest in MRI. Following intravenous administration, iron oxide particles are taken up by RES. Inflammatory cells such as monocytes or macrophages which have phagocytosed iron oxide particles can thus be detected by MRI. Studies have shown that the monocyte or macrophage uptake of iron oxide particles is greatly influenced by the particle size, larger particles leading to more efficient cell labeling[3,4]. Research further showed that MPIO provided a higher efficiency for labeling macrophages compared to SSPIO and USPIO[5]. The inflammation process that involves monocyte/macrophage traffic can be monitored in many diseases through iron oxide particles-enhanced MRI techniques[6-8]. Iron oxide particles have been used to study infiltration of inflammatory cells into the rejected heart[9] following transplantation and into the infarcted myocardium[10] in rodent models.

It is of fundamental importance to quantify the relative amount of labeled cells infiltrating into the injured area *in vivo* by cellular MRI, which will provide quantitative

information regarding cell population, disease progression or treatment effect. Many studies have focused on *in vitro* quantification of iron oxide particle-labeled cells[11,12]. These studies are useful for determining the MR property of a particular type of iron oxide particles such as their T_1 and T_2 relaxivites, and to provide insight for further *in vivo* study. However, there are essential differences between the *in vitro* and *in vivo* environment. The relaxation times T_1 and T_2 are dependent not only on the type of iron oxide particles and iron concentration, but on the particle distribution as well as the microenvironment surrounding the iron oxide particle, i.e., the cell compartmentalization, water content and ionic environment. The substantial differences between the *in vivo* and *in vitro* environments make it imperative to calibrate an *in vivo* relationship projecting the signal intensity or relaxivity to the number of labeled cells, before taking further steps to quantify disease progression or to evaluate treatment effect.

The previous study demonstrated that infiltration of inflammatory cells can be noninvasively and longitudinally monitored during the MI using MPIO at a dose level of 14.5 μg Fe/g body weight[13]. The main purpose of this dose-dependent study is to optimize the MPIO dose as well as the temporal window for inflammatory cell tracking. In addition, this study investigated the connection between the MR signal intensity at the MI site and the infiltration rate of labeled cells. In order to assess the cell infiltration, it is fundamentally important to correlate the MR signal intensity with the features of cell infiltration, such as the cell infiltration rate or even the density of labeled cells at the infarction site. The information acquired from this study can potentially be translated to other cell labeling studies, e.g. stem cell labeling and tracking, and provide useful clues for quantification of labeled cell infiltration in MI.

3.2 METHODS

3.2.1 Animal Preparation

Adult male C57Bl/6 mice (n = 57; 24.8±2.7 g; 6–12 weeks old) were used in compliance with the Institutional Animal Care and Use Committee at the Medical College of Georgia, Augusta, GA, USA. The procedures have been described in the previous chapter. Briefly, the animals were anesthetized with a mixture of medical air, oxygen, and isoflurane, and then put in a prone position on the animal cradle. The isoflurane was maintained at ~1.5% throughout all MRI sessions. During this dose-dependent study, the animals were maintained at a constant animal respiration rate of 65±7 breaths per minute and a heart rate of 441±52 beats per minute.

Animals were divided into 5 dose groups: 14.5, 9.1, 3.6, 1.1 μg Fe/g body weight and a control group without any MPIO injection. The MPIO were injected into the animal blood stream intravenously. At 7 days post-injection, the animals underwent surgery to induce MI. MR images were acquired at 1 day before MI surgery (baseline), 3 days (D3), 7 days (D7), 14 days (D14) and 21 days (D21) post-MI. The experiment time course is shown in Figure 3.1.

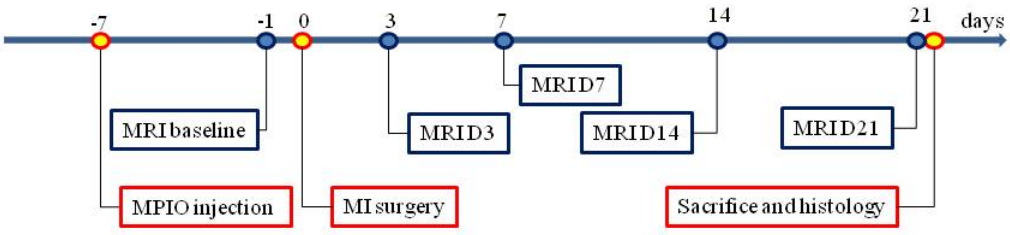

Figure 3.1 Time course for dose-dependent study.

3.2.2 Contrast Agent

The iron oxide contrast agent used in this study was Bangs particles (a type of MPIO, Catalog code: ME03F; Bangs Laboratories, Inc., Fishers, IN, USA). Bangs particles have been described in chapter 2. Briefly, these particles have a mean diameter of 1.63 μm, with a magnetite core (42.5% weight) coated with a polymer (P(S/V-COOH)Mag/Encapsulated). These particles are also tagged with a fluorescent dye (Suncoast Yellow fluorescence, excitation:emission = 540:600 nm). For animals receiving the highest dose, the undiluted MPIO solution (original concentration of 2.793×10^9 particles per mL) was injected via tail vein at a dose of 14.5 μg Fe/g body weight (i.e., 1.31×10^7 particles/g body weight). For the lower dose levels, the MPIO solution was diluted in proportion using saline solution while maintaining a relatively consistent total injection volume. For example, when the dose was 3.6 μg Fe/g body weight, the concentration was first diluted into $2.793 \times 10^9 \times (3.6/14.5) = 6.934 \times 10^8$ particles/g body weight and then a volume corresponding to the animal's weight was injected.

3.2.3 MI and MRI

The MI or sham surgeries were performed as previously described in chapter 2. Briefly, mice were anesthetized with an intraperitoneal injection of ketamine/xylazine. The animals had their left anterior descending coronary artery permanently ligated to induce an acute infarction in the left ventricular myocardium. The animals were then allowed to rest for 3 days before MRI.

As described in chapter 2, T_2^*-weighted MR images were acquired on a horizontal 7.0-T, 21-cm MRI spectrometer (Bruker Instruments, Billerica, MA, USA) equipped with

a micro-imaging gradient insert (950 mT/m). A 35mm inner diameter volume coil was used to transmit and receive at ^{1}H frequency (300 MHz). The ECG and respiratory signals were monitored and used for gating by a physiological monitoring system (SA Instruments, INC., Stony Brook, NY). Short-axis images were acquired through the left ventricle and perpendicular to the long axis of the heart using two pulse sequences: (1) a GEFC sequence to acquire the T_2^*-weighted images on which signal intensity and CNR were calculated; and (2) a GEFC cine sequence to acquire the movie of cardiac movement, on which cardiac function was evaluated. The parameters for the GEFC were: TE/TR = 4/120 ms; FA = 30^o; FOV = 30 x 30 mm; slice thickness = 1 mm; matrix = 256 x 256 and 8 averages. The parameters for GEFC cine sequence were: TE/TR = 4/16 ms; FA = 25^o; FOV = 30 x 30 mm; slice thickness = 1 mm; matrix size = 128 x 128; 8 frames in one cardiac cycle and 8 averages. Both pulse sequences were triggered by the R-wave of the ECG signal.

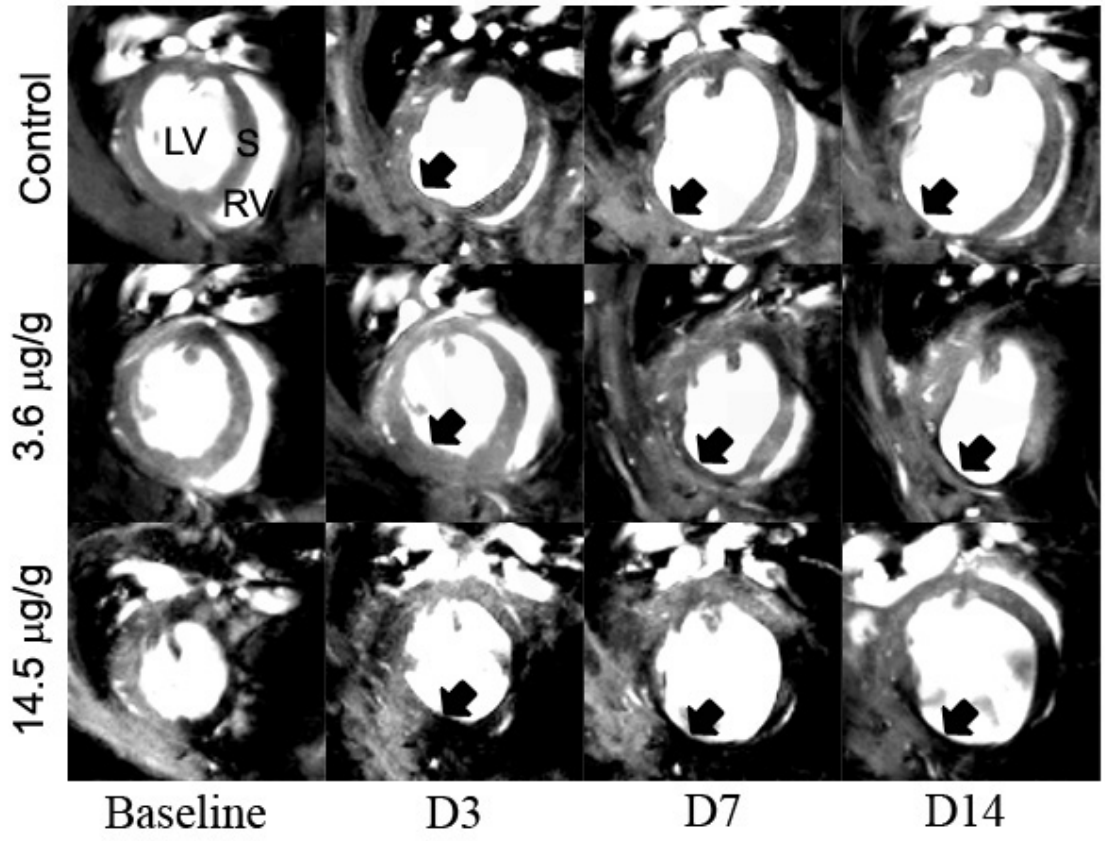

Figure 3.2 T_2^*-weighted longitudinal short-axis cardiac MR images from the macrophage study. The signal intensity at the infarction site (indicated by dark arrows) was attenuated temporally for both groups with iron injection. More signal attenuation was observed at higher dose level at a given time post-MI. LV: left ventricle; RV: right ventricle; S: interventricular septum.

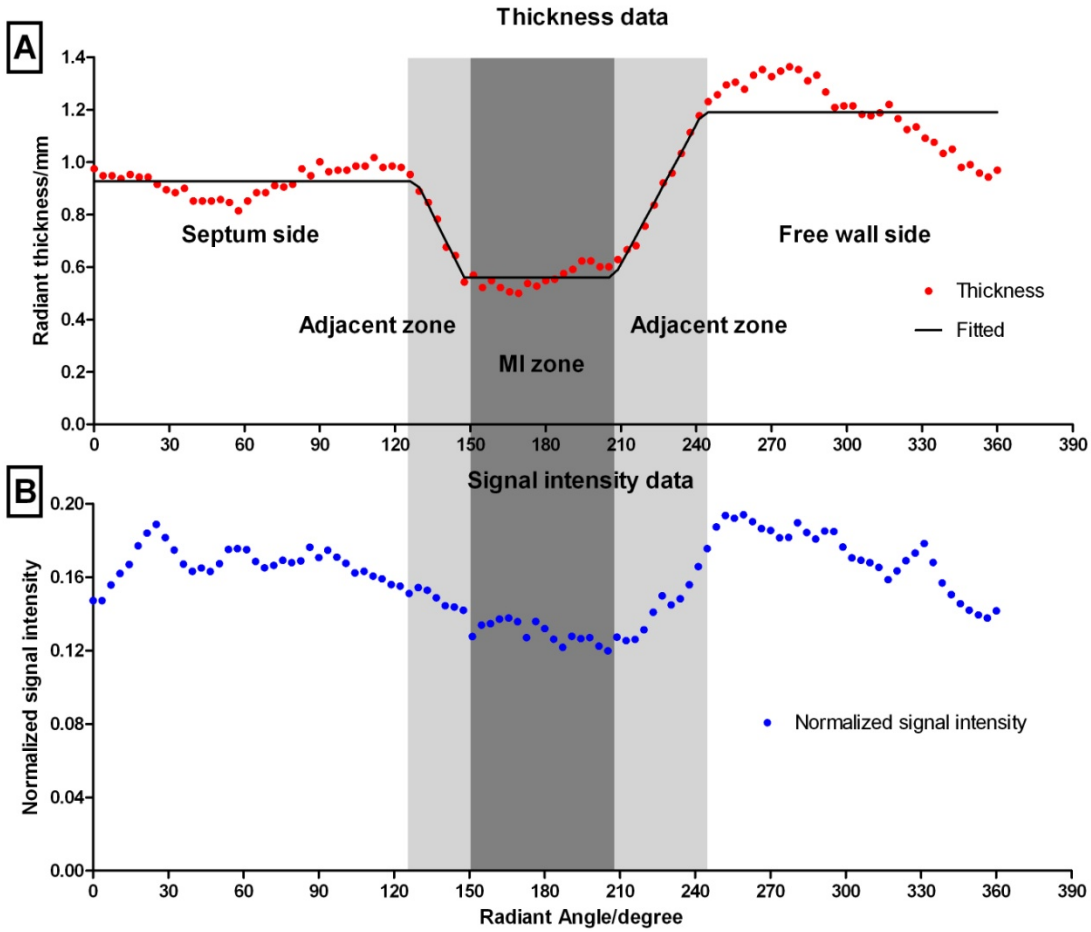

Figure 3.3 Identification of the MI zone. The thickness of the left ventricular wall (A) and normalized MR signal intensity (B) at each radiant angle was plotted. The center of the MI zone was set to 180° as demonstrated in the inserted image on the lower left. The signal intensity at the infarction zone was obtained after the MI zone was identified. Attenuation in both wall thickness and MR signal intensity was demonstrated at the MI zone.

3.2.4 Image Processing and Data Analysis

MR images were processed using an in-house program developed in MATLAB (MathWorks, Inc., Natick, MA). A description of this program can be found in appendix C. Normalized signal intensity (nSI) method was used to illustrate the signal intensity attenuation at the MI site. In the nSI analysis, the signal intensity was normalized to the maximum signal intensity from the ventricular blood. During the image analysis, the left ventricular wall was outlined manually and then its thickness was curve fitted. Examples of cardiac images are shown in Figure 3.2. The infarction site (indicated by arrows) with attenuation in both wall thickness and MR signal intensity can be observed at D7 and D14. By curve fitting the thickness of the left ventricular wall, the MI zone can be automatically identified, as it corresponds to the region with attenuated thickness (Figure 3.3Top). The signal intensity at the infarction site was acquired after the MI zone was identified. (Figure 3.3Bottom). This image analysis procedure by and large reduces the bias otherwise produced when the image analyst subjectively localizes and manually draws the ROIs at the MI site.

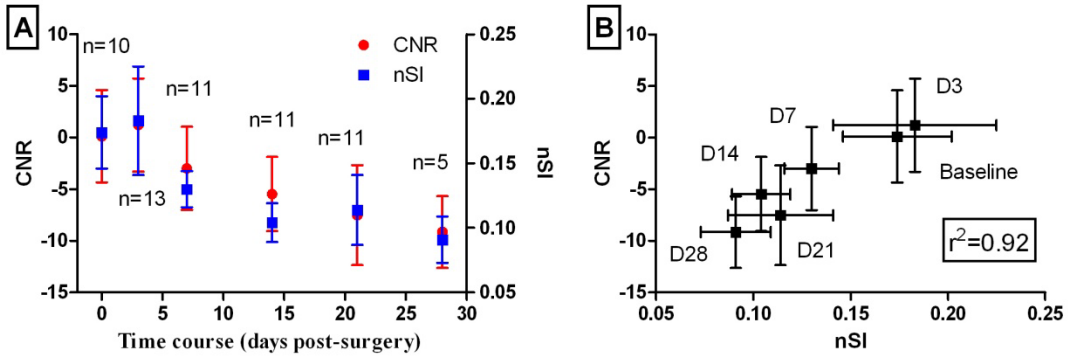

Figure 3.4 Comparison and correlation of CNR and nSI analysis. The data was expressed with mean ± SD. A. CNR and nSI are plotted side by side with scale approximately matched with each other. The coefficient of variance is smaller for nSI at all time points post-MI. B. Pearson correlation analysis demonstrated CNR was well correlated with nSI (r^2=0.92).

A comparison between the nSI and CNR method showed that the nSI method was a better way for quantitative analysis in the current study. In the traditional CNR method, CNR at the MI site was calculated by CNR = $(SI_{MI} - SI_{norm})/SI_{bkg}$. SI_{MI} represents the signal intensity at the infarction region, which was determined as the area with ventricular wall thinning; SI_{norm} represents the signal intensity at the normal myocardium; and SI_{bkg} represents the background noise. Figure 3.4 demonstrates the comparison between the nSI and CNR. A good match between CNR and nSI can be seen in Figure 3.4A, with both showing a similar temporal trend of signal attenuation with time. A significant correlation between nSI and CNR is shown in Figure 3.4B (r^2=0.92, $P < 0.01$). To compare the coefficient of variation (CV) at each time point, the CNR was converted to nSI first, according to the linear regression formular [nSI = 0.009523 x CNR + 0.1704]. The standard deviation (SD) of CNR was also scaled by a multiplication factor of 0.009523. The result is shown in Table 3.1. The CV of the nSI at each time point was

smaller than the scaled CV of CNR [Scaled CV = Scaled SD / Scaled mean]. Therefore, nSI analysis was determined to be a more accurate method and thus was used to quantify the signal attenuation at the MI site.

Table 3.1 Comparison between CNR and nSI

Time	CNR						nSI		
	Mean	SD	CV	Scaled mean	Scaled SD	Scaled CV	Mean	SD	CV
Baseline	0.12	4.47	37.25	0.17	0.04	0.25	0.17	0.03	0.16
D3	1.21	4.51	3.73	0.18	0.04	0.24	0.18	0.04	0.23
D7	-2.98	4.03	1.35	0.14	0.04	0.27	0.13	0.01	0.11
D14	-5.46	3.6	0.66	0.12	0.03	0.29	0.10	0.02	0.14
D21	-7.51	4.84	0.64	0.10	0.05	0.47	0.11	0.03	0.24
D28	-9.14	3.47	0.38	0.08	0.03	0.40	0.09	0.02	0.20

To connect the serial MR signal intensity at the MI site with the cell infiltration rate, the rate of attenuation (ROA) of nSI was calculated [$ROA = ABS(nSI_{current} – nSI_{previous})/nSI_{previous}/(Date_{current} – Date_{previous})$]. ABS is denoted as the mathematical operation of calculating the absolute value. For example, the ROA from 3 to 7 days post-MI is calculated as $ROA_{3\text{-}7} = ABS(nSI_7 – nSI_3)/nSI_3/(7\ day – 3\ day)$]. The unit for ROA is percentage per day (% per day). The ROA is used as an indirect index of labeled cell infiltration rate.

To evaluate the cardiac performance, the LVEF was calculated using the LVEDV and LVESV [LVEF (%) = (LVEDV-LVESV)/LVEDV]. The LVEDV and LVESV were determined from endocardial contours at the end-diastole and end-systole phase,

respectively. The ROIs for calculation were drawn on the continuous short-axis MRI slices from the apex to the base covering the entire heart.

3.2.5 Statistical Analysis

All data were presented as mean ± SEM in the result section. A two-way repeated-measures ANOVA was used to compare the difference in LVEF among the five experimental groups. A Pearson correlation analysis was used to determine if a linear correlation existed between the nSI and the injected MPIO dose at each time point. Student t-test was used to examine the temporal and dose-dependent characteristics of nSI by comparing any dose groups with the control group at each time point. The GraphPad Prism 5.01 (GraphPad Software Inc., San Diego, CA, USA) was used for all statistical analyses. Significance was determined at $P < 0.05$.

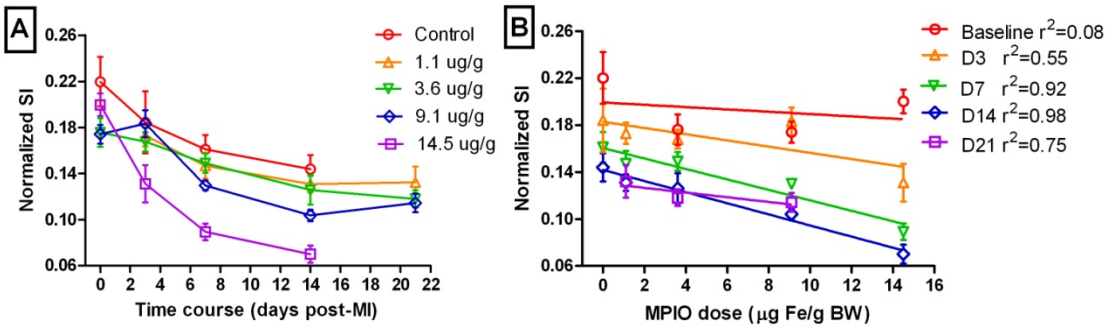

Figure 3.5 Temporal and dose-dependent analysis. A. A dose-dependent plot of normalized signal intensity (nSI) at the infarction site with time. Higher dose level produced more signal intensity attenuation at 7 and 14 days post-MI. B. Linear regression demonstrating a linear signal-dose relationship at 7 (D7) and 14 (D14) days post-MI. BW: body weight.

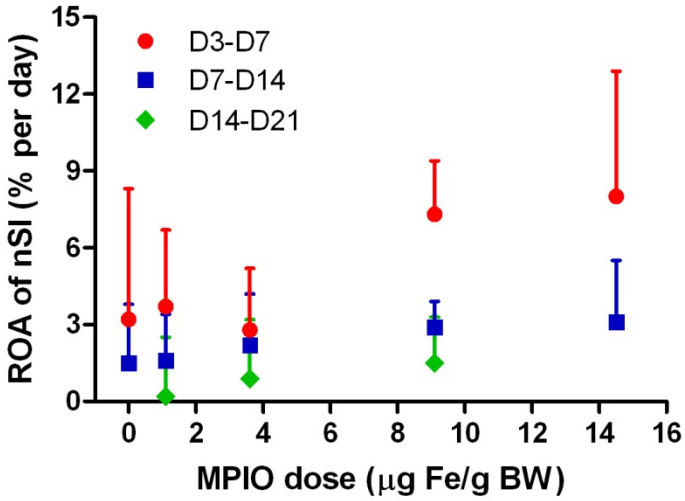

Figure 3.6 Variance of the ROA of the nSI due to differential doses. The ROA of nSI is an indicator of the infiltration rate of the labeled cells to the MI site. D3, D7, D14 and D21 are denoted as 3, 7, 14 and 21 days post-MI. BW: body weight

3.3 RESULTS

The cell infiltration during MI was successfully monitored using MPIO cell labeling and T_2^*-weighted MRI technique. The signal intensity at the MI site was continuously attenuated following infarction until 14 days post-MI, at all dose levels. This dose-dependent study demonstrated that a higher dose produces more attenuation at the infarction site (Figure 3.2). The quantitative results are shown in Figure 3.5. For each dose group, continuous signal attenuation was observed until 14 days post-MI. The signal intensity stabilized after 14 days, which resulted in relatively small signal differences at 21 days post-MI at different dose levels. Most interestingly, an inverse linear relationship between the nSI and MPIO dose was found at both 7 days (r^2=0.92) and 14 days (r^2=0.98) post-MI using linear regression. No such strong relationship was evidenced at other time points (r^2=0.08, 0.55, 0.75 for baseline, 3 days and 21 days post-MI). The inverse linear relationship potentially suggests that higher MPIO doses can effectively lead to more labeled cell accumulation at the MI site. The wide range of signal intensity produced by different doses indicates that MPIO is utilized more effectively at 7 days and 14 days post-MI. The variance of the ROA of the nSI due to differential doses is demonstrated in Figure 3.6. It is deemed that the variance of the ROA at one given temporal interval was primarily caused by the difference in the injected MPIO dose, but not by the surgical variation. The ROA with minimal variation among time points occurred from 7 to 14 days post-MI, indicating that the error caused by the difference in the injected dose can potentially be minimized when using the MR signal intensity to interpret the cell infiltration rate during this time interval. These dose-dependent characteristics suggest an

optimal temporal window for MR imaging of the labeled cells at the MI site, which is determined to be from 7 days to 14 days post-MI.

Table 3.2 P values of student t-test compared with control

Time	1.1 μg/g	3.6 μg/g	9.1 μg/g	14.5 μg/g
Baseline	NA	0.1045	0.0810	0.4121
3 days	0.3449	0.2820	0.4848	0.0576
7 days	0.2209	0.2222	0.0276	0.0004
14 days	0.1915	0.1633	0.0081	0.0002

Note: no data was measured at baseline for 1.1 μg/g dose.

Student t-test was used to compare the signal difference between any dose group and the control group. The results are shown in Table 3.2. Significant differences in signal intensity were found between the control group and the 9.1 μg/g dose group or the 14.5 μg/g dose group, at both 7 days ($P = 0.03$, 0.0004 for the 9.1 μg/g, 14.5 μg/g dose, respectively) and 14 days post-MI ($P = 0.008$, 0.0002 for the 9.1 μg/g, 14.5 μg/g dose, respectively). The signal intensity of lower dose groups was not significantly different from that of the control group at either 7 or 14 days post-MI ($P > 0.05$ for the 1.1 μg/g or 3.6 μg/g dose group). At baseline or 3 days post-MI, there was no significant difference in signal intensity between the control group and any dose group ($P > 0.05$). The significant difference in signal intensity at 7 days and 14 days post-MI indicates that a dose of no less than 9.1 μg/g should be administered in order to quantify the labeled cells at the MI site. However, a dose as high as 14.5 μg/g may cause overdose artifacts in the

posterior ventricular wall and interventricular septum, which also produced signal attenuation and could potentially be misinterpreted as signal attenuation caused by iron oxide particles. A dose less than 9.1 μg/g may not be able to produce sufficient signal attenuation. Therefore, the optimal dose for tracking labeled cells following MI should be no less than 9.1 μg/g, but no more than 14.5 μg/g.

The left ventricular ejection fraction (Table 3.3) was compared using a two-way ANOVA test. The results showed no significant difference in the LVEF by surgical treatment among all animal groups ($P = 0.45$), which indicates that the signal attenuation at the MI site was not caused by surgical variation. Since the variation in MPIO dose did not affect the cardiac function, the animals from different dose groups were grouped together to examine the alteration of cardiac function parameters following MI. Those results are shown in Table 3.4. Following MI, both the LVEDV and LVESV increased with time, but the LVEF decreased. The most dramatic changes in cardiac remodeling occurred within 14 days post-MI. The situation stabilized after 14 days. This cardiac function turnover matched the findings on signal intensity, which also reached a minimum at 14 days post-MI.

Table 3.3 Left ventricular ejection fraction (%)

Time	Control	1.1 μg/g	3.6 μg/g	9.1 μg/g	14.5 μg/g
Baseline	69.34±3.29	NA	72.26±2.03	73.34±1.38	70.68±1.79
D3	51.26±4.33	54.99±1.33	48.91±2.10	52.90±3.14	49.68±3.50
D7	38.09±2.75	47.40±2.70	38.88±4.19	46.63±4.20	41.28±3.39
D14	43.42±4.07	50.86±1.50	40.19±4.40	48.11±4.91	41.16±4.10

Note: the numbers of samples for each measurement varies from 6 to 13. Data for group 1.1 μg/g at baseline was not measured.

Table 3.4 Cardiac physiology data

Time	EDV (mL)	ESV (mL)	SV (mL)	LVEF (%)	LVWM (mg)
Baseline	49.43±1.68	13.87±0.95	35.55±1.17	72.12±1.32	107.84±2.84
D3	65.41±2.36	32.45±1.96	32.96±1.40	50.68±1.89	118.91±2.59
D7	84.00±4.80	50.68±5.05	33.32±1.11	41.77±2.84	127.44±3.83
D14	92.61±6.41	56.97±7.40	35.64±1.45	42.01±3.61	168.44±4.71
D21	97.69±7.94	58.83±8.38	38.86±1.31	43.58±3.29	133.25±3.25
D28	101.11±9.00	61.10±8.66	40.01±1.34	42.96±2.86	143.79±5.09

Note: the data was from 16 animals that received varied doses. EDV, ESV, SV, LVEF and LVWM denote left ventricular end-diastolic volume, end-systolic volume, stroke volume, ejection fraction and wall mass, respectively.

3.4 DISCUSSION

This study demonstrated an indirect method for quantification of labeled cell infiltration in cardiac MRI by using signal intensity at regions of interest normalized to the signal intensity from the ventricular blood. The image analysis showed that the normalized signal intensity has a smaller systemic statistical variation than CNR dose. The systemic deviation stems mainly from the variation of scan parameters such as the acquisition gain or even attenuation values, which are subject to the user's setup during each imaging session. To achieve optimal image quality, it is necessary to increase the acquisition gain as the iron oxide particles accumulation in injured tissues inside an imaging plane caused pronounced signal attenuation. The changes of acquisition gain as well as the fluctuation of spectrometer over time could influence the CNR, in particular, by causing dramatic variations in background noise. When using signal intensity as an analysis index, it is intuitive and common to normalize the signal intensity at a region of interest to that from a phantom which may contain water or oil. In cardiac imaging, the ventricular blood provides a natural and convenient phantom for signal correction, as long as the blood is not contaminated with contrast media. In this study, the MPIO were rapidly washed out of the blood, with a half life of less than 1 minute. Consequently, it was determined that the ventricular blood should not be contaminated by MPIO at the time of MRI.

Iron oxide particles provide image contrast by causing signal loss at the MI site. However, it is difficult to differentiate the signal attenuation caused by labeled cells from that caused by hemorrhage. Attenuation due to hemorrhage also can affect signal intensity measurement even in the case of signal enhancement through positive contrast

agents. Although some imaging sequences or post-processing methods have been tried via recognition of the signal pattern caused by iron oxide particles[14-21], execution of these methods usually requires a great deal of effort for preparation and optimization. In addition, some methods become impractical when many labeled cells cluster together and a great number of particles accumulate even in one single image voxel, which is usually the case when iron oxide particles are administered intravenously. While using relaxation time T_2 or T_2^* is a better choice for quantification than using signal intensity, several limitations exist in cardiac imaging. First, the image registration in multi-echo sequences is sensitive to cardiac motion. Second, T_2^* can be shortened to such a large extent that T_2^* measurement may have an intolerable error. In addition, detecting a short T_2^* requires a short starting echo time and thus a high power. Future investigation such as using MRS is encouraged to generate better methodology for quantification of labeled cells.

The activity of labeled cells infiltration intensified within 14 days post-MI and caused significant signal attenuation at the MI site from 7 days to 14 days post-MI. A wide range of signal intensity produced by varied doses during this optimal temporal imaging window suggests that further experiments in quantification of labeled cells at the MI site should be performed within this time interval. In future research, MRI experiments performed on more time points between 3 and 14 days post-MI may refine the optimal temporal window for the interpretation of the cell infiltration rate. It will be necessary to find a better way to correlate the signal intensity or relaxivity with the cell infiltration rate, or even with the number of labeled cells at the MI site. The ROA of the nSI at the MI site is an indirect index for the infiltration rate of the labeled cells. While the ROA correlates closely with the cellular activity, it may be affected by other factors.

For instance, the dose difference may lead to variation in *in vivo* cell labeling efficiency. Because no significant difference in the LVEF was observed among all dose groups, the variance of the ROA due to variation in surgical procedures was minimized. Further experiments can be performed to test whether the technique developed from this study is sensitive enough to differentiate any drug effect on labeled cell mobilization.

3.5 CONCLUSIONS

This study provided a convenient method to quantify signal intensity attenuation caused by labeled cells in cardiac MRI. The signal intensity at the infarction site normalized to that from the ventricular blood was well correlated with the CNR but had less variation than the CNR did. The study suggests that the dose to quantify any effect on cell infiltration by potential treatment strategies should be no less than 9.1 μg/g but no greater than 14.5 μg/g. A dose-dependent phenomenon of labeled cell infiltration into the MI site was evidenced, each dose leading to a different number of labeled cells at the MI site reflected from the MR signal intensity attenuation. Furthermore, a linear dependence of MR signal intensity on injected MPIO dose was observed at 7 and 14 days post-MI. This linear signal-dose relationship further suggests an optimal temporal imaging window, which is between 7 and 14 days post-MI. During this time interval, the variance of ROA of the nSI due to the dose difference was also minimized. Future investigation is necessary to delineate a direct relationship between the signal intensity and the cell infiltration rate, or even the relative number of labeled cells at the infarction site. The current cell labeling and MR imaging techniques can potentially be applied to track and quantify cell infiltration in cell therapy and drug treatment or to monitor disease progression in both clinical and preclinical study.

3.6 REFERENCES

1. Frangogiannis NG, Smith CW, Entman ML. The inflammatory response in myocardial infarction. Cardiovasc Res. 2002; 53(1):31-47.

2. Fujiwara N, Kobayashi K. Macrophages in inflammation. Curr Drug Targets Inflamm Allergy. 2005; 4(3):281-286.

3. Metz S, Bonaterra G, Rudelius M, et al. Capacity of human monocytes to phagocytose approved iron oxide MR contrast agents in vitro. Eur Radiol. 2004; 14(10):1851-1858.

4. Raynal I, Prigent P, Peyramaure S, et al. Macrophage endocytosis of superparamagnetic iron oxide nanoparticles: mechanisms and comparison of ferumoxides and ferumoxtran-10. Invest Radiol. 2004; 39(1):56-63.

5. Williams JB, Ye Q, Hitchens TK, et al. MRI detection of macrophages labeled using micrometer-sized iron oxide particles. J Magn Reson Imaging. 2007; 25(6):1120-1128.

6. Henning EC, Ruetzler CA, Gaudinski MR, et al. Feridex preloading permits tracking of CNS-resident macrophages after transient middle cerebral artery occlusion. J Cereb Blood Flow Metab. 2009; 29(7):1229-1239.

7. Saleh A, Schroeter M, Ringelstein A, et al. Iron oxide particle-enhanced MRI suggests variability of brain inflammation at early stages after ischemic stroke. Stroke. 2008; 38(10):2733-2737.

8. Kanno S, Wu YJ, Lee PC, et al. Macrophage accumulation associated with rat cardiac allograft rejection detected by magnetic resonance imaging with ultrasmall superparamagnetic iron oxide particles. Circulation. 2001; 104(8):934-938.

9. Chang HH, Moura JM, Wu YL, et al. Immune cells detection of the in vivo rejecting heart in USPIO-enhanced magnetic resonance imaging. Conf Proc IEEE Eng Med Biol Soc. 2006; 1:87-89.

10. Sosnovik DE, Nahrendorf M, Deliolanis N, et al. Fluorescence tomography and magnetic resonance imaging of myocardial macrophage infiltration in infarcted myocardium in vivo. Circulation. 2007; 115(11):1384-1391.

11. Brisset JC, Desestret V, Marcellino S, et al. Quantitative effects of cell internalization of two types of ultrasmall superparamagnetic iron oxide nanoparticles at 4.7 T and 7 T. Eur Radiol. 2010; 20(2):275-285.

12. Shapiro EM, Skrtic S, Koretsky AP. Sizing it up: cellular MRI using micron-sized iron oxide particles. Magn Reson Med. 2005; 53(2):329-338.

13. Yang Y, Yanasak N, Schumacher A, et al. Temporal and noninvasive monitoring of inflammatory-cell infiltration to myocardial infarction sites using micrometer-sized iron oxide particles. Magn Reson Med. 2010; 63(1):33-40.

14. Haacke EM, Xu Y, Cheng YC, et al. Susceptibility weighted imaging (SWI). Magn Reson Med. 2004; 52(3):612-618.

15. de Crespigny AJ, Roberts TP, Kucharcyzk J, et al. Improved sensitivity to magnetic susceptibility contrast. Magn Reson Med. 1993; 30(1):135-137.

16. Mills PH, Wu YJ, Ho C, et al. Sensitive and automated detection of iron-oxide-labeled cells using phase image cross-correlation analysis. Magn Reson Imaging. 2008; 26(5):618-628.

17. Cunningham CH, Arai T, Yang PC, et al. Positive contrast magnetic resonance imaging of cells labeled with magnetic nanoparticles. Magn Reson Med. 2005; 53(5):999-1005.

18. Mani V, Briley-Saebo KC, Itskovich VV, et al. Gradient echo acquisition for superparamagnetic particles with positive contrast (GRASP): sequence characterization in membrane and glass superparamagnetic iron oxide phantoms at 1.5T and 3T. Magn Reson Med. 2006; 55(1):126-135.

19. Warren WS, Ahn S, Mescher M, et al. MR imaging contrast enhancement based on intermolecular zero quantum coherences. Science. 1998; 281(5374):247-251.

20. Seppenwoolde JH, Viergever MA, Bakker CJ. Passive tracking exploiting local signal conservation: the white marker phenomenon. Magn Reson Med. 2003; 50(4):784-790.

21. Robson MD, Gatehouse PD, Bydder M, et al. Magnetic resonance: an introduction to ultrashort TE (UTE) imaging. J Comput Assist Tomogr. 2003; 27(6):825-846.

CHAPTER 4
MONITORING MESENCHYMAL STEM CELL INFILTRATION

4.1 INTRODUCTION

A major complication of MI is heart failure[1], since the scar tissue healing over the necrosed myocardium contains no contractile or pacemaker myocytes[2]. Stem cell-based therapies have been explored to potentially regenerate healthy tissue at MI sites, given that the heart lacks the necessary cardiomyocyte progenitors to do so by itself[3]. However, the roles of stem cells in the myocardial repair and remodeling processes are yet to know[4,5].

Cells such as ESC[6], human ESC-derived cardiomyocytes[7], skeletal myocytes[8] and bone marrow-derived stem cells[9,10] have been previously transplanted into infarcted myocardium. However, complications have occurred when applying these cells to myocardial repair, including adverse immunological response and/or teratoma formation[11], highly complex harvest process[12] and failure to functionally integrate with the host tissue[13]. Compared with other cell types, MSC demonstrate advantages in cardiac cell therapy since they exhibit a multi-lineage plasticity, a reduced immune response, and an easy harvest process[14,15]. Research by Quevedo et al[16] showed that MSC were capable of restoring cardiac function with an increase of ejection fraction from 35.0±1.7% to 41.3±2.7 over 12 weeks in swine receiving transendocardial injection of 200 million MSC.

Previous studies attempted to improve cardiac structure and function by directly delivering labeled stem cells into the damaged myocardium. However, this method

usually led to severe cell loss[12]. Studies also showed that intracoronary and intravenous injections were no more successful than the intramyocardial route at rendering satisfactory graft efficiency[17-19]. Furthermore, transfer of iron oxide particles form originally labeled cells to macrophages can lead to false interpretation of MRI data[20,21], which imposes additional disadvantage for intramyocardial delivery. Intra-bone marrow transplantation is an alternative delivery method, which has exhibited improved engraftment[22]. The bone marrow milieu provides a native environment for transplanted cell engraftment and proliferation.

Therefore, the purpose of this study was to investigate MSC' infiltration traffic from the bone marrow to MI sites by an intra-bone marrow cell delivery method. MSC were labeled with enhanced green fluorescent protein (GFP) and MPIO, which are also tagged with a Suncoast Yellow fluorescent dye. MPIO labeling enabled the noninvasive cell tracking with MRI. Fluorescence from both GFP and MPIO was used to confirm the MRI findings by histological fluorescent imaging. This study intended to demonstrate that combining intra-bone marrow cell delivery, dual-cell labeling and MRI cell tracking is a promising methodology for studying stem cells mobilization in animal MI models.

4.2 METHODS

4.2.1 Overall Experimental Protocol

All animal procedures were performed in compliance with the Institutional Animal Care and Use Committee at the Medical College of Georgia, Augusta, GA. Adult male C57Bl/6 mice (6-12 weeks old, 23.8±3.0 g) underwent irradiation, unlabeled rescuing bone marrow cell transplantation (one day after irradiation), and transplantation

of the labeled MSC (two days after irradiation). At 14 days after labeled MSC transplantation, one animal group underwent MI surgery as an experimental group (Experimental group, n=7); another group underwent sham-operated surgery (thoracotomy without any heart injury) as a sham control group (Sham control, n=7). A third group receiving neither irradiation nor cell transplantation underwent MI surgery (MI control, n=6) as MI control. MRIs were performed on all mice at baseline, 3 days (D3), 7 days (D7), and 14 days (D14) post-MI or sham surgery. Figure 4.1 illustrates the overall experimental time course.

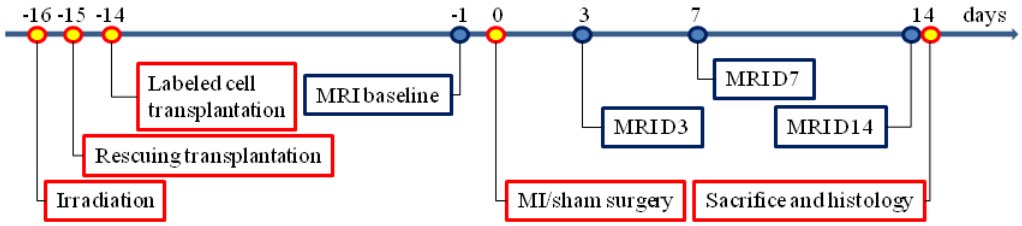

Figure 4.1 Experiment time course.

4.2.2 MSC Isolation and Culture

Bone marrow was harvested from 18-month-old C57Bl/6 mice by flushing the femora and tibiae with complete isolation medium (CIM) consisting of RPMI-1640 with 9% heat-inactivated fetal bovine serum, 9% horse serum, 100 U/mL penicillin, 100 µg/mL streptomycin, and 12 µmol/L L-glutamine[23]. The bone marrow was then dispersed into single-cell suspension and plated in flasks. To minimize MSC contamination with hematopoietic progenitor cells, the bone marrow cell suspension was allowed to adhere to the flasks for 3 hours at 37°C in a 5% CO_2 atmosphere[24]. The media was then removed,

the flask containing adherent cells gently washed with phosphate-buffered saline (PBS), and the cells cultured in CIM until they reached 80% confluence. Cells were then lifted by trypsin and subjected to negative immuno-selection by using magnetic beads to remove any hematopoietic lineage cells[25]. The magnetic beads had been conjugated with CD11b, CD11c, CD45R/220B, and PDCA-1 monoclonal antibody. The hematopoietic lineage cells removed in this process included granulocytes, macrophages, myeloid-derived dendritic cells, natural killer cells, B-1 cells, B lymphocytes, T lymphocytes, classical dendritic cells, plasmacytoid dendritic cells, and macrophage progenitors. Lastly, all cells negative for these antigens were subjected to a positive immuno-selection using stem cell antigen-1 (Sca-1) monoclonal antibody conjugated magnetic beads.

4.2.3 MSC Labeling and Delivery

First, MSC were fluorescently labeled with GFP via infecting the cells with retroviral vectors expressing GFP (ΔU3-GFP)[26]. The GFP allowed cells to be visualized in fluorescent imaging. Next, the MSC were magnetically labeled with 1.63 μm MPIO (Bangs Laboratories, Fishers, IN). MPIO have a polymer-coated magnetite core (42.5% weight) and are tagged with a Suncoast Yellow fluorescent dye. The magnetic core and Suncoast Yellow fluorescence allowed MPIO to be visualized via MR and fluorescent imaging, respectively. For labeling, MPIO were opsonized in 50% fetal bovine serum for 1 hour at 37^{o}C, washed in PBS and resuspended in 1 mL expansion media with a concentration of 1x10^{8} MPIO per mL. Then MSC were incubated in 10 mL of media with a concentration of 10^{6} MPIO per mL for 48 hours.

Labeling outcomes were evaluated using a Zeiss Axiovert 10 microscope (Carl Zeiss, Jena, Germany) with a SPOT camera and software (Diagnostic Instruments,

Sterling Heights, MI). The dual-labeled MSC were identified by the co-localization of GFP and Suncoast Yellow fluorescence. Labeling efficiency was measured by randomly selecting labeled-cell cultures. The ratio of the number of dual-labeled cells to the total cell number was calculated within a single fluorescent image (20x magnification). MSC were further examined under an electron microscope to confirm MPIO were inside the cells. These dual-labeled cells maintained their capability of differentiation during a 10-day observation. More information about MSC differentiation in culture and bone marrow can be found in appendix B.

For the Experimental and Sham control groups, animals underwent irradiation with ^{137}Cs using a Gammacell 40 irradiator (Best Theratronics, Ottawa, ON, Canada). A dose of 8.0 Gy was used to ablate the bone marrow. The animals received a rescuing donation of unlabeled ~0.5-2 $x10^6$ bone marrow cells via retro-orbital plexus injection within 24 hours after irradiation. Two days after the irradiation, each animal was properly anesthetized with a mixture of medical air, oxygen (1:1), and ~2.0% isoflurane (Abbott Laboratories, Abbott Park, IL), and a hole was drilled into the proximal articular surface with a 26-gauge needle. Then ~30-50 μL of bone marrow was aspirated from the bone marrow cavity, and ~$6.6x10^5$ GFP and MPIO dual-labeled MSC (1.3 million cells per mL in PBS) were transplanted into the tibial medullary space. The mice were allowed to recover in a post-operative recovery chamber under careful supervision before being returned to their cages.

4.2.4 MI and MRI

The MI and sham surgeries were performed two weeks after MSC transplantation using previously described procedures[27]. Briefly, mice were anesthetized with an intraperitoneal injection of ketamine/xylazine at a dose of 2 μL/g body weight. The sham-group mice had their chests immediately sutured after performing the thoracotomy without injuring the heart. The MI-group mice had their left anterior descending coronary artery permanently ligated to produce an acute infarction in the left ventricular myocardium. The mice were then allowed to recover for 3 days before next MRI.

MRI procedures were conducted using a previously described protocol[27]. Briefly, each mouse was anesthetized with a mixture of medical air, oxygen (1:1), and 1.5-2.0% isoflurane, maintaining a respiration rate of 61±6 breaths per minute and a heart rate of 434±58 beating per minute for all MRI sessions. MRI was performed on a horizontal 7-T MRI spectrometer (Bruker Instruments, Billerica, MA). Short-axis cardiac images were acquired through the left ventricle perpendicular to the long axis of the heart using two pulse sequences: (1) an ECG-gated GEFC sequence that acquired single T_2^*-weighted images, and (2) an ECG-gated GEFC cine sequence that acquired movies of cardiac movement during the cardiac cycle. The GEFC sequence was sensitive enough to detect the signal attenuation generated by MPIO, while the LVEF was calculated from the GEFC cine sequences.

LVEF was calculated using the LVEDV and LVESV determined from the endocardial contours in the end-diastolic and end-systolic phases, respectively [LVEF(%) = (LVEDV-LVESV)/LVEDV]. CNR at the MI site was calculated using signal intensity

measurements in the GEFC T_2^*-weighted images [CNR = (SI_{MI} - SI_{norm})/SI_{bkg}]. The SI_{MI} represented the signal intensity at the MI region located where the left ventricular wall thinned; the MI region was confirmed by the akinetic contractility area seen in the cine images. The SI_{norm} represented the signal intensity in the normal (non-infarcted) myocardium and the SI_{bkg} represented the background noise.

4.2.5 Histology

After completing the final MRI session and while still anesthetized, each animal was sacrificed by perfusing the body with 4% paraformaldehyde (PFA) injected into the inferior vena cava. Once the blood was flushed out, the heart was removed from the body. After two days in PFA, the heart was immersed in 30% sucrose and then sectioned into 10 μm-thick transverse slices along the longitudinal axis. These tissue slices were then immuno-labeled with antibodies against a fibroblast marker ER-TR7, macrophage/monocyte marker F4/80 and CD11. All slices were examined under a confocal microscopy (Zeiss LSM 510 laser scanning microscope; Carl Zeiss, Jena, Germany) for fluorescent imaging.

4.2.6 Statistical Analysis

All data were presented as mean ± SEM. A two-way repeated-measures ANOVA analysis was used to compare differences in CNR and LVEF values between different groups followed by Bonferroni post-hoc tests. The GraphPad Prism 5.01 (GraphPad Software Inc., San Diego, CA) was used for all statistical analyses with a significance level determined at $P < 0.05$.

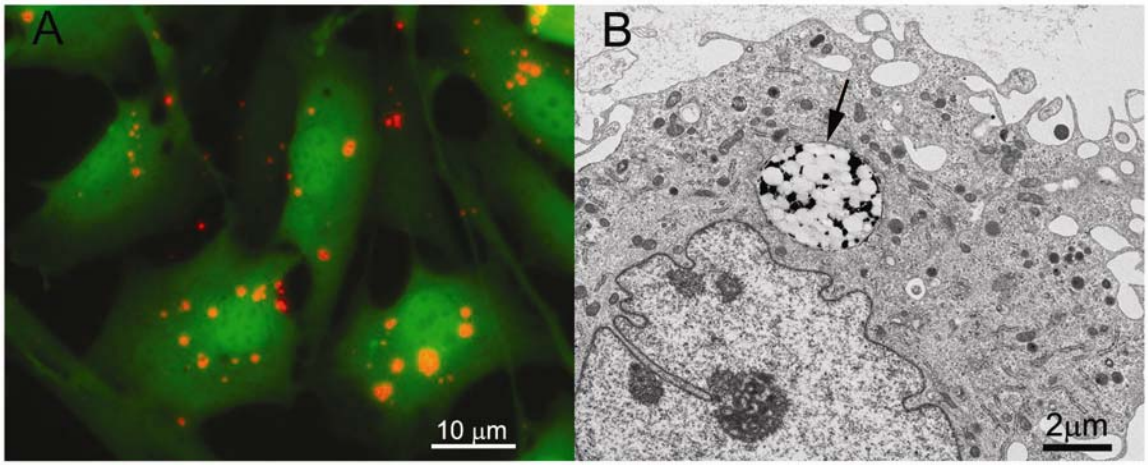

Figure 4.2 Dual-labeled MSC with GFP and MPIO. A. A merged fluorescent image of dual-labeled MSC. The GFP expression is in green and MPIO are indicated by red spots. B. Image from an electron microscope showing MPIO engulfment inside a cell. The black arrow indicates a MPIO particle.

4.3 RESULTS

4.3.1 MSC Labeling

Figure 4.2 demonstrates the dual-labeled MSC. Figure 4.2A shows the co-localization of GFP and MPIO in these cells with the GFP expression shown in green and MPIO represented by red spots. Figure 4.2B is an image from an electron microscopy confirming that MPIO were incorporated into the MSC. Based on ten random measurements (n=10), a labeling efficiency of 97.2 ± 1.5% was calculated for MPIO cell labeling.

4.3.2 MRI Cell Tracking

Figure 4.3 shows an example of longitudinal T_2^*-weighted MR images acquired to monitor labeled MSC infiltration into the MI sites. Gradual signal attenuation was observed in infarction sites over time for the Experimental group. No remarkable attenuation was observed at the corresponding sites for the Sham control mouse. Low signal intensity localized in the posterior left ventricular wall was presumably artifacts caused by cardiac motion rather than iron oxide particles.

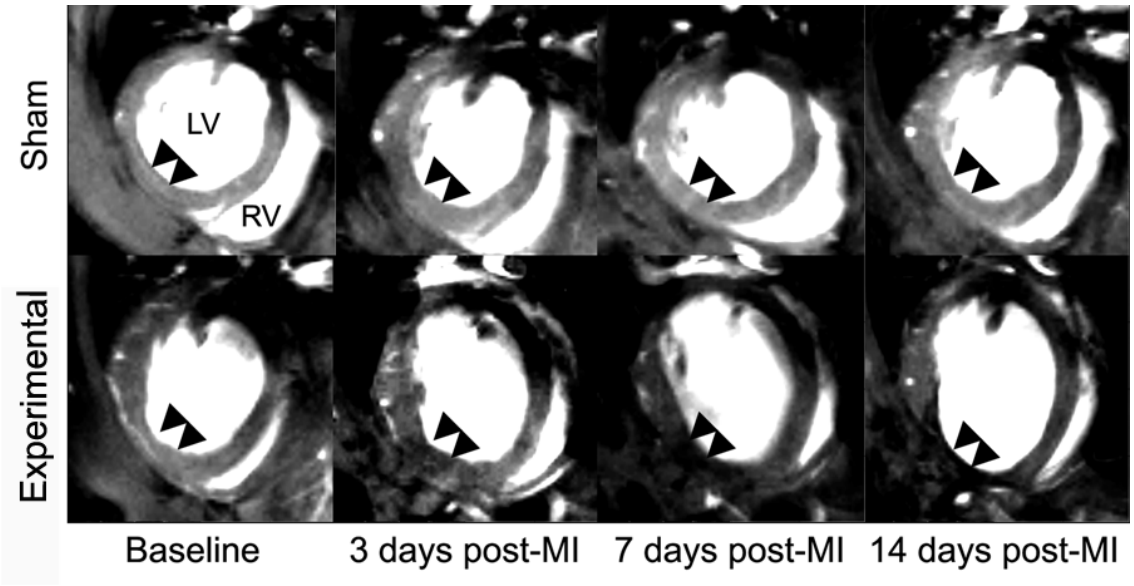

Figure 4.3 T_2^*-weighted short-axis cardiac MR images. Gradual signal attenuation was observed at MI sites for the Experimental group, suggesting labeled cells accumulation. No remarkable signal attenuation was observed for sham group. Arrows indicate MI or corresponding sites. MI: myocardial infarction. LV: left ventricle. RV: right ventricle.

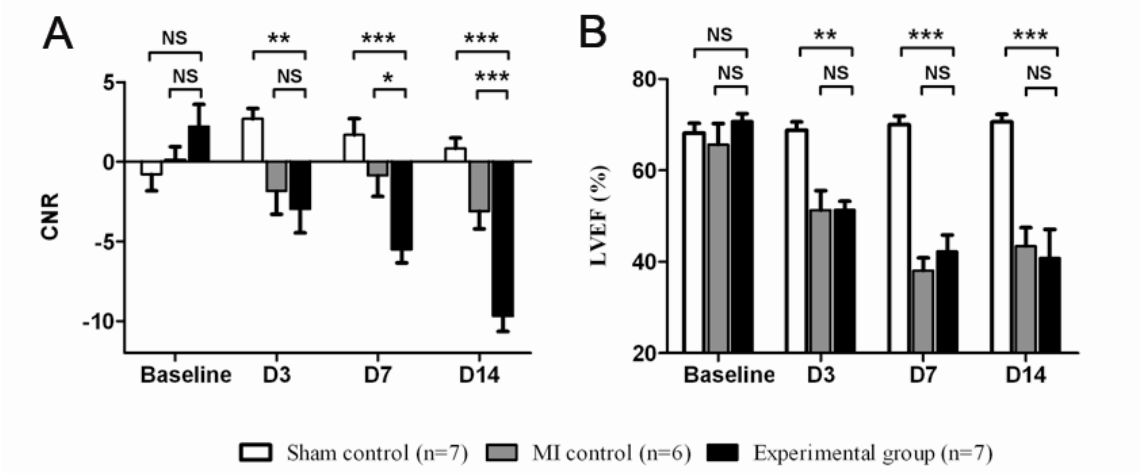

Figure 4.4 CNR and LVEF. A. Continuous CNR attenuation for the Experimental group suggests labeled MSC infiltration into MI sites. B. Decrease in LVEF for both the experimental and MI control group evidences MI-caused cardiac dysfunction. NS: not significant; (*) $P < 0.05$; (**) $P < 0.01$; (***) $P < 0.001$.

Temporal infiltration of MPIO-labeled MSC at the MI site was quantified using CNR (Figure 4.4A). The negative CNR values seen for the Experimental group represents signal attenuation around the MI site indicative of MPIO-labeled cell infiltration. The continuous CNR attenuation over time denotes an increased MPIO-labeled cell infiltration into the infarction site, which was not observed in either the Sham or MI control group. Two-way repeated measures ANOVA test showed significance difference in CNR among all groups ($P < 0.0001$). As expected, no significant difference in CNR were found between any two groups at baseline ($P > 0.05$). Significant differences in CNR were found between the experimental group and Sham control group at 3 days ($P < 0.01$), 7 days ($P < 0.001$) and 14 days ($P < 0.001$) post-MI, and between the experimental group and MI control group at 7 days ($P < 0.05$) and 14 days ($P < 0.001$). The post-MI CNR attenuation for the MI control group was presumably caused by unintended hemorrhage during the surgical formation of the MI. The pronounced signal

attenuation for the Experimental group indicates that the MPIO-labeled cells mobilized into the MI site from bone marrow and was successfully monitored with the T_2^*-weighted MRI technique.

LVEF was evaluated as a representation of cardiac performance (Figure 4.4B). As expected, LVEF decreased following the MI surgery and gradually stabilized after 7 days for both the Experimental and MI control group. Two-way repeated measures ANOVA test showed significance difference in LVEF among all groups ($P < 0.0001$). While no significant difference in LVEF were found between any two groups at baseline ($P > 0.05$), significant differences in the LVEF were found between the Experimental group and Sham control group at 3 days ($P < 0.01$), 7 days ($P < 0.001$) and 14 days ($P < 0.001$) post-MI. No significant difference was found between the experimental group and MI control group at each time point ($P > 0.05$).

4.3.3 Histological Fluorescent Imaging

Fluorescent confocal imaging provided a 3-dimentional view of the histology slices. Therefore this method is well-suited to examine the co-localization of dual labels. Figure 4.5A illustrated the dual-labeled MSC at the MI site, with GFP labeling identified by the green color and MPIO labeling by the red spots. This finding confirmed that dual-labeled MSC mobilized from the bone marrow into the MI site, thus validating MRI findings. Figure 4.5B shows that a subset of GFP labeled MSC were also positive for ER-TR7 (i.e., the fibroblast biomarker). This merged image shows ER-TR7 expression in red and GFP in green. The overlap between ER-TR7 and GFP turned the color yellow, suggesting that a population of transplanted MSC differentiated into fibroblasts at the MI

site. These histological findings confirmed that the dual-labeled MSC maintained their capability of proliferating, migrating and differentiating following intra-bone marrow transplantation. Additional immunohistological staining with F4/80 and CD11b antibodies, two macrophage biomarkers, demonstrated no macrophages with MPIO particles.

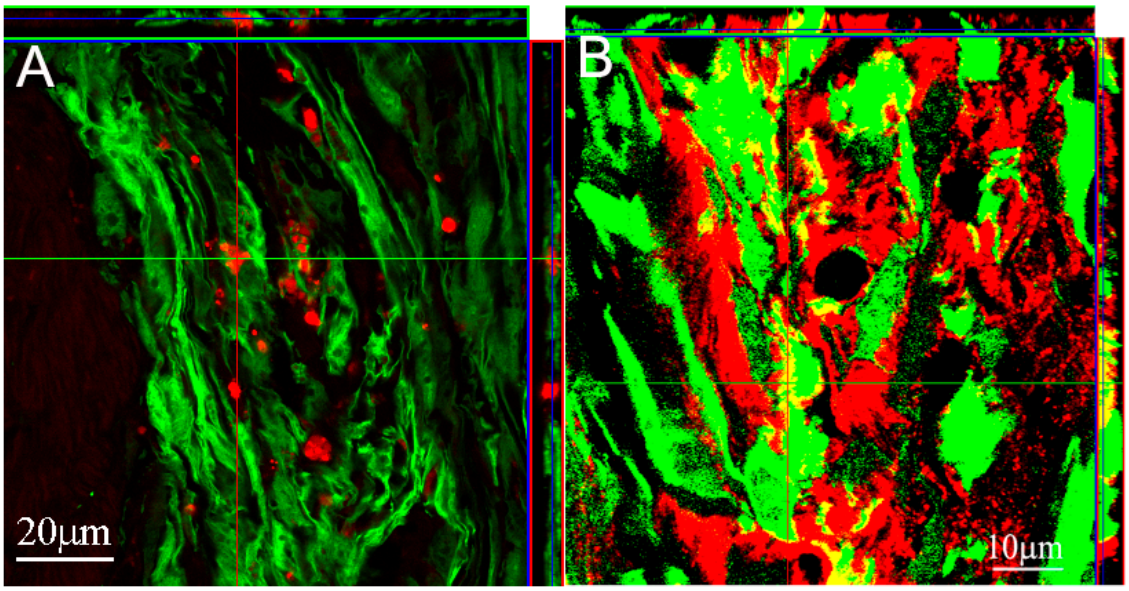

Figure 4.5 Three-dimensional histological fluorescent images. A. Dual-labeled MSC contained both GFP (green color) and MPIO particles (red spots). B. GFP+ MSC and/or derivatives (green color) were positive to ER-TR7 antibody, a fibroblast marker (red color). Overlap of ER-TR7 and GFP turned out to be yellow.

4.4 DISCUSSION

This study demonstrated how combining the *in vivo* MRI and *ex vivo* fluorescent imaging techniques assessed the temporal characteristics of MSC homing to MI sites following their intra-bone marrow transplantation. Dual labeling of MSC with GFP and MPIO allowed noninvasively and temporally tracking MSC infiltration into the MI site, as well as histological confirmation of the MRI findings. MRI data illustrated the post-MI attenuation of CNR over time, indicating that mediation of MSC in myocardial remodeling lasted at least two weeks. MRI findings were confirmed by histological fluorescent imaging, in which a considerable number of dual-labeled cells were observed around the MI site.

The intra-bone marrow transplantation technique provided a unique cell delivery method for studying bone marrow-originated stem cells in post-MI animal models, since the bone marrow provides a native environment for implanted cells to survive and proliferate. This study showed that dual-labeled MSC maintained their capability of migrating and differentiating following intra-bone marrow transplantation. Once irradiation prepared the bone marrow for MSC engraftment, the two-week span between the transplantation and sham/MI surgeries proved to be an adequate amount of time for this cell engraftment to occur. More information about MSC engraftment in the bone marrow can be found in appendix B.

In this research, the MI was determined by the thinning of the infarction area and further confirmed by its contraction inability. In the future study, the infarction area can be outlined with some other objective methods. For example, the infarction site may be

outlined by using gadolinium-based contrast agent to enhance the MR signal *in situ*. Interestingly, in histology it was observed that some dual-labeled cardiomyocyte-like cells were inserted between the host myocardial cells based on cell morphology. However, it warrants further investigation to confirm that those transplanted cells are able to differentiate into cardiomyocytes (e.g., by using cardiomyocyte-specific staining to confirm that some dual-labeled cells are cardiomyoctes).

4.5 CONCLUSIONS

This study applied a dual labeling approach to monitor bone marrow-originated MSC traffic to the MI site. MPIO labeling produced a hypointensity in MR images and enabled noninvasive and temporal cell tracking. The fluorescent labeling allowed for *ex vivo* examination of labeled cells to confirm MRI findings. This technique with dual-labeling, bone marrow transplantation and multiple imaging modalities provides a unique approach to investigate bone-marrow originated stem cells in cardiac remodeling. Once the dual-labeled cells infiltrated into the infarcted heart, they maintained their ability to divide and differentiate and would contribute to healing process. In this manner, signaling pathways for tissue repair by stem cells can be tested and alteration in cell infiltration flux can be monitored. Therefore, this technique has a potential application of monitoring treatment effects on cell mobilization and infiltration at diseased sites in drug development or post-treatment evaluation process.

4.6 REFERENCES

1. Velagaleti RS, Pencina MJ, Murabito JM, et al. Long-term trends in the incidence of heart failure after myocardial infarction. Circulation 2008;118(20):2057-2062.

2. Opie LH. Heart physiology: from cell to circulation. 4th edition. Philadelphia: Lippincott Williams & Wilkins 2004.

3. Li SC, Wang L, Jiang H, et al. Stem cell engineering for treatment of heart diseases: potentials and challenges. Cell Biol Int 2009;33(3):255-267.

4. Murry CE, Field LJ, Menasche P. Cell-based cardiac repair: reflections at the 10-year point. Circulation 2005;112(20):3174-3183.

5. Menasche P. Cell-based therapy for heart disease: a clinically oriented perspective. Mol Ther 2009;17(5):758-766.

6. Yang L, Soonpaa MH, Adler ED, et al. Human cardiovascular progenitor cells develop from a KDR+ embryonic-stem-cell-derived population. Nature 2008;453(7194):524-528.

7. Kehat I, Khimovich L, Caspi O, et al. Electromechanical integration of cardiomyocytes derived from human embryonic stem cells. Nat Biotechnol 2004;22(10):1282-1289.

8. Menasche P. Skeletal myoblasts for cardiac repair: Act II? J Am Coll Cardiol 2008;52(23):1881-1883.

9. Carr CA, Stuckey DJ, Tatton L, et al. Bone marrow-derived stromal cells home to and remain in the infarcted rat heart but fail to improve function: an in vivo cine-MRI study. Am J Physiol Heart Circ Physiol 2008;295(2):H533-542.

10. Shyu KG, Wang BW, Hung HF, et al. Mesenchymal stem cells are superior to angiogenic growth factor genes for improving myocardial performance in the mouse model of acute myocardial infarction. J Biomed Sci 2006;13(1):47-58.

11. Nussbaum J, Minami E, Laflamme MA, et al. Transplantation of undifferentiated murine embryonic stem cells in the heart: teratoma formation and immune response. FASEB J 2007;21(7):1345-1357.

12. Laflamme MA, Chen KY, Naumova AV, et al. Cardiomyocytes derived from human embryonic stem cells in pro-survival factors enhance function of infarcted rat hearts. Nat Biotechnol 2007;25(9):1015-1024.

13. Leobon B, Garcin I, Menasche P, et al. Myoblasts transplanted into rat infarcted myocardium are functionally isolated from their host. Proc Natl Acad Sci U S A 2003;100(13):7808-7811.

14. Pittenger MF, Mackay AM, Beck SC, et al. Multilineage potential of adult human mesenchymal stem cells. Science 1999;284(5411):143-147.

15. Kawada H, Fujita J, Kinjo K, et al. Nonhematopoietic mesenchymal stem cells can be mobilized and differentiate into cardiomyocytes after myocardial infarction. Blood 2004;104(12):3581-3587.

16. Quevedo HC, Hatzistergos KE, Oskouei BN, et al. Allogeneic mesenchymal stem cells restore cardiac function in chronic ischemic cardiomyopathy via trilineage differentiating capacity. Proc Natl Acad Sci U S A 2009;106(33):14022-14027.

17. Freyman T, Polin G, Osman H, et al. A quantitative, randomized study evaluating three methods of mesenchymal stem cell delivery following myocardial infarction. Eur Heart J 2006;27(9):1114-1122.

18. Barbash IM, Chouraqui P, Baron J, et al. Systemic delivery of bone marrow-derived mesenchymal stem cells to the infarcted myocardium: feasibility, cell migration, and body distribution. Circulation 2003;108(7):863-868.

19. Wei H, Ooi TH, Tan G, et al. Cell delivery and tracking in post-myocardial infarction cardiac stem cell therapy: an introduction for clinical researchers. Heart Fail Rev 2009;15(1):1-14.

20. Amsalem Y, Mardor Y, Feinberg MS, et al. Iron-oxide labeling and outcome of transplanted mesenchymal stem cells in the infarcted myocardium. Circulation 2007;116(11 Suppl):I38-45.

21. Qiao H, Zhang H, Zheng Y, et al. Embryonic stem cell grafting in normal and infarcted myocardium: serial assessment with MR imaging and PET dual detection. Radiology 2009;250(3):821-829.

22. Kushida T, Inaba M, Hisha H, et al. Intra-bone marrow injection of allogeneic bone marrow cells: a powerful new strategy for treatment of intractable autoimmune diseases in MRL/lpr mice. Blood 2001;97(10):3292-3299.

23. Peister A, Mellad JA, Larson BL, et al. Adult stem cells from bone marrow (MSC) isolated from different strains of inbred mice vary in surface epitopes, rates of proliferation, and differentiation potential. Blood 2004;103(5):1662-1668.

24. Gimble JM, Robinson CE, Wu X, et al. Peroxisome proliferator-activated receptor-gamma activation by thiazolidinediones induces adipogenesis in bone marrow stromal cells. Mol Pharmacol 1996;50(5):1087-1094.

25. Tropel P, Noel D, Platet N, et al. Isolation and characterisation of mesenchymal stem cells from adult mouse bone marrow. Exp Cell Res 2004;295(2):395-406.

26. Yang N, Zhang W, Shi XM. Glucocorticoid-induced leucine zipper (GILZ) mediates glucocorticoid action and inhibits inflammatory cytokine-induced COX-2 expression. J Cell Biochem 2008;103(6):1760-1771.

27. Yang Y, Yanasak N, Schumacher A, et al. Temporal and noninvasive monitoring of inflammatory-cell infiltration to myocardial infarction sites using micrometer-sized iron oxide particles. Magn Reson Med 2010;63(1):33-40.

CHAPTER 5
CHALLENGES AND RECOMMENDATIONS

In this thesis, two different cell labeling strategies were used with MPIO. One is the direct injection of MPIO into the animal blood stream to label inflammatory cells *de novo*, and the other is transplantation of MPIO-laden cells into bone marrow after labeling these cells *in vitro*. The former labeling method is a non-specific labeling methodology, since all cell types that are able to take up MPIO *in vivo* would be labeled. Nonetheless it has been recognized as an effect cell labeling strategy for labeling inflammatory cells, in particular, monocytes/macrophages. Following injection, MPIO accumulate primarily in liver, spleen, bone marrow and lymph nodes, organs or tissues that are rich in macrophages. However, the pathway of labeled macrophages migrating and homing to the pathological heart is beyond the scope of this study and thus is not studied. Similarly, how labeled MSC migrate from bone marrow to the infarction site also warrants further investigation. It will be helpful to figure out the pathway of labeled cells both in a normal condition and during the progress of myocardial infarction. One of the important points is to clarify how these labeled cells exchange between the blood and monocyte-rich organs, such as bone marrow and spleen. Appendix A and B present some preliminary results about the MPIO blood kinetics and the labeled MSC differentiation in bone marrow, respectively. However, this preliminary investigation is far less than required in order to elucidate a comprehensive circulation pathway for the MPIO-labeled cells.

The inflammatory cell tracking study demonstrated an inverse linear relationship between the MPIO dose and the MR signal intensity at the infarction site. However, further study would be recommended to delineate a direct relationship between the relative number of labeled cells and the resulted signal intensity. Once a dependable curve describing the correspondence between labeled cell number and signal intensity is developed, then the number of labeled cells could be directly interpreted from the signal intensity *in vivo*. In a preliminary study, the number of MPIO-labeled cells was counted from a transverse histology slice at differential regions including the infarcted myocardium, myocardium adjacent to the infarction site and normal myocardium. Then these regions were coregistered with their correspondences in the MR image by careful observation. A linear regression was performed between the number of labeled cells and corresponding signal intensity, through which a moderate linear correlation was acquired (Figure 5.1). Certainly far more efforts are warranted in order to delineate a credible curve. Furthermore, it must be very careful in dealing with the coregistration between the *ex vivo* histology micrographs and *in vivo* MR images. One challenge is due to that the resolution of micrographs is usually much higher than that of MR images; and the other is that the dimension as well as the shape of the heart may change dramatically after *ex vivo* histological fixation.

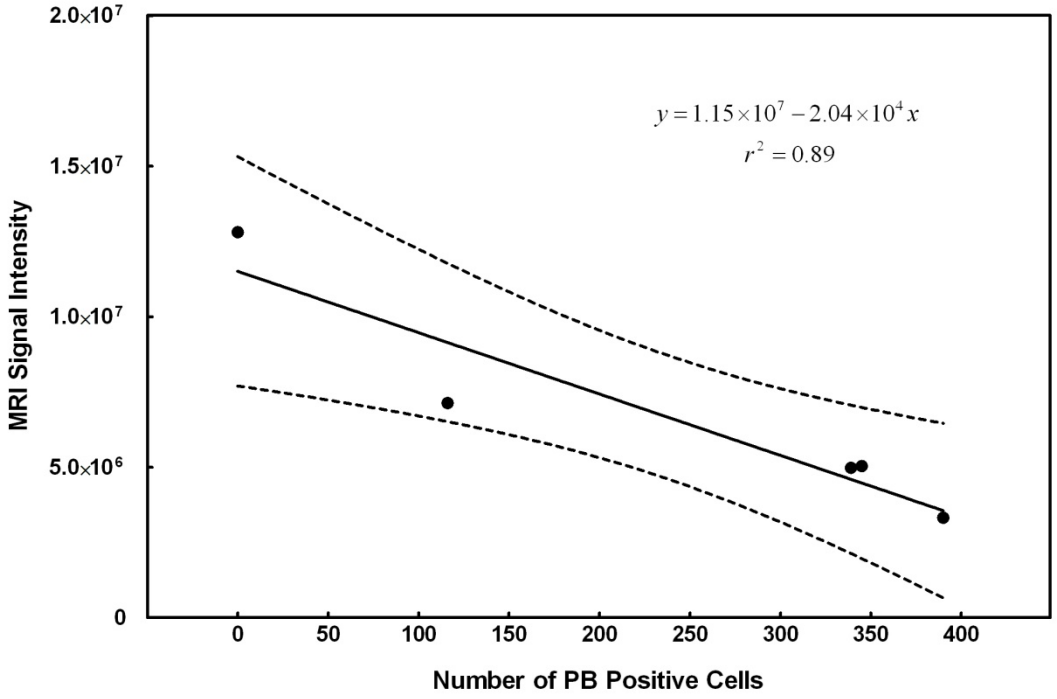

Figure 5.1 Correlation between the MR signal intensity and the number of MPIO-labeled cells. MPIO labeled cells are in dark blue in histology after Prussian blue (PB) staining. The solid line is the linear regression, and the two dotted lines show 95% confidence interval.

The MSC tracking study also warrants more investigation, particularly from a biological point view. First of all it is necessary to figure out all the cell types that the labeled MSC can differentiate into at the infarcted heart. One of the major challenges in the treatment of myocardial infarction is to find a way to regenerate the lost myocardium. Therefore it is extremely fundamental to clarify whether or not MSC are able to differentiate into cardiomyocytes and, if any, how large the cardiomyocyte population can be. A couple of labeled cells morphologically resembling cardiomyocytes were observed in the infarcted heart (Figure 5.2). However, it is recommended to design and perform robust experiments to approve this discovery.

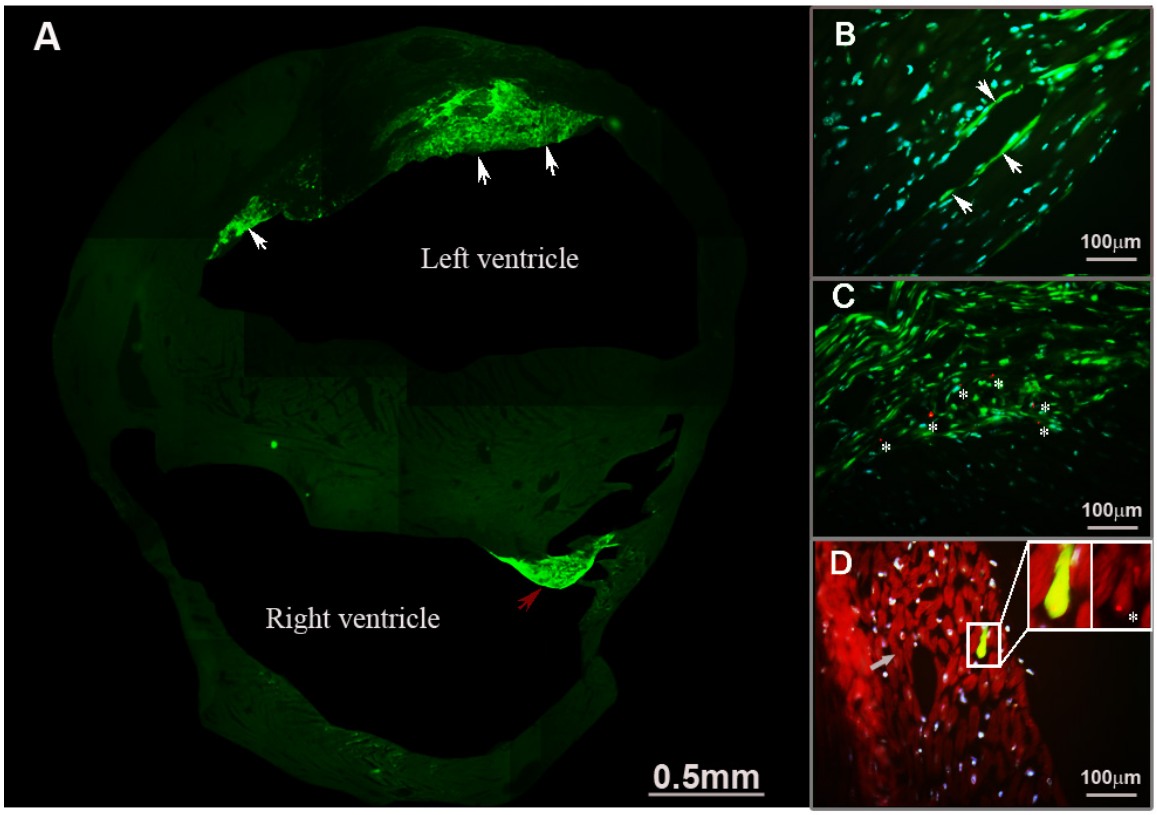

Figure 5.2 Heart histology 28 days after MSC transplantation and 14 days after infarction. Fluorescent images show the distribution and differentiation of labeled MSC from an infarcted heart at 14 days post-infarction. A. Montage cross-section of the heart using 10x magnification images from a microscope. White arrows indicate where the GFP+ cells (light green) homed to the infarction site. Interestingly, some GFP+ cells accumulated in the septal area of the heart (shown by the red arrow). This may indicate potential injury in this area. B. White arrows indicate where a large number of GFP+ cells lined the wall of a coronary blood vessel. C. GFP+ cells exhibited a fibroblast-like phenotype. MPIO particles (in red) were retained in some GFP+ cells. D. Cardiomyocyte-like cell derived from labeled MSC inserted between the resident cardiomyocytes. The higher magnification images show this cell were duo-labeled with both GFP and MPIO (red spot marked by an asterisk).

Both studies are to investigate the cell infiltration in the myocardial infarction. No matter what cell types, their infiltration should synchronize the progress of myocardial infarction. Therefore, any discovery or solution from one study would to some extent help the other. The cell labeling is completed before myocardial infarction, through either systemic injection or bone marrow transplantation. The labeled cells then home to the infarction site through the blood. These two cell implantation methods are distinct from the intra-myocardium injection, in which the cell function can be affected by the local non-optimal tissue microenvironment. In the future, it would also be interesting to systemically connect and compare the results from both studies and to find out potential correlations and interactions between the inflammatory cell and MSC infiltration.

Moreover, the techniques used in these two studies could be applied to drug test. For instance, anti-inflammatory drugs (e.g., ACE-Is and Statins) can be applied to test if any altered cellular infiltration due to drug treatment can be observed or even be quantified. Similarly, drugs that can alter stem cell mobilization can be applied to test the enhancement of cell infiltration into the infarcted heart. A preliminary study was designed to investigate the potential effect, if any, on MSC infiltration caused by granulocyte-colony stimulating factor (GCSF). The signal intensity at the myocardial infarction site in GCSF-treated group was significantly lower than that in the untreated group (Figure 5.3), indicating cell infiltration was enhanced due to GCSF injection.

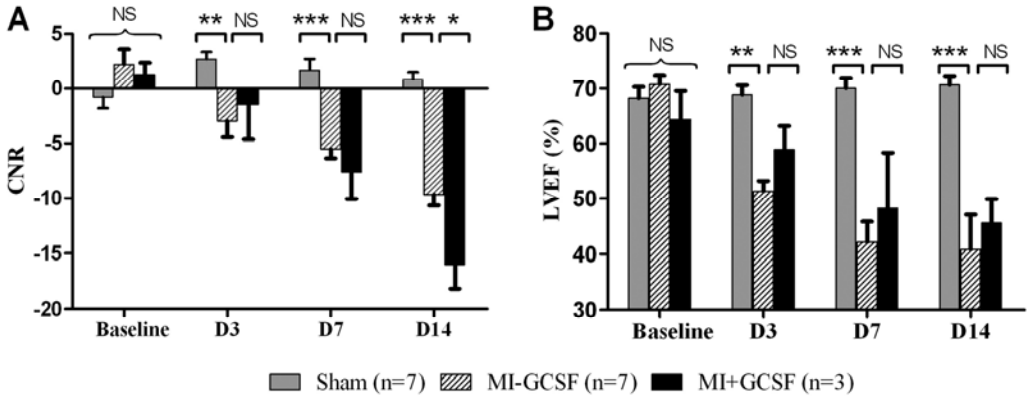

Figure 5.3 Change of CNR and LVEF due to GCSF injection. Comparison was between sham, myocardial infarction without GCSF injection (MI-GCSF) and myocardial infarction plus GCSF injection (MI+GCSF) groups. A. Gradual decrease in signal intensity was observed in both groups with myocardial infarction, indicating MPIO-labeled MSC accumulated around the infarction site over time. The MI+GCSF mice showed maximal signal attenuation at 14 days post-infarction (D14), indicating more MPIO-labeled MSC infiltration compared to the MI-GCSF group. B. Decrease in LVEF was observed in both groups with myocardial infarction. While LVEF stabilized after 7 days post-infarction, the MI+GCSF group showed higher LVEF and thus improved left ventricular function compared to the MI-GCSF group. However, the improvement was not significant. NS: not significant. D3, D7 and D14: 3, 7 and 14 days post-infarction, respectively. (*) $P < 0.05$, (**) $P < 0.01$, and (***) $P < 0.001$.

APPENDIX A
MPIO BLOOD KINETICS

Before applying iron oxide particles to cell tracking experiments, it is necessary to elucidate the blood kinetics of these particles. The blood kinetics of MPIO would determine the time interval between the MPIO injection and myocardial infarction surgery. To minimize any residual effect caused by MPIO otherwise circulating in the blood stream, it is required that myocardial infarction surgery be performed until MPIO are completely cleared out of the mouse blood. The short-term blood kinetics of MPIO has been demonstrated in chapter 2. The half life of MPIO in the mouse blood stream is determined to be less than one minute (see Figure 2.1). Figure A.1 shows the serial fluorescent images of blood samples taken at variant time points after MPIO injection. No significant fluorescence was observed from the blood sample taken at ~8 minutes post-MPIO injection.

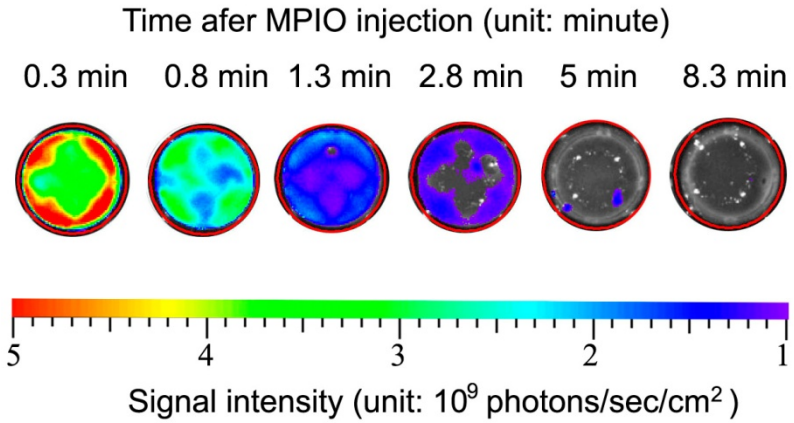

Figure A.1 Serial fluorescent images of blood samples. The blood samples (50 µl for each) were taken at variant time points after MPIO injection and put into 96-size well for fluorescent imaging.

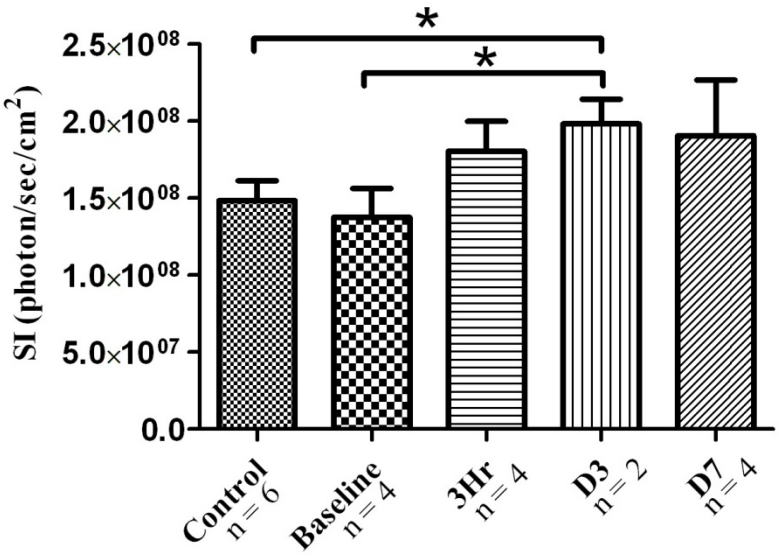

Figure A.2 Serial fluorescent intensity of blood samples taken at variant time points during the myocardial infarction process. SI: signal intensity; 3Hr, D3, and D7 stand for 3 hours, 3 days and 7 days post-infarction, respectively. The number of animal in each group is also noticed below the horizontal axis. The asterisks indicate the difference is significant under student t-test.

To further investigate the long-term MPIO blood kinetics during the process of myocardial infarction, blood samples were taken out of mouse blood stream at variant time points after the myocardial infarction surgery (3 hours, 3 days and 7 days post-infarction) and measured using fluorescent imaging. MPIO were injected 7 days before myocardial infarction. Blood samples at baseline (6 days after MPIO injection and 1 day before surgery) and control samples (blood samples taken from normal animals) were also measured as references. Figure A.2 shows the serial fluorescent intensity of blood samples for this longitudinal study. Significant difference was obtained between 3 days and either control or baseline ($P > 0.05$), indicating potential enhancement of circulating MPIO in the blood stream at 3 days post-infarction. This enhancement may be caused by the increased MPIO-laden circulating inflammatory cells in response to the myocardial

inflammation process. No significant difference was obtained between 3 days or 7 days and baseline or control. These findings may suggest that the quantity of circulating inflammatory cells maximize at 3 days post-infarction.

To conclude, the blood kinetics study finds that MPIO has a short half life of 0.73 minute in the mouse blood stream. Furthermore, the number of circulating MPIO-labeled inflammatory cells peaked at 3 days post-infarction. However, there are several drawbacks for this study. First, there are only a few time points after the infarction surgery (3 hours, 3 and 7 days). It necessitate more time points between 3 hours and 3 days in order to pinpoint the time when maximal circulating inflammatory cells can be found. Second, fluorescent imaging may not have sufficient sensitivity for quantification of MPIO-labeled cells in the blood sample. In the case of long-term study, the fluorescent intensity of blood samples taken after infarction was in the same order of those at baseline or of control. Therefore, the accuracy and reproducibility of the experiment results may be severely affected by the stability of the fluorescent imaging system. It is suggested using more accurate methods, such as flow cytometry, to quantify the absolute number of MPIO-labeled inflammatory cells in the blood sample. In these methods, either the Suncoast Yellow fluorescence or the magnetite core in MPIO can be used as a marker for identification of the MPIO-labeled cells.

APPENDIX B
MSC LABELING AND DIFFERENTIATION

It is necessary to investigate their capability of proliferation and differentiation of before and after labeled MSC are transplanted into the bone marrow. Otherwise the experiment cannot be carried on if the labeled cells lose viability. In the cell culture, the serial MSC differentiation MSC was observed at variant time points after they were labeled with MPIO. The labeled cells retained their capability of proliferation. During the 7-day observation period, a portion of cells were able to maintain the MPIO. Figure B.1 demonstrated that the daughter cells maintained MPIO for at least 7 days. During the process of cell division, MPIO are split into the descendant daughter cells. Some descendant cells will eventually lose MPIO since only a finite number of particles are included in the original MSC. Figure B.2 demonstrates the number of labeled cells at variant generations. Originally all the twenty MSC were labeled with MPIO, each MSC with variant numbers of MPIO. The labeled cells increased along with cell division, with ~120 cells labeled at 7 days. The number of total cells including both labeled and unlabeled MSC increases dramatically during the 7-day observation period. The portion of labeled cells decreased. The number of free MPIO altered with cell division, indicating some MPIO were excluded from cells and some free MPIO were incorporated into cells.

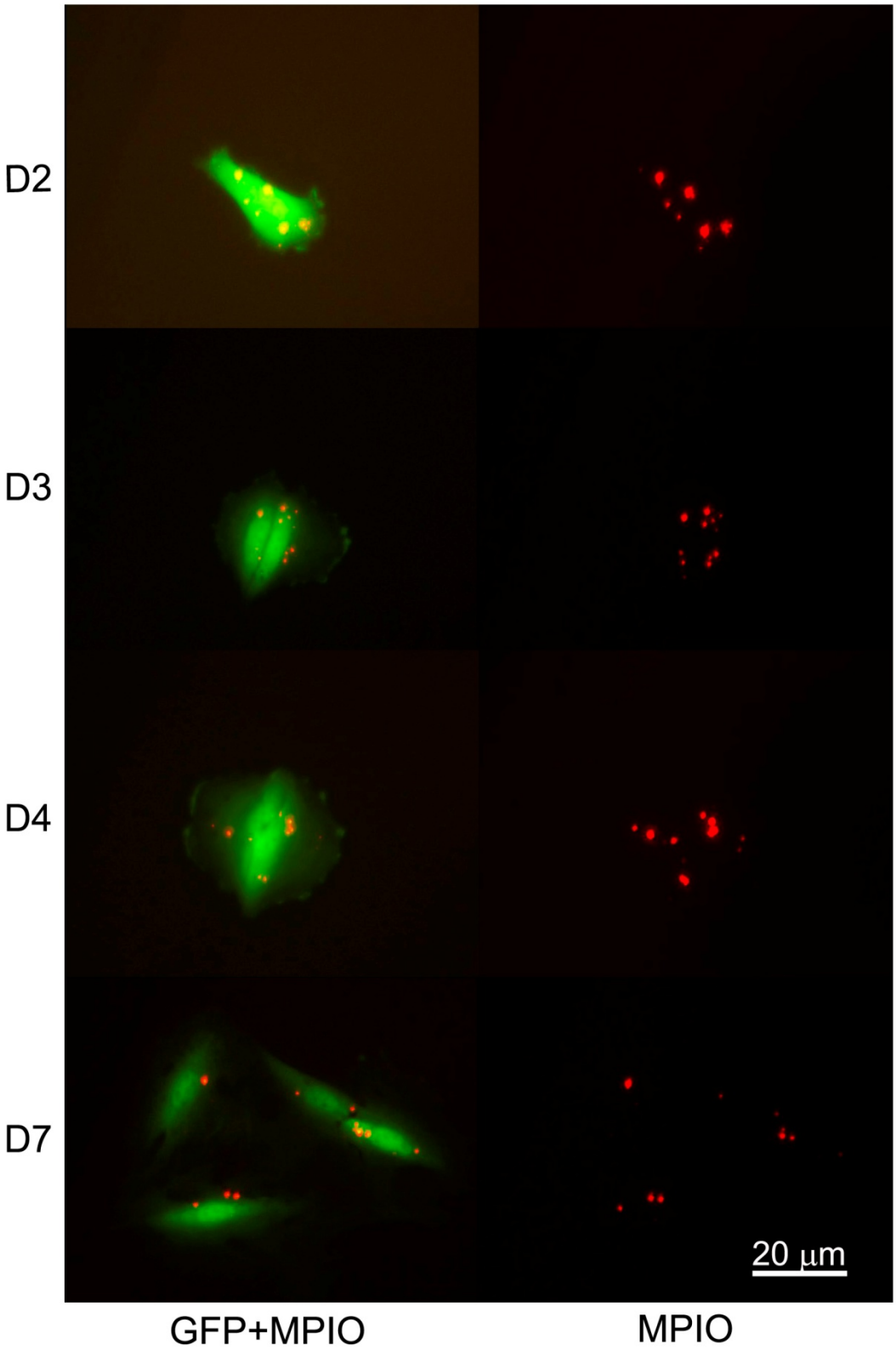

Figure B.1 Division of a single labeled MSC. Each row represents an observation date and D2, D3, D4 and D7 stand for 2, 3, 4 and 7 days after cell labeling. The green color is from the GFP and red color from MPIO.

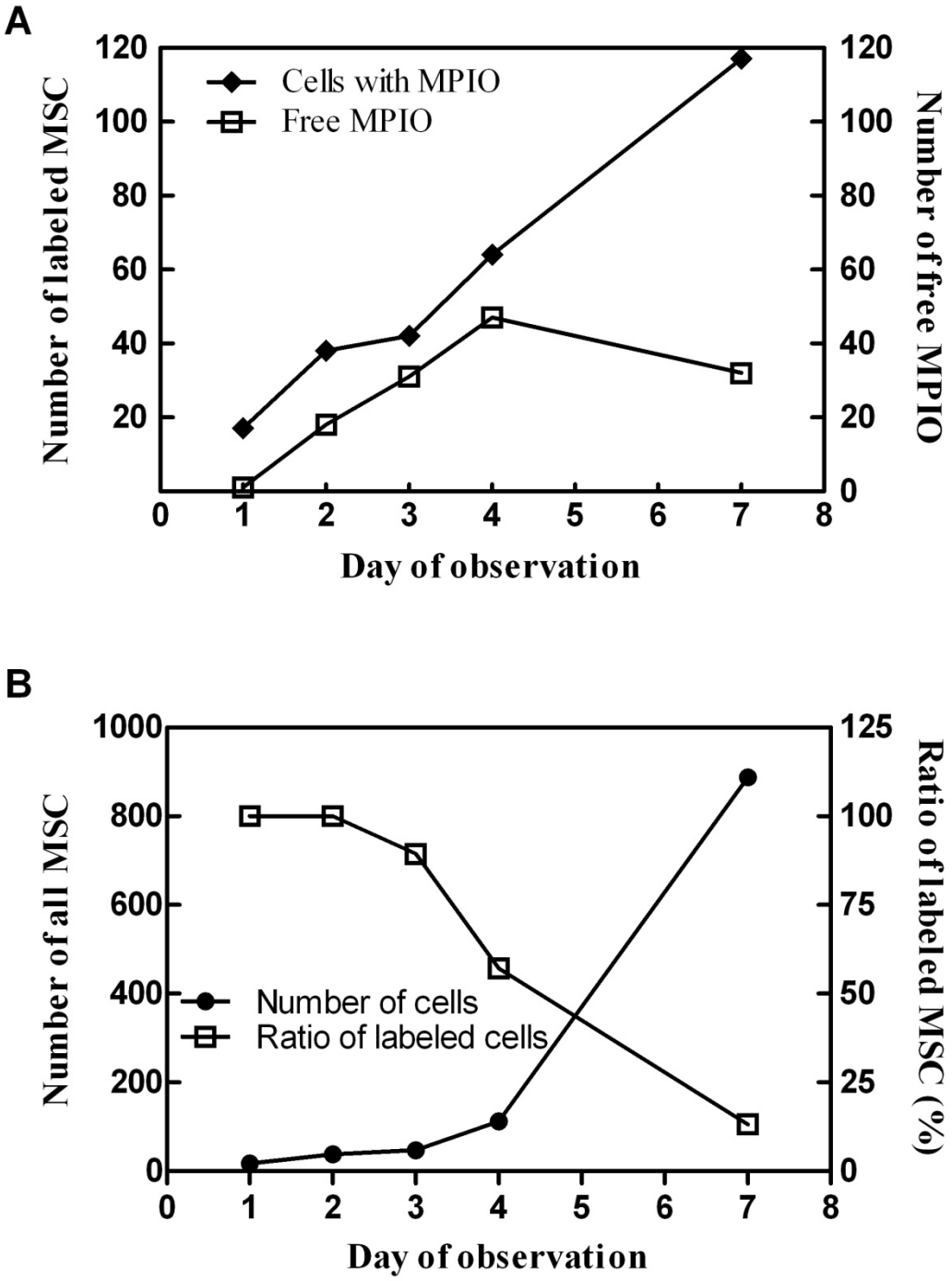

Figure B.2 Cell culture of labeled MSC during a 7-day period.

After transplantation into bone marrow, the labeled MSC retain their capability of proliferation and differentiation. In Figure B.3, the viable GFP+ cells can be observed in the marrow space after transplantation. At one hour post-transplantation, the cells scattered around in the bone marrow space. At 4 weeks post-transplantation, the number of GFP labeled cells increased dramatically, indicating the proliferation of transplanted cells. The GFP+ cells were flattened on the surface of trabeculae bone (tr), suggesting the fusion of GFP+ cells with the microenvironment. Micro-computed tomography (Micro-CT) further demonstrates the formation of new bone in the hinder leg of the animal with labeled MSC transplantation, whereas none was observed in the hinder leg of the animal with saline injection. These findings proved that the labeled MSC retain their capability of proliferation and differentiation after they are transplanted into the bone marrow, which provides the basis that the viable cells are able to home to the infarction site.

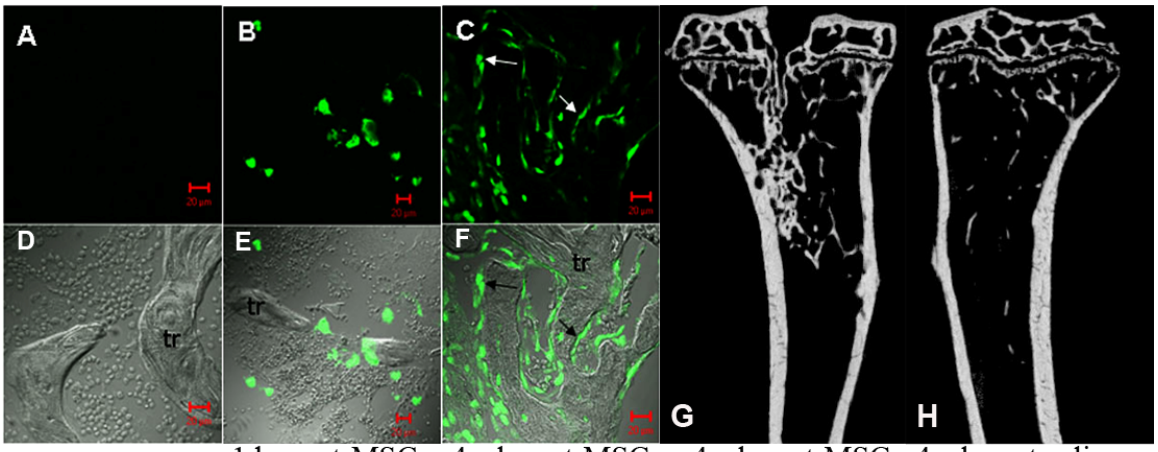

Figure B.3 MSC proliferation after transplantation into the bone marrow. A, B, C are imaging of only the GFP channel, and D, E, F imaging of the bright field. tr stands for trabecular bone. The black arrows in F point to the flattened GFP+ cells on the surface of trabecular bone. In panel A-F, the MSC were labeled only with GFP and therefore no Suncoast Yellow fluorescence was observed. The red scale bar stands for 20 μm.

APPENDIX C
A CARDIAC IMAGE ANALYSIS PROGRAM

C.1 STRUCTURE AND FUNCTION

The **CardiProc** program was developed in MATLAB environment. Currently, it can only be run within MATLAB. "CardiProc" is taken from the phrase "Cardiac Image Processing", and therefore this program is used in particular for the analysis of cardiac images. The author has used this program to analyze cardiac magnetic resonance images. The Medical College of Georgia Office of Technology Transfer has disclosed the intellectual property of this program as a provisional patent.

CardiProc program consists of seven components in its menu list, including **File**, **ROI**, **Process**, **Data**, **Segment**, **Histogram**, and **Statistic**. Each menu is for a separate function.

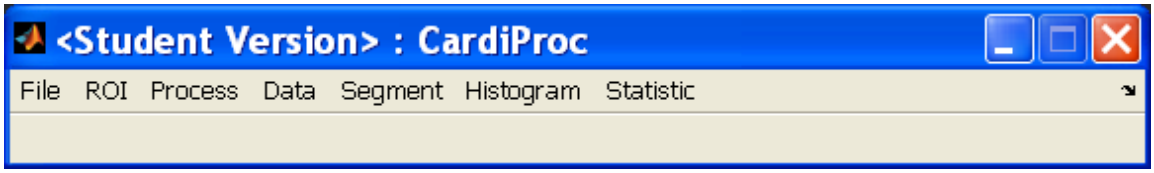

Figure C.1 The menu of CardiProc program.

The **File** menu is for opening and saving functions. There are 5 submenus: **Open**, **Save**, **Save as**, **Save all** and **Save statistics**. Users can open raw data, image sequence, mask/region of interest (ROI), as well as to localize any frame of an opened image sequence. **Save** and **Save as** function similarly to other common softwares. The

additional saving functions are accomplished by **Save all** and **Save statistics**. **Save all** can save all the data the user has analyzed into a **.Mat** file. These files can be used for the simple statistical analysis in the menu **Statistic**.

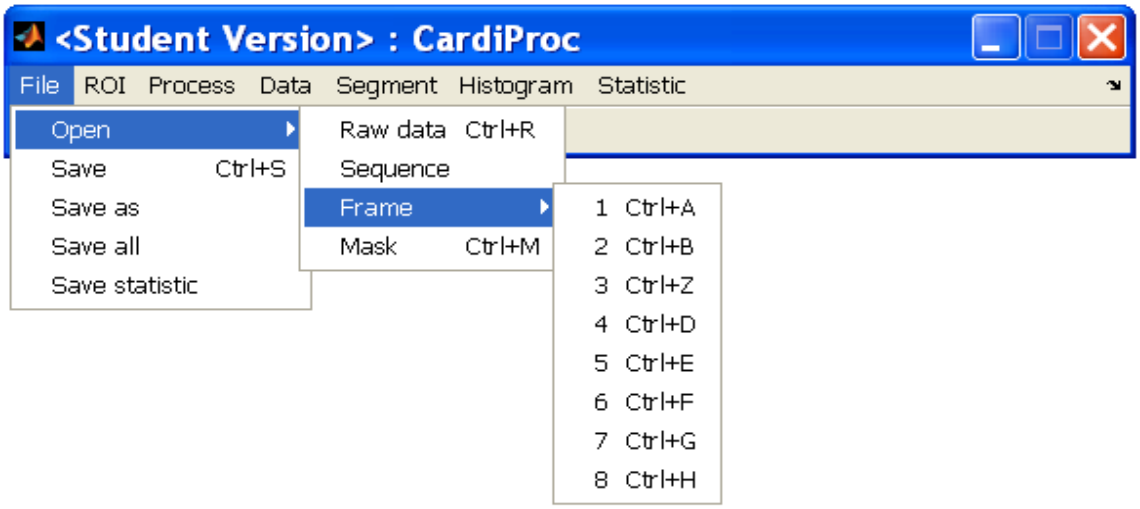

Figure C.2 File menu

The ROI menu is for ROI analysis. Users can manually draw a new ROI after clicking **New ROI**. Clicking **Load ROI** will load a saved ROI into the current image. **Save ROI** allows users to save the current ROI after they have named it. Users can use **Combine as mask** to convert the two most recently activated ROIs into a mask, which allows to process a partial image covered by the mask, for instance, the left ventricular wall.

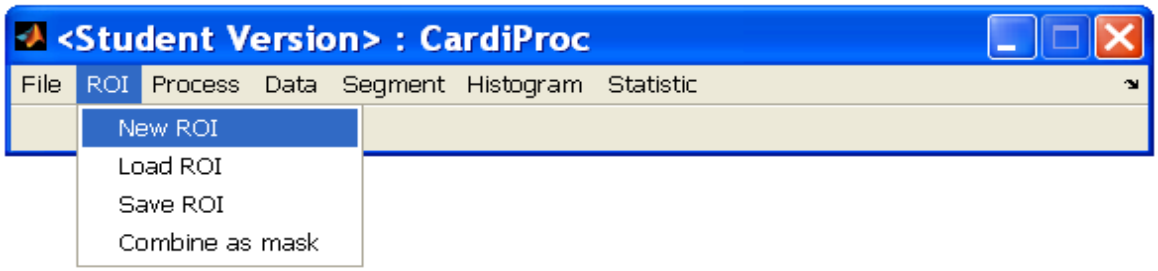

Figure C.3 ROI menu

The **Process** menu consists of two submenus. Under **MI center**, user can localize the center of the myocardial infarction area, or any point that user is interested in. Once the center is localized, the program will convert the left ventricular wall into a standard ring after the user clicks the **Standard heart** submenu. This ring with a width of 20 pixels and a circumference of 100 pixels is referred as **standard heart** in this instruction.

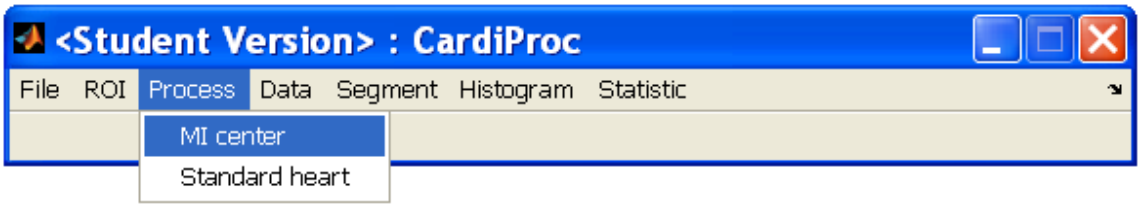

Figure C.4 Process menu.

The **Data** menu is used to calculate the thickness of the masked left ventricular wall, and to fit the 360-degree view of thickness data into a curve, which usually is a step function that can differentiate the myocardial infarction region and the adjacent regions. This is done by **Calculate thickness data** and **Fit thickness** respectively. The **Open thickness data** is used to import a saved thickness data file into the program.

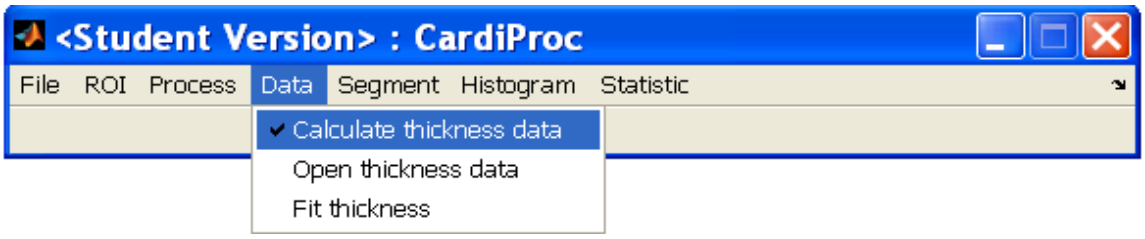

Figure C.5 Data menu.

The **Segment** menu is for segmentation of the left ventricular wall. Users can click **Uniform** submenu to segment the left ventricular wall into ten segments uniformly, or they can click **Nonuniform** to segment it into one ring composed of one myocardial infarction region, two adjacent regions and four normal myocardium regions. In this instruction the uniformly segmented and nonuniformly segmented left ventricular wall are referred as **uniform heart** and **nonuniform heart**, respectively.

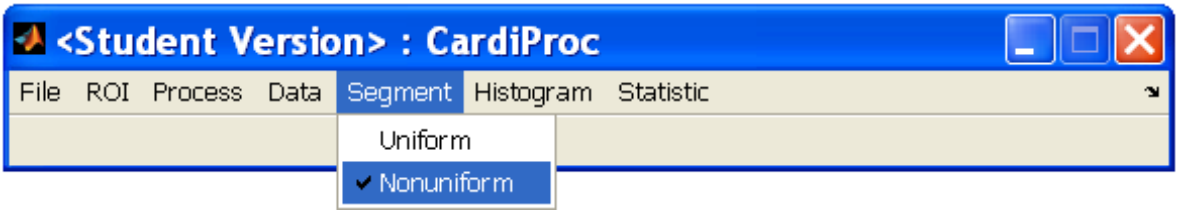

Figure C.6 Segment menu.

The user can acquire the statistical data as well as histogram for a specified ROI in **Histogram** menu. Clicking the **Histogram** submenu will pop out the **HistGUI** window. By clicking **Acquire histogram** the program will provide the statistics of the signal intensities within the current ROI. Also, a histogram will appear at the bottom, x-axis being the value of gray level (0-255) and y-axis being the number of pixels corresponding to each value. The user can save the data by clicking **Append** after they specify a file (**Browse**) and name the ROI.

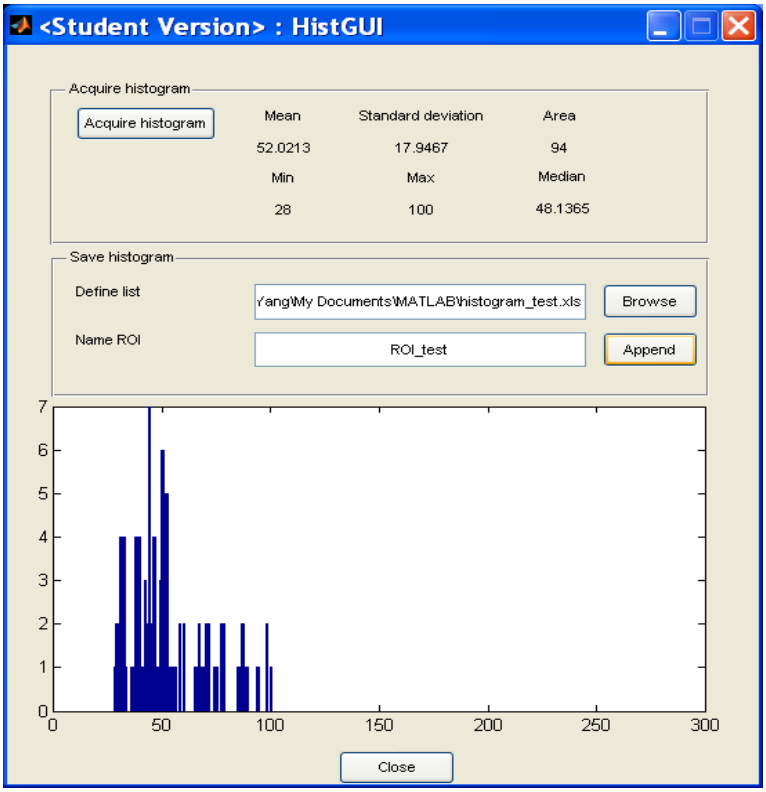

Figure C.7 Histogram analysis.

The **Statistic** menu is for batch processing of a data group. First, users have to load a file containing individual data files (.Mat format). Then they can click **Standard heart** to obtain a standard heart standing for the average of all the individual data in the file. There will be two images displayed in the window, one is the mean data, and the other is the standard deviation data. Similarly, the user can also obtain an averaged uniform heart or nonuniform heart by using **Uniform segment** or **Nonuniform segment**, respectively.

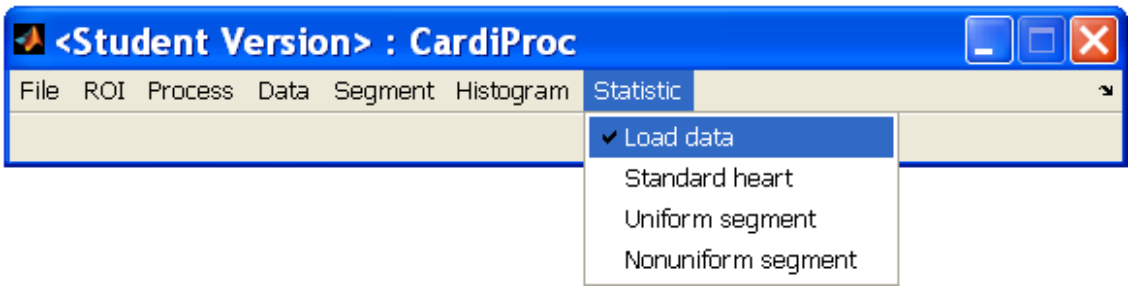

Figure C.8 Statistic menu.

C.2 EXAMPLES

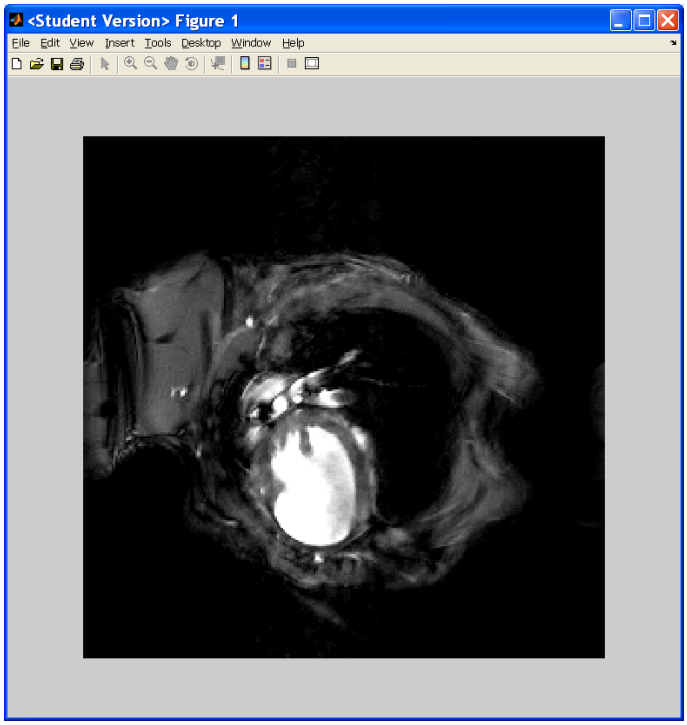

Figure C.9 An image displayed after MRI raw data is imported into the program.

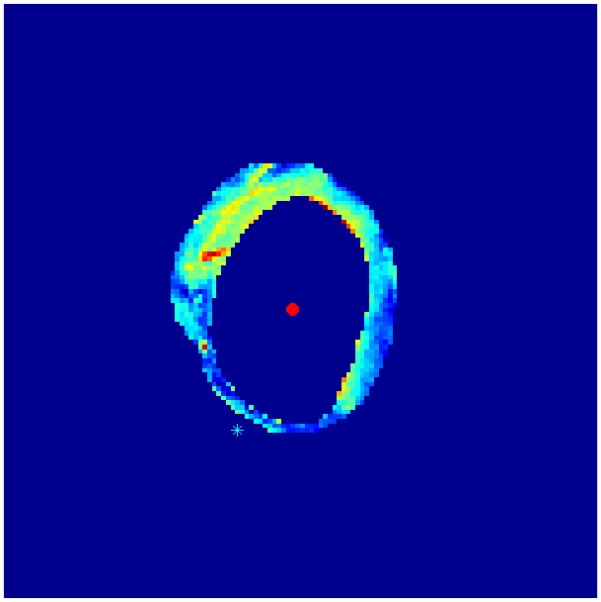

Figure C.10 The image interface for localization of the center of the infarction region. The position of the asterisk will be referred as the center of the interested region.

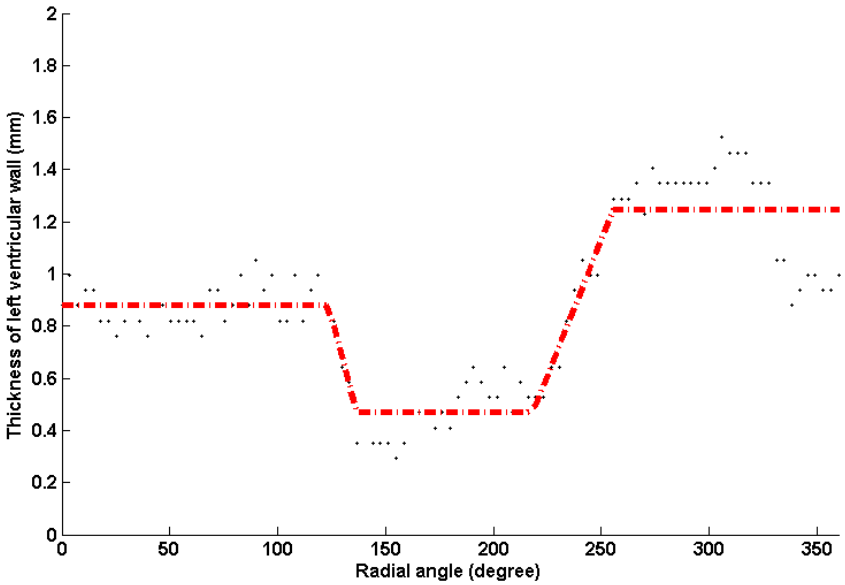

Figure C.11 Thickness data of a left ventricular wall and curve fitting (red dotted line).

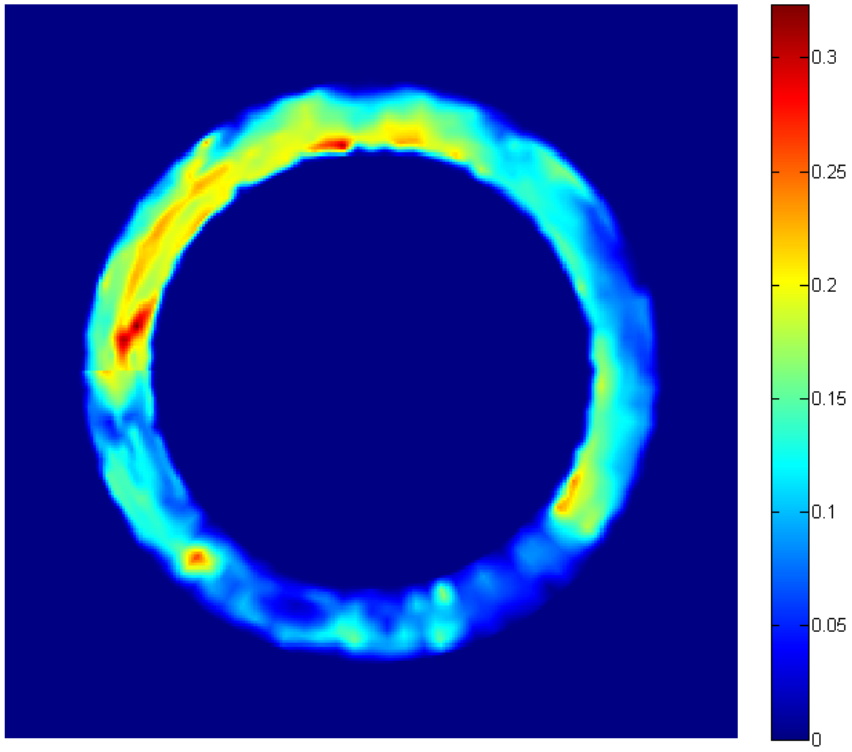

Figure C.12 A standard heart.

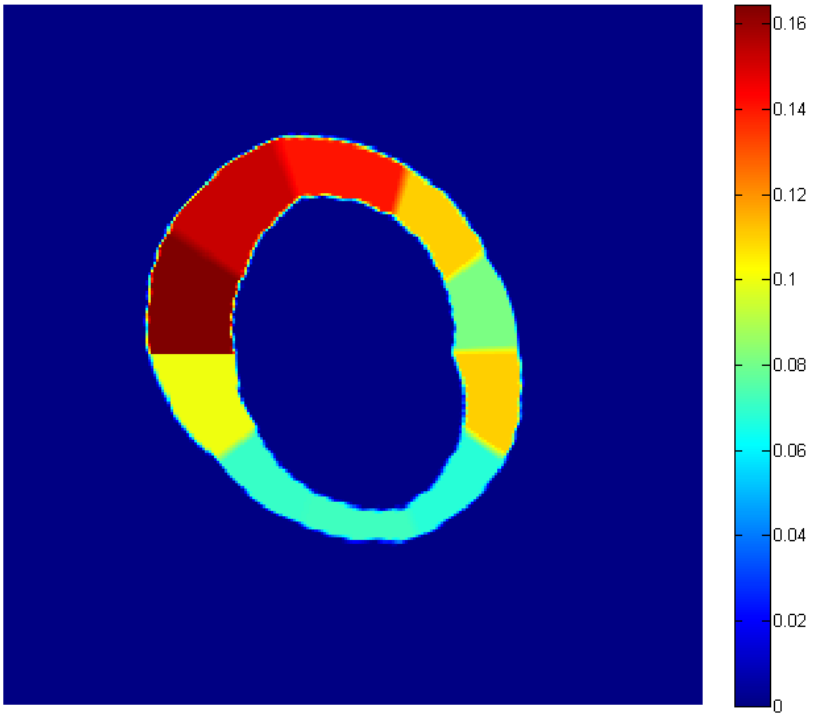

Figure C.13 A uniformly segmented left ventricular wall (uniform heart).

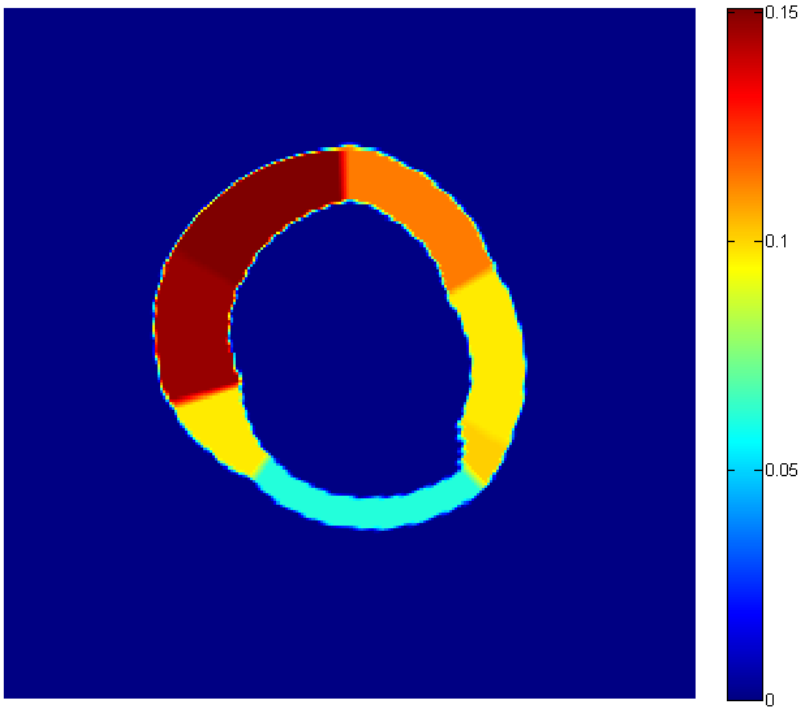

Figure C.14 A nonuniformly segmented left ventricular wall (nonuniform heart).

C.3 PROGRAM CODE

```
function varargout = CardiProc(varargin)
% CARDIPROC M-file for CardiProc.fig
%      CARDIPROC, by itself, creates a new CARDIPROC or raises the existing
%      singleton*.
%
%      H = CARDIPROC returns the handle to a new CARDIPROC or the handle to
%      the existing singleton*.
%
%      CARDIPROC('CALLBACK',hObject,eventData,handles,...) calls the local
%      function named CALLBACK in CARDIPROC.M with the given input arguments.
%
%      CARDIPROC('Property','Value',...) creates a new CARDIPROC or raises the
%      existing singleton*.  Starting from the left, property value pairs are
%      applied to the GUI before CardiProc_OpeningFunction gets called.  An
%      unrecognized property name or invalid value makes property application
%      stop.  All inputs are passed to CardiProc_OpeningFcn via varargin.
%
%      *See GUI Options on GUIDE's Tools menu.  Choose "GUI allows only one
%      instance to run (singleton)".
%
% See also: GUIDE, GUIDATA, GUIHANDLES

% Edit the above text to modify the response to help CardiProc

% Last Modified by GUIDE v2.5 04-Aug-2009 20:37:31

% Begin initialization code - DO NOT EDIT
gui_Singleton = 1;
gui_State = struct('gui_Name',       mfilename, ...
                   'gui_Singleton',  gui_Singleton, ...
                   'gui_OpeningFcn', @CardiProc_OpeningFcn, ...
                   'gui_OutputFcn',  @CardiProc_OutputFcn, ...
                   'gui_LayoutFcn',  [] , ...
                   'gui_Callback',   []);
if nargin && ischar(varargin{1})
    gui_State.gui_Callback = str2func(varargin{1});
end

if nargout
    [varargout{1:nargout}] = gui_mainfcn(gui_State, varargin{:});
else
    gui_mainfcn(gui_State, varargin{:});
end
% End initialization code - DO NOT EDIT
```

```
% --- Executes just before CardiProc is made visible.
function CardiProc_OpeningFcn(hObject, eventdata, handles, varargin)
% This function has no output args, see OutputFcn.
% hObject    handle to figure
% eventdata  reserved - to be defined in a future version of MATLAB
% handles    structure with handles and user data (see GUIDATA)
% varargin   command line arguments to CardiProc (see VARARGIN)

% Choose default command line output for CardiProc
handles.output = hObject;
handles.Flag_MICenter=0;
% Update handles structure
guidata(hObject, handles);

% UIWAIT makes CardiProc wait for user response (see UIRESUME)
% uiwait(handles.figure1);


% --- Outputs from this function are returned to the command line.
function varargout = CardiProc_OutputFcn(hObject, eventdata, handles)
% varargout  cell array for returning output args (see VARARGOUT);
% hObject    handle to figure
% eventdata  reserved - to be defined in a future version of MATLAB
% handles    structure with handles and user data (see GUIDATA)

% Get default command line output from handles structure
varargout{1} = handles.output;

%**************************************************************************
%START OF THE SUBFUNCTION BLOCKS
%**************************************************************************

%-------------------------------------------------------------------
%function to find the center of mass
%-------------------------------------------------------------------
function COM=FindCOM(Mask)
%this function find the Center of Mass (COM) of the mask image
%Mask is the mask image used for mask and also to calculate the COM; COM is
%a vector composed of the row and column number of the COM.
AntiMask=~Mask;%use the complemental image so as to find the COM of the Left
Ventrical Chamer,not the LVW.
[L,n]=bwlabel(AntiMask);%L is the label matrix, and n is the total number of connected
components.
```

```
[r,c]=find(L==2);%find the row vector (r) and column vector (c) of the connected
component labeled with 2.
rmean=round(mean(r));
cmean=round(mean(c));
COM=[rmean,cmean];

%------------------------------------------------------------------------
%function to convert image in rectangular coordinates to polar coordinates
%------------------------------------------------------------------------
function PolF = DisinPol(f,com)
%The function DisinPol draw and display the image f in polar coodinates
%The input is the image F in cartisian system, center of the mass COM, and
%the angle off the vertical line OFFANG.
%The convertion starts from 9 clock direction and rotate clockwise

th = linspace(-pi,pi,101);
r = linspace(0,50,101);
%Set the matrix=101x101
X = -50:1:50;
Y = -50:1:50;
% Specifiy the center point or the origin for the conversion
Xc=com(1);
Yc=com(2);
%crop the image to 101x101 matrix
f=f(Xc-50:Xc+50,Yc-50:Yc+50);
f=double(f);

[R, TH] = meshgrid(r,th);
%To check THETA is -pi to pi.
idx=find(TH(:)>pi);
if(~isempty(idx))
    TH(idx)=TH(idx)-2*pi;
end
idx=find(TH(:)<(-pi));
if(~isempty(idx))
   TH(idx)=TH(idx)+2*pi;
end
% Convert the pair to cartesian
[XI, YI] = pol2cart(TH, R);
% Interpolate the points to find the new data points
ZI = interp2(X, Y, f, XI, YI);
% Change the data in (Theta,R)format
PolF = ZI';
```

```
%-------------------------------------------------------------------------
%Convert into CARTISIAN coordinates from POLAR coordinates
%-------------------------------------------------------------------------
function CartIm=DisinCart(PolIm)
%This function convert the polar image to cartisian system
%The image matrix is 256x256, and original is 101x101
%x=-50:1:50;
%y=-50:1:50;
x=linspace(-50,50,256);
y=linspace(-50,50,256);
theta=linspace(-pi,pi,101);
r=linspace(0,50,101);
[X,Y]=meshgrid(x,y);
[THETA,R]=cart2pol(X,Y);
%Order: theta first, r second
%Interpolate pixel(x,y), x = column and y = row
CartIm=interp2(theta,r,PolIm,THETA,R);

%-------------------------------------------------------------------------
%Thickness data fitting function
%-------------------------------------------------------------------------
function output=FitFun2(param,input)

Aparam = param(1);
Bparam = param(2);
Cparam = param(3);
aparam = param(4);
bparam = param(5);
cparam = param(6);
dparam = param(7);
 r = input;
azslope1 = - (Aparam.*1 - Cparam.*1)/ (bparam.*1 - aparam.*1); %first adjacent zone
slope
azslope2 =(Bparam.*1 - Cparam.*1)/ (dparam.*1 - cparam.*1); %second adjacent zone
slope
azconst1 = Aparam.*1 - (azslope1 * aparam.*1);
azconst2 = Cparam.*1 - (azslope2 * cparam.*1);
azcurve1 = ((azslope1*r) + azconst1);
azcurve2 = ((azslope2*r) + azconst2);
azcurveregion1 = (Heaviside(r-(aparam.*1))-Heaviside(r-(bparam.*1)));
indexrange1 = find(azcurveregion1 == 0);
azcurve1(indexrange1) = 0;
azcurveregion2 = (Heaviside(r-(cparam.*1))-Heaviside(r-(dparam.*1)));
indexrange2 = find(azcurveregion2 == 0);
azcurve2(indexrange2) = 0;
```

```
output = (Aparam.*1)*(Heaviside(r-0)-Heaviside(r-(aparam.*1))) ...
       + azcurve1 +(Cparam.*1)*(Heaviside(r-(bparam.*1))-Heaviside(r-(cparam.*1))) ...
       + azcurve2 + (Bparam.*1)*(Heaviside(r-(dparam.*1))-Heaviside(r-101.1));

return;


%%%%%%%%%%%%%%%%%%%%%%%%%%%%%%%%%%%%%%%%%%%%%%%%%%%%%%%%%%%%%%%%%%%%%%%
%END OF SUBFUNCTION BLOCKS
%%%%%%%%%%%%%%%%%%%%%%%%%%%%%%%%%%%%%%%%%%%%%%%%%%%%%%%%%%%%%%%%%%%%%%%

% --------------------------------------------------------------------
function Open_Callback(hObject, eventdata, handles)
% hObject    handle to Open (see GCBO)
% eventdata  reserved - to be defined in a future version of MATLAB
% handles    structure with handles and user data (see GUIDATA)

% --------------------------------------------------------------------
function Save_Callback(hObject, eventdata, handles)
% hObject    handle to Save (see GCBO)
% eventdata  reserved - to be defined in a future version of MATLAB
% handles    structure with handles and user data (see GUIDATA)

%If no file is open, catch an error and return
  try
  pathname=handles.LastPathname;
  filename=hanles.LastFilename;
  catch
    return
end
File=fullfile(pathname,filename);
if isequal([filename,pathname],[0,0])
  return
elseif ~isempty(strfind(filename,'.tif'))
  try
    LastFigure=handles.LastFigure;
  catch
    errordlg('You do not have any figure to save!');
    return
  end
  imwrite(LastFigure,File,'tif');
elseif ~isempty(strfind(filename,'.mat'))
   try
     LastROI=handles.LastROI;
  catch
    errordlg('You do not have any ROI to save!');
```

```
      return
   end
    save (File, 'LastROI');
elseif ~isempty(strfind(filename,'.xls'))
    try
       ThDataT=handles.ThData;
       FitThDataT=handles.FitThData;
       FitParDataT=handles.FitParData;
    catch
      errordlg('You do not have any data to save!');
      return
    end
    xlswrite(File,ThDataT,1,'a1');%save the thickness data
    xlswrite(File,FitThDataT, 1,'b1');%save the fitted data
    xlswrite(File,FitParDataT,1,'c1');%save the fitting parameters
else
    return;
end

return


% --------------------------------------------------------------------
function SaveAs_Callback(hObject, eventdata, handles)
% hObject    handle to SaveAs (see GCBO)
% eventdata  reserved - to be defined in a future version of MATLAB
% handles    structure with handles and user data (see GUIDATA)

[filename, pathname]=uiputfile({'*.tif','Tiff image(*.tif)';...
    '*.mat','MAT-file(*.mat)';...
    '*.xls','Excel(*.xls)'},'Save as');
File=fullfile(pathname,filename);
if isequal([filename,pathname],[0,0])
   return
elseif ~isempty(strfind(filename,'.tif'))
   try
      LastFigure=handles.LastFigure;
   catch
      errordlg('You do not have any figure to save!');
      return
   end
   imwrite(LastFigure,File,'tif');
elseif ~isempty(strfind(filename,'.mat'))
    try
       LastROI=handles.LastROI;
   catch
```

```
      errordlg('You do not have any ROI to save!');
      return
    end
    save (File, 'LastROI');
elseif ~isempty(strfind(filename,'.xls'))
    try
       ThDataT=handles.ThData;
       FitThDataT=handles.FitThData;
       FitParDataT=handles.FitParData;
    catch
      errordlg('You do not have any data to save!');
      return
    end
    xlswrite(File,ThDataT,1,'a1');%save the thickness data
    xlswrite(File,FitThDataT, 1,'b1');%save the fitted data
    xlswrite(File,FitParDataT,1,'c1');%save the fitting parameters
else
    errordlg('Please specify a file format from the list!');
end

handles.LastPathname=pathname;
handles.LastFilename=filename;
guidata(hObject,handles);

return;

% --------------------------------------------------------------------
function File_Callback(hObject, eventdata, handles)
% hObject    handle to File (see GCBO)
% eventdata  reserved - to be defined in a future version of MATLAB
% handles    structure with handles and user data (see GUIDATA)

% --------------------------------------------------------------------
function RawData_Callback(hObject, eventdata, handles)
% hObject    handle to RawData (see GCBO)
% eventdata  reserved - to be defined in a future version of MATLAB
% handles    structure with handles and user data (see GUIDATA)
[filename,pathname]=uigetfile({'*.*','All files(*.*)'},...
    'Select file you want to open');
%if "Cancel" is selected then return
if isequal([filename,pathname],[0,0])
    return
%otherwise construct the full file name, and check and load the file

%if the file is '2dseq', open it
elseif strcmp(filename,'2dseq')
```

```
        %update this file as the current file
        File=fullfile(pathname,filename);
        handles.LastFile=File;
        %open the file
        fid=fopen(File,'r','l'); %open the file filename.
        fidmix=fread(fid,inf,'int16'); %read the file fid
        fidmix=reshape(fidmix,256,256); %reshape the 1-dimension array
        Image=mat2gray(fidmix);%convert matrix to inten the sity image
        Image=Image';%get the image matrix by transpose
        handles.LastFigHdl=figure;
        imshow(Image)
        hold on
        truesize([600 600]);
        handles.LastFigure=Image;
        guidata(handles.figure1,handles)
%if the file is not '2dseq',display error message
else
   errordlg('Not a valid RAW DATA file','Open file error')
end

% --------------------------------------------------------------------
function ROI_Callback(hObject, eventdata, handles)
% hObject    handle to ROI (see GCBO)
% eventdata  reserved - to be defined in a future version of MATLAB
% handles    structure with handles and user data (see GUIDATA)

% --------------------------------------------------------------------
function NewROI_Callback(hObject, eventdata, handles)
% hObject    handle to NewROI (see GCBO)
% eventdata  reserved - to be defined in a future version of MATLAB
% handles    structure with handles and user data (see GUIDATA)
%[ROI, ROI_C, ROI_R]=roipoly(handles.LastFigure);
%h=gcf;
try
   figure(handles.LastFigHdl);
catch
   errordlg('Make sure the image is open!');
   return
end
%figure(handles.LastFigHdl)
hold on
imshow(handles.LastFigure,[0.04 0.6]);
%Draw the ROI
%Use TRY CATCH statement in case interruption during ROIPOLY
try
[ROI,Row,Column]=roipoly;
```

```
%Draw ROI polygon
catch
   return
end
hold on
h=fill(Row,Column,'w');
set(h,'facecolor','none');
set(h,'edgecolor','g');
%FACECOLOR,FACEALPHA,EDGECOLOR,EDGEALPHA could be modified to
change the
%color and transparency of the surface.

%temporally save binary image ROI as the current ROI.
handles.LastROI=ROI;
guidata(hObject,handles);
return

% --------------------------------------------------------------------
function LoadROI_Callback(hObject, eventdata, handles)
% hObject    handle to LoadROI (see GCBO)
% eventdata  reserved - to be defined in a future version of MATLAB
% handles    structure with handles and user data (see GUIDATA)

%To load the ROI data
[filename, pathname]=uigetfile({'*.mat','MAT-file(*.mat)';...
   '*.*','All files(*.*)'},'Load ROI');
if isequal([filename,pathname],[0,0])
   return
else
   File=fullfile(pathname,filename);
   load(File, 'LastROI');
end
handles.LastROI=LastROI;
handles.LastPathname=pathname;
handles.LastFilename=filename;
guidata(hObject,handles);

% --------------------------------------------------------------------
function SaveROI_Callback(hObject, eventdata, handles)
% hObject    handle to SaveROI (see GCBO)
% eventdata  reserved - to be defined in a future version of MATLAB
% handles    structure with handles and user data (see GUIDATA)

%The ROI is saved as matrix in name of LastROI into the matfile.

ButtonName=questdlg('Which ROI do you want to save this as?',...
```

```
                'Save ROI',...
                'ROI_Inside','ROI_Outside','Others',...
                'Others');
switch ButtonName,
   case 'ROI_Inside',
      try
        ROI_Inside=handles.LastROI;
      catch
        errordlg('Please acquire ROI first!');
        return
      end
      LastROI=ROI_Inside;
      handles.ROI_Inside=ROI_Inside;
   case 'ROI_Outside',
      try
      ROI_Outside=handles.LastROI;
      catch
        errordlg('Please acquire ROI first!');
        return
      end
      LastROI=ROI_Outside;
      handles.ROI_Outside=ROI_Outside;
   case 'Others',%save roi and return
      try
        LastROI=handles.LastROI;
      catch
        errordlg('Please acquire ROI first!');
        return
      end
      [filename, pathname]=uiputfile({'*.mat','MAT-file(*.mat)';...
              '*.*','All files(*.*)'},'Save ROI as');
      if isequal([filename,pathname],[0,0])
         return
      else
         File=fullfile(pathname,filename);
         save (File, 'LastROI');
      end
      handles.LastPathname=pathname;
      handles.LastFilename=filename;
      %Need guidata update
      return;
   case '',
      return;
end

guidata(hObject,handles);
```

```
return;

% --------------------------------------------------------------------
function Combine_Callback(hObject, eventdata, handles)
% hObject    handle to Combine (see GCBO)
% eventdata  reserved - to be defined in a future version of MATLAB
% handles    structure with handles and user data (see GUIDATA)
%If handles.ROI_Inside and handles.ROI_Outside, catch a error
%Combine ROI_Outside and ROI_Inside to get the ROI_LVW
try
   ROI_Inside=handles.ROI_Inside;
   ROI_Outside=handles.ROI_Outside;
catch
   errordlg('Please acquire ROI first!');
   return
end
ROI_LVW=ROI_Outside-ROI_Inside;
handles.LastROI=ROI_LVW;
handles.LastMask=ROI_LVW;
guidata(hObject,handles);


% --------------------------------------------------------------------
function Mask_Callback(hObject, eventdata, handles)
% hObject    handle to Mask (see GCBO)
% eventdata  reserved - to be defined in a future version of MATLAB
% handles    structure with handles and user data (see GUIDATA)

[filename,pathname]=uigetfile({'*.mat','MAT-file';...
   '*.*','All files(*.*)'},'Select file you want to open');
%if "Cancel" is selected then return
if isequal([filename,pathname],[0,0])
   return
%otherwise construct the full file name, and check and load the file

%if the file is '2dseq', open it.
elseif strcmp(filename,'2dseq')
      %update this file as the current file
      File=fullfile(pathname,filename);
      handles.LastFile=File;
      %open the file
      fid=fopen(File,'r','l'); %open the file filename.
      %remember the viewport data from Bruker is int8 format.
      fidmix=fread(fid,inf,'int8');
      %reshape the 1-dimension array to a 256x256 matrix
      fidmix=reshape(fidmix,256,256);
```

```
    Mask=mat2gray(fidmix); %convert matrix to inten the sity image. Values [0,1]
    Mask=Mask'; %get the image matrix by transpose
    %Convert the Mask image to logic image.
    Mask=Mask>1e-10; %use 1e-10 instead of 0.
%if the file is Mat-file, load it.
elseif ~isempty(strfind(filename,'.mat'))
    File=fullfile(pathname,filename);
    load(File, 'LastROI');
    Mask=LastROI;
else %if the file is not '2dseq' or '.mat',display error message

   errordlg('Not a valid RAW DATA file','Open file error')
end
figure;
imshow(Mask);

handles.LastPathname=pathname;
handles.LastFilename=filename;
handles.LastMask=Mask;
guidata(hObject,handles)
return

% --------------------------------------------------------------------
function Overlay_Callback(hObject, eventdata, handles)
% hObject    handle to Overlay (see GCBO)
% eventdata  reserved - to be defined in a future version of MATLAB
% handles    structure with handles and user data (see GUIDATA)

% --------------------------------------------------------------------
function Data_Callback(hObject, eventdata, handles)
% hObject    handle to Data (see GCBO)
% eventdata  reserved - to be defined in a future version of MATLAB
% handles    structure with handles and user data (see GUIDATA)

% --------------------------------------------------------------------
function OpenThicknessData_Callback(hObject, eventdata, handles)
% hObject    handle to OpenThicknessData (see GCBO)
% eventdata  reserved - to be defined in a future version of MATLAB
% handles    structure with handles and user data (see GUIDATA)

[filename,pathname]=uigetfile({'*.xls','Excel(*.xls)';'*.*','All files(*.*)'},...
   'Select file you want to open');
%if "Cancel" is selected then return
if isequal([filename,pathname],[0,0])
   return
%otherwise construct the full file name, and check and load the file
```

```
%if the file is '2dseq', open it
elseif ~isempty(strfind(filename,'.xls'))
       %update this file as the current file
       File=fullfile(pathname,filename);
       handles.LastFile=File;
       %open the file
       Data=xlsread(File,1,'A1:A101');
       %Convert the column data to row data
       handles.LastData=Data';
       guidata(hObject,handles)
       %handles.LastMask
%if the file is not '2dseq',display error message
else
   errordlg('Not a valid file','Open file error')
end

handles.LastPathname=pathname;
handles.LastFilename=filename;
guidata(hObject,handles);

return

% --------------------------------------------------------------------
function CalculateThicknessData_Callback(hObject, eventdata, handles)
% hObject    handle to CalculateThicknessData (see GCBO)
% eventdata  reserved - to be defined in a future version of MATLAB
% handles    structure with handles and user data (see GUIDATA)

% Construct a questdlg to check if the MI center is already located
choice = questdlg('Have you localized the MI center?', ...
          'Please locate MI center before calculation', ...
          'Yes','No','Cancel','Cancel');
% Handle response
switch choice
   case 'Yes'
      if(~handles.Flag_MICenter)
         errordlg('Sorry, please chose MI center first!')
         return;
      end
      OffAng=handles.OffAng;
   case 'No'
      return;
   case 'Cancel'
      OffAng=0;
end
```

```
%Then display the Mask in Polar coordinates
Image=handles.LastFigure;
Mask=handles.LastMask;
Image=Image.*Mask;
%First to find the center of mass of the Left Ventricle
COM=FindCOM(handles.LastMask);
%Then to convert the image into polar coordinates
PolF=DisinPol(Image,COM);%initially set the offang to be 0.
%Then calculate the thickness data
ThickData=sum(PolF>1e-10);
%Circulate Shift (25~101/4~90 degree) elements to localize the MI center
%in the center of the plot
ColShift=round(OffAng*101/(2*pi));
ThickData=(circshift(ThickData',-25+ColShift))';
handles.LastData=ThickData;
%Update the handles data
guidata(hObject,handles);

% --------------------------------------------------------------------
function FitThickness_Callback(hObject, eventdata, handles)
% hObject    handle to FitThickness (see GCBO)
% eventdata  reserved - to be defined in a future version of MATLAB
% handles    structure with handles and user data (see GUIDATA)
Theta=1:1:101;
%If handles.LastData does not exist, catch a eorror
try
   ThData=handles.LastData;
catch
   errordlg('Please acquire thickness data first!');
   return
end
ThData=ThData*30/256/2;%In coordinate convertion, 50/101~1/2
%Define options for the least square curve fitting
options=optimset('MaxFunEvals',1000,'TolFun',1e-100,'TolX',1e-100,'MaxIter',1000);

   igA=1.5;
   igB=1.5;
   igC=0.5;
   iga=20;
   igb=40;
   igc=50;
   igd=80;
   InitialConditions=[igA,igB,igC,iga,igb,igc,igd];

[NewParam]=lsqcurvefit(@FitFun2,InitialConditions,Theta,ThData,[0,0,0,0,0,0,0],[Inf,In
f,Inf,Inf,Inf,Inf,Inf],options);
```

```
Aparam=NewParam(1);
Bparam=NewParam(2);
Cparam=NewParam(3);
aparam=NewParam(4);
bparam=NewParam(5);
cparam=NewParam(6);
dparam=NewParam(7);
r=Theta;
azslope1 = - (Aparam.*1 - Cparam.*1)/ (bparam.*1 - aparam.*1); %first adjacent zone
slope
azslope2 =(Bparam.*1 - Cparam.*1)/ (dparam.*1 - cparam.*1); %second adjacent zone
slope
azconst1 = Aparam.*1 - (azslope1 * aparam.*1);
azconst2 = Cparam.*1 - (azslope2 * cparam.*1);
azcurve1 = ((azslope1*r) + azconst1);
azcurve2 = ((azslope2*r) + azconst2);
azcurveregion1 = (Heaviside(r-(aparam.*1))-Heaviside(r-(bparam.*1)));
azcurve1(azcurveregion1 == 0) = 0;
azcurveregion2 = (Heaviside(r-(cparam.*1))-Heaviside(r-(dparam.*1)));
azcurve2(azcurveregion2 == 0) = 0;
FitData = (Aparam.*1)*(Heaviside(r-0)-Heaviside(r-(aparam.*1))) ...
      + azcurve1 +(Cparam.*1)*(Heaviside(r-(bparam.*1))-Heaviside(r-(cparam.*1))) ...
      + azcurve2 + (Bparam.*1)*(Heaviside(r-(dparam.*1))-Heaviside(r-101.1));


MICenter=(3.564*(cparam+bparam)/2);%360/101=3.564
RotAng=MICenter-180;
DataWrite={'Parameter','A','B','C','a','b','c','d','MI Center','Rotate Angle';...
   'Value',Aparam,Bparam,Cparam,aparam,bparam,cparam,dparam,MICenter,RotAng};

%Now to plot the fitting data
Angle=0:3.6:360;
figure
scatter(Angle,ThData,4,'k','o');
axis([0 360 0 2]);
hold on
plot(Angle,FitData,'r-.','LineWidth',4,'MarkerFaceColor',...
   'r','MarkerEdgeColor','r','MarkerSize',10);
xlabel('Radial angle (degree)');
ylabel('Thickness of left ventricular wall (mm)');
%Update guidata
handles.ThData=ThData';
handles.FitThData=FitData';
handles.FitParData=DataWrite';
handles.FitParam=[aparam,bparam,cparam,dparam,Aparam,Bparam,Cparam];
```

```
guidata(hObject,handles);
return;


%---------------------------------------------------------------------
%this function is to localize the MI center
%---------------------------------------------------------------------
function MICenter_Callback(hObject, eventdata, handles)
% hObject    handle to MICenter (see GCBO)
% eventdata  reserved - to be defined in a future version of MATLAB
% handles    structure with handles and user data (see GUIDATA)
try
  Mask=handles.LastMask;
  Image=handles.LastFigure;
catch
  errordlg('Please acquire MASK first!');
  return
end
Image=Image.*Mask;
%This serves as a marker to see the relative geometry during coordinates conversion.
%Image(170:180,93:200)=0;

%Find the center fo mass(COM)
%Can improve by define handles.COM as guidata
com=FindCOM(Mask);

%The window will allow us to pick the center of the MI, approximately.
dim=[256 256];
%Define a flag to determine the termination of loop

%Display the image initially
figure
imshow(Image,[min(Image(:)) max(Image(:))]);
hold on
plot(com(2), com(1), 'Marker','o','MarkerFaceColor',...
    'r','MarkerEdgeColor','r','MarkerSize',10);
truesize([600 600]);
colormap('default');

flg=0;%Flag to determine when to terminate the loop.
flg1=0;%Flag to dtermine if the user has performed left-click to locate
      %the MI center. Display a error message if Not.
ventr=zeros(1,2);
while(flg==0)
   %seems the com is localized in coordernates 256x256, although the
   %matrix for image used is 101x101.
```

```
    COLORMAP('default');
    F=gcf;
    g=get(F);
    imgpos=get(g.CurrentAxes,'Position');
    set(F,'name',...
       'Left click on the center of the MI,right click to accept or left click to clear.');
    % Choose the center of MI ...
    waitforbuttonpress;
    SelnType = get(gcf,'SelectionType');
    if(strcmp(SelnType,'normal'))
       get(F,'Units');
       set(F,'Units','Pixels');
       pos=get(F,'Position');
       loc=get(F,'CurrentPoint');
       ventr=round([dim(2)*(pos(4)-(loc(2)+imgpos(2)*pos(4)))/(pos(4)*imgpos(4)) ...
                dim(1)*(loc(1)-imgpos(1)*pos(3))/(pos(3)*imgpos(3))]);

       imshow(Image,[min(Image(:)) max(Image(:))]);
       truesize([600,600]);
       hold on
       plot(com(2), com(1), 'Marker','o','MarkerFaceColor',...
          'r','MarkerEdgeColor','r','MarkerSize',10);
       plot(ventr(2), ventr(1), 'Marker','*','MarkerFaceColor',...
          'c','MarkerEdgeColor','c','MarkerSize',10);
       flg1=1;
    %end
    % Now, agree or not? if YES, right click to terminate the procedure
    %waitforbuttonpress;
    %SelnType = get(gcf,'SelectionType');
    elseif(strcmp(SelnType,'alt'))&&flg1==1
       flg=1;
       msgbox('The MI center has been chosen');
    else %(strcmp(SelnType,'alt'))&&flg1==0
       msgbox('Please start "MI center submenu" again and chose the MI center');
       return;
       %Return the focus to the figure created previously
       %uicontrol(h);
       %Replot the original image
    end
end

%This block is to calculate the angle off the vertical line.
vectr=[ventr(1)-com(1) ventr(2)-com(2)];
norm=1./sqrt(sum(vectr.^2));
vectr=vectr*norm;
%Get the off angle, OffAng<0 if MI centers at left and >0 if at right
```

```
OffAng=atan2(vectr(2),vectr(1));
%Update the data in handles
handles.COM=com;
handles.OffAng=OffAng;
%Define a flag that indicate MI center has been chosen
handles.Flag_MICenter=1;
guidata(hObject,handles);

% --------------------------------------------------------------------
function Process_Callback(hObject, eventdata, handles)
% hObject    handle to Process (see GCBO)
% eventdata  reserved - to be defined in a future version of MATLAB
% handles    structure with handles and user data (see GUIDATA)

% --------------------------------------------------------------------
function StandardHeart_Callback(hObject, eventdata, handles)
% hObject    handle to StandardHeart (see GCBO)
% eventdata  reserved - to be defined in a future version of MATLAB
% handles    structure with handles and user data (see GUIDATA)

%To get the masked image (LVW)
try
  Image=handles.LastFigure;
  Mask=handles.LastMask;
catch
  errordlg('Please acquire IMAGE and MASK first!');
  return
end
Image=Image.*Mask;
%To display the masked image (LVW)in polar coordinates
try
COM=handles.COM;
OffAng=handles.OffAng;
PolImg=DisinPol(Image,COM);
catch
   errordlg('Please locate MI center first!');
   return
end
%To remove the NaN from the matrix
PolImg(isnan(PolImg))=0;
%To get the thickness data
ThData1=sum(PolImg>1e-10);
%Shift the data to re-locate the MI center
ColShift=round(OffAng*101/(2*pi));
ThData=(circshift(ThData1',ColShift))';
PolImgT=PolImg';
```

```
PolImgT=circshift(PolImgT,ColShift);
PolImg=PolImgT';
%Interpolate the LVW band in polar map to get the standard heart.
%The thickness of LVW is set to 20 pixels 20x(30/256)*(50/101)=1.16mm
Output=zeros(101,101);

for j=1:1:101
   NonZero=find(PolImg(:,j)>1e-6);
   L=length(NonZero);
   X=1:1:L;
   %Interpolate the L non-zero pixels to 20 pixels
   Y=linspace(1,L,20);
   NewEl=interp1(X,PolImg(NonZero,j),Y);
   %Change corresponding values in Output
   Output(61:80,j)=NewEl;
end

%ImOut=mat2gray(double(Output));
CartImg=DisinCart(Output);
figure
imshow(CartImg,[min(CartImg(:)) max(CartImg(:))]);
truesize([600,600]);
%Define COLORMAP and COLORBAR
hold on
colormap('jet');
colorbar;
%Save data
handles.ThData=ThData;
handles.StdHtMat=CartImg;
guidata(hObject,handles);

% --------------------------------------------------------------------
function Segment_Callback(hObject, eventdata, handles)
% hObject    handle to Segment (see GCBO)
% eventdata  reserved - to be defined in a future version of MATLAB
% handles    structure with handles and user data (see GUIDATA)

% --------------------------------------------------------------------
function Uniform_Callback(hObject, eventdata, handles)
% hObject    handle to Uniform (see GCBO)
% eventdata  reserved - to be defined in a future version of MATLAB
% handles    structure with handles and user data (see GUIDATA)
%To get the masked image (LVW)
try
  Image=handles.LastFigure;
  Mask=handles.LastMask;
```

```
catch
  errordlg('Please acquire IMAGE and MASK first!');
  return
end
Image=Image.*Mask;
%To display the masked image (LVW)in polar coordinates
try
  COM=handles.COM;
catch
   errordlg('Please locate the MI center first!');
   return
end
OffAng=handles.OffAng;
PolImg=DisinPol(Image,COM);
%To remove the NaN from the matrix
PolImg(isnan(PolImg))=0;
%To get the thickness data
ThData=sum(PolImg>1e-10);
%To get the Signal Intensity data
SIData=sum(PolImg)./ThData;
%Shift the data to re-locate the MI center at the bottom
ColShift=round(OffAng*101/(2*pi));
PolImg=(circshift(PolImg',ColShift))';
ThData=(circshift(ThData',ColShift))';
%Make MI localized at the center of the SI data
SIData=(circshift(SIData',ColShift))';

%To get the lower border every 10 colums
UpLtRow=zeros(1,101);
for j=1:10:101
   UpLtRow(j)=find(PolImg(:,j)>1e-10, 1 );
   %The row coordinates for every 10 columns
end

%To make the end of LVW connect to the start
UpLtRow(101)=UpLtRow(1);
ThData(101)=ThData(1);

%To get the mean value for each sector
Sum_Column=sum(PolImg);
MeanVal=zeros(1,10);
for i=1:1:10
MeanVal(i)=sum(Sum_Column((10*i-9):(10*i))./sum(ThData((10*i-9):(10*i)));
end

%To fit the border of the LVW band and save it in 2-D array BORDER, the 1st
```

```
%row is the upper border and the 2nd row is the lower border
Border=zeros(2,101);
for i=1:10:91
   for j=0:1:9
   Border(1,i+j)=round(UpLtRow(i)*((10-j)/10)+UpLtRow(i+10)*(j/10));
   Border(2,i+j)=round((UpLtRow(i)+ThData(i))*((10-j)/10)...
      +(UpLtRow(i+10)+ThData(i+10))*(j/10));
   end
end
Border(1,101)=UpLtRow(1,101);
Border(2,101)=UpLtRow(1,101)+ThData(1,101);

%To re-plot the Polar Image with UpLtRow,ThData,and MeanVal
NewPolImg=zeros(101,101);
for j=1:1:100
   NewPolImg(Border(1,j):Border(2,j),j)=MeanVal(ceil(j/10));
end
NewPolImg(Border(1,101):Border(2,101),101)=MeanVal(10);

%Process the polar image PolImg to get output with segmented LVW

CartImg=DisinCart(NewPolImg);
figure
imshow(CartImg,[min(CartImg(:)) max(CartImg(:))]);
truesize([600,600]);
%Define COLORMAP and COLORBAR
hold on
colormap('jet');
colorbar;

%Save data
%Circshift -25 to locate the middle of MI at the center of plot.
ThData=(circshift(ThData',-25))';
SIData=(circshift(SIData',-25))';
handles.ThData=ThData;
handles.SIData=SIData;
handles.Seg_MeanVal=MeanVal;
handles.Seg_UpLtRow=UpLtRow;
handles.Seg_HtMat=CartImg;
guidata(hObject,handles);

% --------------------------------------------------------------------
function Nonuniform_Callback(hObject, eventdata, handles)
% hObject    handle to Nonuniform (see GCBO)
% eventdata  reserved - to be defined in a future version of MATLAB
% handles    structure with handles and user data (see GUIDATA)
```

```
%Pass the fitting parameters
FitParam=handles.FitParam;%FitParam contains 4 valuses,a,b,c,d
%The LVW was segmented into 7 parts:MI, 2 adjacent zones, and 4 other parts
Marker=zeros(1,8);
Marker(1)=1;
Marker(2)=round(0.5*FitParam(1));
for i=3:1:6
   Marker(i)=round(FitParam(i-2));
end
Marker(7)=round(0.5*(101+FitParam(4)));
Marker(8)=101;

%This code to make all the elements are integers.
for i=1:1:8
   if Marker(i)<1
      Marker(i)=1;
   end
end

%Get the thickness data in unit of pixes
ThData=zeros(1,8);
ThData(1:3)=FitParam(5)*2*256/30;
ThData(4:5)=FitParam(7)*2*256/30;
ThData(6:7)=FitParam(6)*2*256/30;
ThData(8)=FitParam(5)*2*256/30;

%Get the image and corresponding figure
try
  Image=handles.LastFigure;
  Mask=handles.LastMask;
catch
  errordlg('Please acquire IMAGE and MASK first!');
  return
end
Image=Image.*Mask;
%To display the masked image (LVW)in polar coordinates
try
  COM=handles.COM;
catch
   errordlg('Please locate the MI center first!');
   return
end
OffAng=handles.OffAng;
PolImg=DisinPol(Image,COM);
%To remove the NaN from the matrix
```

```
PolImg(isnan(PolImg))=0;

%To get the thickness data used for calculating mean SI value
ThData1=sum(PolImg>1e-10);

%To get the Signal Intensity data
SIData=sum(PolImg)./ThData1;
%Shift the data to re-locate the MI center at the bottom
ColShift=round(OffAng*101/(2*pi));
%To corelate the image data with fitting data, additional shift -25 pixels
PolImg=(circshift(PolImg',ColShift-25))';
ThData1=(circshift(ThData1',ColShift-25))';
SIData=(circshift(SIData',ColShift-25))';


%To get the lower border every 10 colums
UpLtRow=zeros(1,101);
for j=1:1:8
   UpLtRow(Marker(j))=find(PolImg(:,Marker(j))>1e-10, 1 );
   %The row coordinates for every 10 columns
end

%To get the mean value for each sector
Sum_Column=sum(PolImg);
MeanVal=zeros(1,7);
for i=1:1:7
MeanVal(i)=sum(Sum_Column(Marker(i):Marker(i+1)))./sum(ThData1(Marker(i):Mark
er(i+1)));
end

%To fit the border of the LVW band and save it in 2-D array BORDER, the 1st
%row is the upper border and the 2nd row is the lower border
Border=zeros(2,101);
for i=1:1:7
   for j=Marker(i):1:Marker(i+1)
   Border(1,j)=round(UpLtRow(Marker(i))*((Marker(i+1)-j)/(Marker(i+1)-Marker(i)))...
      +UpLtRow(Marker(i+1))*(j-Marker(i))/(Marker(i+1)-Marker(i)));
   Border(2,j)=round(((UpLtRow(Marker(i))+ThData(i))*(Marker(i+1)-j)...
      +(UpLtRow(Marker(i+1))+ThData(i+1))*(j-Marker(i)))/(Marker(i+1)-Marker(i)));

   end
end

%To re-plot the Polar Image with UpLtRow,ThData,and MeanVal
NewPolImg=zeros(101,101);
for i=1:1:7
```

```
   for j=Marker(i):1:Marker(i+1)
   NewPolImg(Border(1,j):Border(2,j),j)=MeanVal(i);
   end
end

%To make sure the MI locate at the bottom, shift back
NewPolImg=(circshift(NewPolImg',25))';
%Process the polar image PolImg to get output with segmented LVW

CartImg=DisinCart(NewPolImg);
figure
imshow(CartImg,[min(CartImg(:)) max(CartImg(:))]);
truesize([600,600]);
%Define COLORMAP and COLORBAR
hold on
colormap('jet');
colorbar;

%Save data
handles.ThData=ThData1;
handles.SIData=SIData;
handles.NuSeg_MeanVal=MeanVal;
handles.NuSeg_UpLtRow=UpLtRow;
handles.NuSeg_ThData=ThData;
handles.NuSeg_Marker=Marker;
handles.NuSeg_HtMat=CartImg;
guidata(hObject,handles);

% --------------------------------------------------------------------
function Histogram_Callback(hObject, eventdata, handles)
% hObject    handle to Statistic (see GCBO)
% eventdata  reserved - to be defined in a future version of MATLAB
% handles    structure with handles and user data (see GUIDATA)
HistGUI();

return

% --------------------------------------------------------------------
function Histogram_Callback_Previous(hObject, eventdata, handles)
% hObject    handle to Statistic (see GCBO)
% eventdata  reserved - to be defined in a future version of MATLAB
% handles    structure with handles and user data (see GUIDATA)

%All the callback functions should appear as M-files.
ROI=handles.LastROI;
%figure('Name','Histogram','MenuBar','none','ToolBar','none',...
```

```
%    'papersize',[8 11]);
Panel_AcqHist = uipanel('Title','Acquire histogram','FontSize',12,...
              'Position',[0.01 0.75 0.98 0.25]);

Button_AcqHist = uicontrol('Parent',Panel_AcqHist,...
   'Callback',@Button_AcqHist_Callback1,...
   'String','Acquire histogram','Position',[5 50 100 30]);

Text_Mean = uicontrol('Parent',Panel_AcqHist,'style','text',...
   'String','Mean','HorizontalAlignment','center',...
   'Position',[110 50 100 30],'Tag','TextMean');
Text_MeanVal = uicontrol('Parent',Panel_AcqHist,'style','text',...
   'String','MeanVal','HorizontalAlignment','center',...
   'Position',[110 20 100 30],'Tag','TextMeanVal');
Text_Stdev = uicontrol('Parent',Panel_AcqHist,'style','text',...
   'String','Standard deviation','HorizontalAlignment','center',...
   'Position',[210 50 100 30]);
Text_StdevVal = uicontrol('Parent',Panel_AcqHist,'style','text',...
   'String','StdevVal','HorizontalAlignment','center',...
   'Position',[210 20 100 30]);
Text_Area = uicontrol('Parent',Panel_AcqHist,'style','text',...
   'String','Area','HorizontalAlignment','center',...
   'Position',[310 50 100 30]);
Text_AreaVal = uicontrol('Parent',Panel_AcqHist,'style','text',...
   'String','AreaVal','HorizontalAlignment','center',...
   'Position',[310 20 100 30]);

Panel_SaveHist =uipanel('Title','Save histogram','FontSize',12,...
              'Position',[0.01 0.59 0.98 0.2]);
Text_DefineList = uicontrol('Parent',Panel_SaveHist,'style','text',...
   'String','Define list','HorizontalAlignment','center',...
   'Position',[5 25 100 30]);
Edit_DefineList = uicontrol('Parent',Panel_SaveHist,'style','edit',...
   'String','input pathway here','HorizontalAlignment','center',...
   'Position',[110 35 300 25]);
Button_Browse = uicontrol('Parent',Panel_SaveHist,...
   'Callback','Button_Browse_Callback',...
   'String','Browse','Position',[415 35 100 25]);

Text_NameHist = uicontrol('Parent',Panel_SaveHist,'style','text',...
   'String','Name histogram','HorizontalAlignment','center',...
   'Position',[5 1 100 30]);
Edit_NameHist = uicontrol('Parent',Panel_SaveHist,'style','edit',...
   'String','input name here','HorizontalAlignment','center',...
   'Position',[110 5 300 25]);
Button_Append = uicontrol('Parent',Panel_SaveHist,...
```

```
   'String','Append','Position',[415 5 100 25]);

Axes_Hist=axes('Position',[0.05 0.05 0.94 0.52],'XLim',[0 256],...
   'XTick',0:20:260);

guidata(hObject,handles);

function Button_AcqHist_Callback1(hObject, eventdata, handles)

%ROI=handles.LastROI;
%Image=handles.LastFigure;
%Compute the histogram of the pixels in the ROI
%Histogram=imhist(Image(ROI));
%Obtain the number of pixels in the ROI
%npix=sum(ROI(:))
%Calculate the listed parameters
set(handles.TextMeanVal,'string',num2str(10));
return

% --------------------------------------------------------------
function Statistic_Callback(hObject, eventdata, handles)
% hObject    handle to Statistic (see GCBO)
% eventdata  reserved - to be defined in a future version of MATLAB
% handles    structure with handles and user data (see GUIDATA)

% --------------------------------------------------------------------
function StdHeart_Callback(hObject, eventdata, handles)
% hObject    handle to StdHeart (see GCBO)
% eventdata  reserved - to be defined in a future version of MATLAB
% handles    structure with handles and user data (see GUIDATA)
StdHtMatAll=handles.StdHtMatAll;
StdHtMean=mean(StdHtMatAll,3);
StdHtStdev=std(StdHtMatAll,1,3);
figure
subplot(1,2,1),imshow(StdHtMean,[min(StdHtMean(:)) max(StdHtMean(:))]),...
hold on, colormap('jet'),colorbar,hold off;
subplot(1,2,2),imshow(StdHtStdev,[min(StdHtStdev(:))...
   max(StdHtStdev(:))]),hold on, colormap('jet'),colorbar,hold off;
truesize([200 200]);

handles.StdHtMean=StdHtMean;
handles.StdHtStdev=StdHtStdev;
guidata(hObject,handles);

return
```

```
% --------------------------------------------------------------------
function UnifmSegmt_Callback(hObject, eventdata, handles)
% hObject    handle to UnifmSegmt (see GCBO)
% eventdata  reserved - to be defined in a future version of MATLAB
% handles    structure with handles and user data (see GUIDATA)

ThDataAll=handles.ThDataAll;
Seg_UpLtRowAll=handles.Seg_UpLtRowAll;
Seg_MeanValAll=handles.Seg_MeanValAll;

%Get the mean data
ThDataMean=mean(ThDataAll,2);
ThDataMean=circshift(ThDataMean,25);%Shift in accord with the image plot
UpLtRowMean=mean(Seg_UpLtRowAll,2);
MeanValMean=mean(Seg_MeanValAll,2);
MeanValStdev=std(Seg_MeanValAll,1,2);

%Produce the new average segmentation image
Border=zeros(2,101);
for i=1:10:91
   for j=0:1:9
   Border(1,i+j)=round(UpLtRowMean(i)*((10-j)/10)+UpLtRowMean(i+10)*(j/10));
   Border(2,i+j)=round((UpLtRowMean(i)+ThDataMean(i))*((10-j)/10)...
      +(UpLtRowMean(i+10)+ThDataMean(i+10))*(j/10));
   end
end
Border(1,101)=UpLtRowMean(101);
Border(2,101)=UpLtRowMean(101)+ThDataMean(101);

%To re-plot the Polar Image with UpLtRow,ThData,and MeanVal
NewPolImgMean=zeros(101,101);
NewPolImgStdev=zeros(101,101);
for j=1:1:100
   NewPolImgMean(Border(1,j):Border(2,j),j)=MeanValMean(ceil(j/10));
   NewPolImgStdev(Border(1,j):Border(2,j),j)=MeanValStdev(ceil(j/10));
end
NewPolImgMean(Border(1,101):Border(2,101),101)=MeanValMean(10);
NewPolImgStdev(Border(1,101):Border(2,101),101)=MeanValStdev(10);

%Process the polar image PolImg to get output with segmented LVW

SegHtMean=DisinCart(NewPolImgMean);
SegHtStdev=DisinCart(NewPolImgStdev);
figure
subplot(1,2,1),imshow(SegHtMean,[min(SegHtMean(:)) max(SegHtMean(:))]),...
  hold on, colormap('jet'),colorbar,hold off;
```

```
subplot(1,2,2),imshow(SegHtStdev,[min(SegHtStdev(:)) max(SegHtStdev(:))]),...
   hold on, colormap('jet'),colorbar,hold off;
truesize([200,200]);

handles.SegHtMean=SegHtMean;
handles.SegHtStdev=SegHtStdev;
guidata(hObject,handles);

return

% --------------------------------------------------------------------
function NonunifmSegmt_Callback(hObject, eventdata, handles)
% hObject    handle to NonunifmSegmt (see GCBO)
% eventdata  reserved - to be defined in a future version of MATLAB
% handles    structure with handles and user data (see GUIDATA)

ThDataAll=handles.NuSeg_ThDataAll;
UpLtRowAll=handles.NuSeg_UpLtRowAll;
MeanValAll=handles.NuSeg_MeanValAll;
MarkerAll=handles.NuSeg_MarkerAll;

%Get the mean data
ThDataMean=mean(ThDataAll,2);
UpLtRowMean=mean(UpLtRowAll,2);
MarkerMean=mean(MarkerAll,2);
MeanValMean=mean(MeanValAll,2);
MeanValStdev=std(MeanValAll,1,2);

%To fit the border of the LVW band and save it in 2-D array BORDER, the 1st
%row is the upper border and the 2nd row is the lower border
Border=zeros(2,101);
for i=1:1:7
   for j=MarkerMean(i):1:MarkerMean(i+1)
   Border(1,j)=round((UpLtRowMean(MarkerMean(i))*(MarkerMean(i+1)-j)...
      +UpLtRowMean(MarkerMean(i+1))*(j-MarkerMean(i)))/...
      (MarkerMean(i+1)-MarkerMean(i)));

Border(2,j)=round(((UpLtRowMean(MarkerMean(i))+ThDataMean(i))*(MarkerMean(i+
1)-j)...
      +(UpLtRowMean(MarkerMean(i+1))+ThDataMean(i+1))*(j-MarkerMean(i)))/...
      (MarkerMean(i+1)-MarkerMean(i)));

   end
end

%To re-plot the Polar Image with UpLtRow,ThData,and MeanVal
```

```
NewPolImgMean=zeros(101,101);
NewPolImgStdev=zeros(101,101);
for i=1:1:7
   for j=MarkerMean(i):1:MarkerMean(i+1)
   NewPolImgMean(Border(1,j):Border(2,j),j)=MeanValMean(i);
   NewPolImgStdev(Border(1,j):Border(2,j),j)=MeanValStdev(i);
   end
end

%To make sure the MI locate at the bottom, shift back
NewPolImgMean=(circshift(NewPolImgMean',25))';
NewPolImgStdev=(circshift(NewPolImgStdev',25))';

NuSegHtMean=DisinCart(NewPolImgMean);
NuSegHtStdev=DisinCart(NewPolImgStdev);
figure
subplot(1,2,1),imshow(NuSegHtMean,[min(NuSegHtMean(:))
max(NuSegHtMean(:))]),...
  hold on, colormap('jet'),colorbar,hold off;
subplot(1,2,2),imshow(NuSegHtStdev,[min(NuSegHtStdev(:))
max(NuSegHtStdev(:))]),...
  hold on, colormap('jet'),colorbar,hold off;
truesize([200,200]);
handles.NuSegHtMean=NuSegHtMean;
handles.NuSegHtStdev=NuSegHtStdev;
guidata(hObject,handles);

return

% --------------------------------------------------------------------
function DefineList_Callback(hObject, eventdata, handles)
% hObject    handle to Histogram (see GCBO)
% eventdata  reserved - to be defined in a future version of MATLAB
% handles    structure with handles and user data (see GUIDATA)
[filename, pathname]=uiputfile({'*.xls','Excel(*.xls)'},...
   'Define an Excel file');
if isequal([filename,pathname],[0,0])
   return
else
   File=fullfile(pathname,filename);
   handles.ListFile=File;
end
guidata(hObject,handles);
return
```

```
% --------------------------------------------------------------------
function GetHistgrm_Callback(hObject, eventdata, handles)
% hObject    handle to GetHistgrm (see GCBO)
% eventdata  reserved - to be defined in a future version of MATLAB
% handles    structure with handles and user data (see GUIDATA)

%Get the data from guidata
ROI=handles.LastROI;
%Compute the histogram of the pixels in the ROI
Histogram=imhist(f(ROI));
%Obtain the number of pixels in the ROI
npix=sum(ROI(:));

% --------------------------------------------------------------------
function SaveHistgrm_Callback(hObject, eventdata, handles)
% hObject    handle to SaveHistgrm (see GCBO)
% eventdata  reserved - to be defined in a future version of MATLAB
% handles    structure with handles and user data (see GUIDATA)

% --------------------------------------------------------------------
function Sequence_Callback(hObject, eventdata, handles)
% hObject    handle to Sequence (see GCBO)
% eventdata  reserved - to be defined in a future version of MATLAB
% handles    structure with handles and user data (see GUIDATA)
%***********Reserved for additional SUB-GUI OpenSeqGUI*******************
%OpenSeqGUI();
%************************************************************************

[filename,pathname]=uigetfile({'*.*','All files(*.*)'},...
   'Select raw sequence data you want to open');
%if "Cancel" is selected then return
if isequal([filename,pathname],[0,0])
   return
%otherwise construct the full file name, and check and load the file

%if the file is '2dseq', open it
elseif strcmp(filename,'2dseq')
     File=fullfile(pathname,filename);
     fid=fopen(File,'r','l'); %open the felile filename.
     fidmix=fread(fid,inf,'int16'); %read the file fid, one step by a int16, until the end (inf).
     %Check the length to get the frames
     NumFrame=length(fidmix)/(128*128);%Make sure the Matrix
     ImStack=reshape(fidmix,128,128,NumFrame); %reshape the 1-dimmension array to
a 256x256 matrix

     ImMontg=zeros(128,128,1,NumFrame);
```

```
    h=figure;
    hold on
    set(h,'Name','Image sequence');
    %hold off
    for i=1:NumFrame
        ImMontg(:,:,1,i)=(mat2gray(ImStack(:,:,i)))';
        %M(i)=im2frame(gray2ind(Image),colormap);
        imshow(ImMontg(:,:,1,i),'initialmagnification','fit');
        pause(1);
    end
    montage(ImMontg,'DisplayRange',[0.05 0.5]);

else

   errordlg('Not a valid RAW DATA file','Open file error')
end
%uicontrol('style','slider');
%set the initial values for uicontrols
handles.ImMontg=ImMontg;
guidata(hObject,handles)

return


% --------------------------------------------------------------------
function Frame1_Callback(hObject, eventdata, handles)
% hObject    handle to Frame1 (see GCBO)
% eventdata  reserved - to be defined in a future version of MATLAB
% handles    structure with handles and user data (see GUIDATA)
LastFigHdl=figure;
ImMontg=handles.ImMontg;
LastFigure=ImMontg(:,:,1,1);
imshow(LastFigure,[0.04 0.6],'InitialMagnification','fit');
handles.LastFigHdl=LastFigHdl;
handles.LastFigure=LastFigure;
guidata(hObject,handles)

function Frame2_Callback(hObject, eventdata, handles)
% hObject    handle to Frame2 (see GCBO)
% eventdata  reserved - to be defined in a future version of MATLAB
% handles    structure with handles and user data (see GUIDATA)
LastFigHdl=figure;
ImMontg=handles.ImMontg;
LastFigure=ImMontg(:,:,1,2);
imshow(LastFigure,[0.04 0.6],'InitialMagnification','fit');
handles.LastFigHdl=LastFigHdl;
```

```
handles.LastFigure=LastFigure;
guidata(hObject,handles)

% --------------------------------------------------------------------
function Frame_Callback(hObject, eventdata, handles)
% hObject    handle to Frame (see GCBO)
% eventdata  reserved - to be defined in a future version of MATLAB
% handles    structure with handles and user data (see GUIDATA)

% --------------------------------------------------------------------
function Frame3_Callback(hObject, eventdata, handles)
% hObject    handle to Frame3 (see GCBO)
% eventdata  reserved - to be defined in a future version of MATLAB
% handles    structure with handles and user data (see GUIDATA)
LastFigHdl=figure;
ImMontg=handles.ImMontg;
LastFigure=ImMontg(:,:,1,3);
imshow(LastFigure,[0.04 0.6],'InitialMagnification','fit');
handles.LastFigHdl=LastFigHdl;
handles.LastFigure=LastFigure;
guidata(hObject,handles)
% --------------------------------------------------------------------
function Frame4_Callback(hObject, eventdata, handles)
% hObject    handle to Frame4 (see GCBO)
% eventdata  reserved - to be defined in a future version of MATLAB
% handles    structure with handles and user data (see GUIDATA)
LastFigHdl=figure;
ImMontg=handles.ImMontg;
LastFigure=ImMontg(:,:,1,4);
imshow(LastFigure,[0.04 0.6],'InitialMagnification','fit');
handles.LastFigHdl=LastFigHdl;
handles.LastFigure=LastFigure;
guidata(hObject,handles)

% --------------------------------------------------------------------
function Frame5_Callback(hObject, eventdata, handles)
% hObject    handle to Frame5 (see GCBO)
% eventdata  reserved - to be defined in a future version of MATLAB
% handles    structure with handles and user data (see GUIDATA)
LastFigHdl=figure;
ImMontg=handles.ImMontg;
LastFigure=ImMontg(:,:,1,5);
imshow(LastFigure,[0.04 0.6],'InitialMagnification','fit');
handles.LastFigHdl=LastFigHdl;
handles.LastFigure=LastFigure;
guidata(hObject,handles)
```

```
% --------------------------------------------------------------------
function Frame6_Callback(hObject, eventdata, handles)
% hObject    handle to Frame6 (see GCBO)
% eventdata  reserved - to be defined in a future version of MATLAB
% handles    structure with handles and user data (see GUIDATA)
LastFigHdl=figure;
ImMontg=handles.ImMontg;
LastFigure=ImMontg(:,:,1,6);
imshow(LastFigure,[0.04 0.6],'InitialMagnification','fit');
handles.LastFigHdl=LastFigHdl;
handles.LastFigure=LastFigure;
guidata(hObject,handles)

% --------------------------------------------------------------------
function Frame7_Callback(hObject, eventdata, handles)
% hObject    handle to Frame7 (see GCBO)
% eventdata  reserved - to be defined in a future version of MATLAB
% handles    structure with handles and user data (see GUIDATA)
LastFigHdl=figure;
ImMontg=handles.ImMontg;
LastFigure=ImMontg(:,:,1,7);
imshow(LastFigure,[0.04 0.6],'InitialMagnification','fit');
handles.LastFigHdl=LastFigHdl;
handles.LastFigure=LastFigure;
guidata(hObject,handles)

% --------------------------------------------------------------------
function Frame8_Callback(hObject, eventdata, handles)
% hObject    handle to Frame8 (see GCBO)
% eventdata  reserved - to be defined in a future version of MATLAB
% handles    structure with handles and user data (see GUIDATA)
LastFigHdl=figure;
ImMontg=handles.ImMontg;
LastFigure=ImMontg(:,:,1,8);
imshow(LastFigure,[0.04 0.6],'InitialMagnification','fit');
handles.LastFigHdl=LastFigHdl;
handles.LastFigure=LastFigure;
guidata(hObject,handles)

% --------------------------------------------------------------------
function SaveAll_Callback(hObject, eventdata, handles)
% hObject    handle to SaveAll (see GCBO)
% eventdata  reserved - to be defined in a future version of MATLAB
% handles    structure with handles and user data (see GUIDATA)

%save and write all the data to files
```

```
[filename, pathname]=uiputfile({'*.mat','MAT-file(*.mat)'},'Save as');
File=fullfile(pathname,filename);
if isequal([filename,pathname],[0,0])
  return
elseif ~isempty(strfind(filename,'.mat'))
   try
      ThData=handles.ThData;
      SIData=handles.SIData;
      SegMeanVal=handles.Seg_MeanVal;
      SegUpLtRow=handles.Seg_UpLtRow;
      SegHtMat=handles.Seg_HtMat;
      NuSegMeanVal=handles.NuSeg_MeanVal;
      NuSegUpLtRow=handles.NuSeg_UpLtRow;
      NuSegThData=handles.NuSeg_ThData;
      NuSegHtMat=handles.NuSeg_HtMat;
      NuSegMarker=handles.NuSeg_Marker;
      StdHtMat=handles.StdHtMat;

  catch
     errordlg('Make sure you have enough data to save!');
     return
  end
   save (File, 'ThData','SIData','SegUpLtRow','SegMeanVal',...
       'SegHtMat','NuSegMeanVal','NuSegUpLtRow','NuSegHtMat',...
       'NuSegThData','NuSegMarker','StdHtMat');

else
   errordlg('Please specify a file format from the list!');
end

return;

% --------------------------------------------------------------------
function LoadData_Callback(hObject, eventdata, handles)
% hObject    handle to LoadData (see GCBO)
% eventdata  reserved - to be defined in a future version of MATLAB
% handles    structure with handles and user data (see GUIDATA)

InputDir=uigetdir('C:\Documents and Settings\Yidong Yang\My Documents\Matlab
Data',...
   'Select directory containing data files');
FileList = dir(fullfile(InputDir,'/*.mat'));
%FileList = dir(InputDir);
L=length(FileList);
ThDataAll=zeros(101,L);
SIDataAll=zeros(101,L);
```

```
Seg_UpLtRowAll=zeros(101,L);
Seg_MeanValAll=zeros(10,L);
Seg_HtMatAll=zeros(256,256,L);
NuSeg_UpLtRowAll=zeros(101,L);
NuSeg_MeanValAll=zeros(7,L);
NuSeg_HtMatAll=zeros(256,256,L);
NuSeg_ThDataAll=zeros(8,L);
NuSeg_MarkerAll=zeros(8,L);
StdHtMatAll=zeros(256,256,L);
%Fitting data for each cardiac area (Healthy,Adj,MI,Adj,Healthy)
FitData=zeros(10,L);
%Define a string array containing file names
FileName=cell(10,1);

for n=1:length(FileList)
   %get the filename of the first file within the input directory
   FileName{n,1}=FileList(n).name;
   s=load(fullfile(InputDir,FileName{n,1}));
   ThDataAll(:,n)=s.ThData;
   SIDataAll(:,n)=s.SIData;
   Seg_UpLtRowAll(:,n)=s.SegUpLtRow;
   Seg_MeanValAll(:,n)=s.SegMeanVal;
   Seg_HtMatAll(:,:,n)=s.SegHtMat;
   NuSeg_UpLtRowAll(:,n)=s.NuSegUpLtRow;
   NuSeg_MeanValAll(:,n)=s.NuSegMeanVal;
   NuSeg_HtMatAll(:,:,n)=s.NuSegHtMat;
   NuSeg_ThDataAll(:,n)=s.NuSegThData;
   NuSeg_MarkerAll(:,n)=s.NuSegMarker;
   StdHtMatAll(:,:,n)=s.StdHtMat;
end

%Caculate the fitting data such as thickness and length for each part
FitData(1,:)=NuSeg_MarkerAll(3,:)-NuSeg_MarkerAll(1,:);
FitData(2,:)=NuSeg_MarkerAll(4,:)-NuSeg_MarkerAll(3,:);
FitData(3,:)=NuSeg_MarkerAll(5,:)-NuSeg_MarkerAll(4,:);
FitData(4,:)=NuSeg_MarkerAll(6,:)-NuSeg_MarkerAll(5,:);
FitData(5,:)=NuSeg_MarkerAll(8,:)-NuSeg_MarkerAll(6,:);
FitData(6,:)=NuSeg_ThDataAll(3,:);
FitData(7,:)=0.5*(NuSeg_ThDataAll(3,:)+NuSeg_ThDataAll(4,:));
FitData(8,:)=NuSeg_ThDataAll(4,:);
FitData(9,:)=0.5*(NuSeg_ThDataAll(5,:)+NuSeg_ThDataAll(6,:));
FitData(10,:)=NuSeg_ThDataAll(6,:);
for i=1:1:5;
   FitData(i,:)=FitData(i,:)*3.6;%convert to degree (360/100).
   FitData(5+i,:)=FitData(5+i,:)*30/512;%convert to unit mm.
end
```

```
%Here write all the necessary data to Excel
[filename, pathname]=uiputfile('*.xls','Load data to Excel');
%If 'Cancel' was selected then return
if isequal([filename,pathname],[0,0])
   return
else
   File=fullfile(pathname,filename);
   %Write the filename into each row of spreadsheet
   for i=1:1:5
      xlswrite(File,FileName',i);
   end
   %1st write the thickness data
   xlswrite(File,ThDataAll,1,'a2');
   %2nd write the SI data
   xlswrite(File,SIDataAll,2,'a2');
   %3nd write the mean values of each partition in Uniform Segmentation
   xlswrite(File,Seg_MeanValAll,3,'a2');
   %4th write the mean valuse of each partition in Non-uniform
   %segmentation
   xlswrite(File,NuSeg_MeanValAll,4,'a2');
   %5th write the data for each area (Healthy,Adj,MI,Adj,Healthy)
   xlswrite(File,FitData,5,'a2');
end
msgbox([num2str(L) ' files have been loaded.']);
handles.ThDataAll=ThDataAll;
handles.SIDataAll=SIDataAll;
handles.Seg_UpLtRowAll=Seg_UpLtRowAll;
handles.Seg_MeanValAll=Seg_MeanValAll;
handles.Seg_HtMatAll=Seg_HtMatAll;
handles.NuSeg_UpLtRowAll=NuSeg_UpLtRowAll;
handles.NuSeg_MeanValAll=NuSeg_MeanValAll;
handles.NuSeg_HtMatAll=NuSeg_HtMatAll;
handles.NuSeg_ThDataAll=NuSeg_ThDataAll;
handles.NuSeg_MarkerAll=NuSeg_MarkerAll;
handles.StdHtMatAll=StdHtMatAll;
guidata(hObject,handles);

return

% --------------------------------------------------------------------
function SaveStatistic_Callback(hObject, eventdata, handles)
% hObject    handle to SaveStatistic (see GCBO)
% eventdata  reserved - to be defined in a future version of MATLAB
% handles    structure with handles and user data (see GUIDATA)
```

```
%save and write all the data to files
[filename, pathname]=uiputfile({'*.mat','MAT-file(*.mat)'},...
    'Save all statistic data');
File=fullfile(pathname,filename);
if isequal([filename,pathname],[0,0])
   return
elseif ~isempty(strfind(filename,'.mat'))
    try
       SegHtMean=handles.SegHtMean;
       SegHtStdev=handles.SegHtStdev;
       NuSegHtMean=handles.NuSegHtMean;
       NuSegHtStdev=handles.NuSegHtStdev;
       StdHtMean=handles.StdHtMean;
       StdHtStdev=handles.StdHtStdev;

   catch
      errordlg('Make sure you have enough data to save!');
      return
   end
    save (File, 'SegHtMean','SegHtStdev','StdHtMean','StdHtStdev',...
        'NuSegHtMean','NuSegHtStdev');

else
    errordlg('Please specify a file format from the list!');
end

return;
```